

# Hydrophobicity, Solvation and Structure Formation in Liquids

Blesson Chacko

Submitted in partial fulfilment of the requirements for the award of  
Doctor of Philosophy of Loughborough University

October 2017

© Blesson Chacko 2017

### **Certificate of Originality**

This is to certify that I am responsible for the work submitted in this thesis, that the original work is my own except as specified in acknowledgments or in footnotes, and that neither the thesis nor the original work contained therein has been submitted to this or any other institution for a degree.

## Abstract

In this thesis we use density functional theory (DFT) to study the solvent mediated interactions between solvophobic, solvophilic and patchy nanostructures – namely rectangular cross section blocks. We calculate both the density profiles and local compressibility around the blocks and the results obtained for our model system provide a means to understanding the basic physics of solvent mediated interactions between nanostructures, and between objects such as proteins in water, that possess hydrophobic and hydrophilic patches. Our results give an improved understanding of the behaviour of liquids around solvophobic objects and solvophobicity (hydrophobicity) in general.

Secondly, we look into the physics incorporated in standard mean-field DFT. This is normally derived by making what appears to be a rather drastic approximation for the two body density distribution function:  $\rho^{(2)}(\mathbf{r}, \mathbf{r}') \approx \rho(\mathbf{r})\rho(\mathbf{r}')$ , where  $\rho(\mathbf{r})$  is the one-body density distribution function. We provide a rationale for why the DFT often does better than this approximation would make you expect.

Finally, we develop a lattice model to understand the nature of the pattern formation exhibited by certain systems of particles deposited on liquid-air interfaces and in particular the nature of the transitions between the different patterned structures that are observed. This is done using Monte Carlo computer simulations and DFT and links the observed microphase ordering with the micellisation process seen e.g. in surfactant systems.

## **Acknowledgements**

First of all I would like to thank my supervisor, Prof. Andrew Archer, for all his support and encouragement, as well as his wisdom in suggesting the topics in this thesis for me to study. His enthusiasm for the subject was a motivation for me throughout. Also, I would like to thank Prof. Bob Evans who was really brilliant in explaining the physics and seeing the problems in a different angle.

I would also like to acknowledge all my friends in Loughborough University, especially: Chris, Morgan, Hayder, Adam, Pierpaolo, Andrea and Mark. Also, a special thanks to Fr. Paul Nellikulam for all the prayers and blessings. I also take this opportunity to acknowledge all my other friends and well-wishers (too many to list). Also, thanks to BAST Inc Ltd and to Dr. J. Grevel for allowing me to continue with my studies whilst in full-time employment.

Last, but not least, I mention my family: my parents and my sister. They have always been my backbone throughout my PhD.

*For surely I know the plans I have for you, says the Lord,  
plans for your welfare and not for harm, to give you a future with hope.*

*Jeremiah 29:11*

*For we are what he has made us, created in Christ Jesus for good works,  
which God prepared beforehand to be our way of life.*

*Ephesians 2:8*

This thesis is partly based on the following publications:

### **Chapter 5**

B. Chacko, R. Evans, and A. J. Archer.

*Solvent fluctuations around solvophobic, solvophilic and patchy nanostructures and the accompanying solvent mediated interactions.*

J. Chem. Phys. **146**, 124703 (2017).

### **Chapter 6**

A. J. Archer, B. Chacko and R. Evans.

*The standard mean-field treatment of inter-particle attraction in classical DFT is better than one might expect.*

J. Chem. Phys. **147**, 034501 (2017).

### **Chapter 7**

B. Chacko, C. Chalmers, and A. J. Archer.

*Two-dimensional colloidal fluids exhibiting pattern formation.*

J. Chem. Phys. **143**, 244904 (2015).

# Contents

<b>1</b>	<b>Introduction</b>	<b>1</b>
<b>2</b>	<b>Statistical Mechanics</b>	<b>4</b>
2.1	Pair Potentials . . . . .	5
2.2	Canonical Ensemble . . . . .	6
2.3	Grand Canonical Ensemble . . . . .	11
2.4	Particle Densities and Pair Distribution Function . . . . .	13
2.5	Ornstein-Zernike Equation and Closure Relations . . . . .	15
2.6	Static Structure Factor . . . . .	16
<b>3</b>	<b>Density Functional Theory</b>	<b>18</b>
3.1	Intrinsic Free Energy . . . . .	18
3.2	Grand Potential Functional . . . . .	20
3.3	Fundamental Measure Theory for Hard Spheres . . . . .	21
3.4	Mean-Field Approximation for Attraction . . . . .	28
3.5	Lattice DFT . . . . .	30
<b>4</b>	<b>Bulk and Interfacial Phase Behaviour of Simple Fluids</b>	<b>37</b>
4.1	Bulk Phase Behaviour . . . . .	37
4.2	Fluids at Interfaces . . . . .	39
4.2.1	Binding Potential . . . . .	41
4.2.2	Young's Equation . . . . .	43
4.2.3	Order of Phase Transition . . . . .	45
4.2.4	Solvation Force and Kelvin's Equation . . . . .	46
<b>5</b>	<b>Solvent Fluctuations Around Nanostructures</b>	<b>49</b>
5.1	Introduction . . . . .	50
5.2	Model Solvent . . . . .	56
5.3	Liquid at Planar Walls . . . . .	58
5.3.1	Single Hard Wall with an Attractive Tail . . . . .	58
5.3.2	Single Soft Lennard-Jones Wall . . . . .	61

5.3.3	Two Planar Walls . . . . .	65
5.4	Two Rectangular Blocks . . . . .	66
5.4.1	Two Solvophobic Blocks . . . . .	67
5.4.1.1	Blocks at fixed separation $x_G$ . . . . .	67
5.4.1.2	Varying the separation between the blocks . . . . .	71
5.4.2	Two Solvophilic Blocks . . . . .	75
5.4.3	One Solvophobic and One Solvophilic Block and Patchy Blocks . . . . .	77
5.4.4	Blocks Shifted Vertically . . . . .	80
5.4.5	Blocks at an Angle . . . . .	81
5.5	Concluding Remarks . . . . .	84
<b>6</b>	<b>The Standard Mean-Field DFT is Better Than One Might Expect</b>	<b>88</b>
6.1	Introduction . . . . .	88
6.2	Integral equation approach: OZ equation and RPA . . . . .	90
6.3	The mean-field DFT and the RPA . . . . .	92
6.3.1	The non-uniform fluid . . . . .	92
6.3.2	The Percus test particle procedure . . . . .	94
6.4	Illustrative results for a 1D fluid . . . . .	96
6.5	Discussion . . . . .	101
<b>7</b>	<b>Two-Dimensional Colloidal Fluids Exhibiting Pattern Formation</b>	<b>105</b>
7.1	Introduction . . . . .	105
7.2	The Model Fluid . . . . .	108
7.3	Monte Carlo . . . . .	110
7.3.1	Heat Capacity . . . . .	111
7.3.2	Cluster Formation . . . . .	113
7.3.3	Changing Box Size . . . . .	115
7.4	Lattice DFT . . . . .	119
7.5	Continuum DFT approximation . . . . .	125
7.6	Conclusion . . . . .	129
<b>8</b>	<b>Final Remarks</b>	<b>131</b>
<b>A</b>	<b>Solvent Mediated Potential for Two Identical (Asymptotic) Planar Walls</b>	<b>134</b>
<b>B</b>	<b>Linear Stability (Spinodal) Calculation for Lattice DFT</b>	<b>136</b>
	<b>Bibliography</b>	<b>139</b>

# List of Figures

2.1	Lennard-Jones pair potential . . . . .	6
2.2	Radial distribution function $g(r)$ for a hard sphere fluid using OZ equation and PY closure . . . . .	14
3.1	Continuum model to lattice model . . . . .	30
4.1	Bulk fluid phase diagram in the density versus temperature plane . . . . .	40
4.2	A schematic sketch of binding potential . . . . .	42
4.3	Density profile showing gas-liquid coexistence calculated using DFT . . . . .	43
4.4	A schematic view of different shapes a liquid forms on a surface . . . . .	45
5.1	Normalised bulk fluid phase diagram in the density versus temperature plane . . . . .	57
5.2	The bulk liquid density and bulk compressibility as a function of $\Delta\mu = (\mu - \mu_{\text{coex}})$ . . . . .	57
5.3	Density profiles $\rho(z)$ and local compressibility $\chi(z)$ for a fluid of hard spheres against a hard planar wall . . . . .	59
5.4	Scaled density profiles $\rho(z)$ and local compressibility $\chi(z)$ for a fluid of hard spheres against an attractive planar wall . . . . .	60
5.5	Contact angle $\theta$ as a function of the wall attraction strength . . . . .	62
5.6	Scaled liquid density profile and local compressibility at a single soft planar wall . . . . .	63
5.7	Capillary evaporation line calculated via DFT with that from the Kelvin equation for two parallel soft planar walls . . . . .	64
5.8	An illustration of two rectangular cross-section solid blocks immersed in the liquid . . . . .	66
5.9	Density profile $\sigma^3\rho(x, y)$ around the pair of solvophobic blocks . . . . .	67
5.10	Local compressibility $k_B T \sigma^3 \chi(x, y)$ around the pair of solvophobic blocks . . . . .	68
5.11	Density profiles and local compressibility along paths P1 and P3 . . . . .	69
5.12	Density profiles and local compressibility along path P2 . . . . .	71
5.13	Mid point density and compressibility as a function of the distance between the blocks $x_G$ . . . . .	72
5.14	The solvent mediated potential between a pair of solvophobic blocks, as a function of distance between blocks $x_G$ . . . . .	73

5.15	The solvent mediated potential between a pair of solvophilic blocks, as a function of distance between blocks $x_G$ . . . . .	76
5.16	The solvent mediated potential between various pairs of blocks, as a function of distance between blocks $x_G$ . . . . .	78
5.17	Local density and compressibility profiles around various pairs of blocks . . . . .	79
5.18	The solvent mediated potential between various pairs of blocks, as a function of distance between blocks $y_S$ . . . . .	80
5.19	Local density and compressibility profiles around solvophobic blocks with various relative orientation . . . . .	82
5.20	The solvent mediated potential between a pair of solvophobic blocks, as a function of orientation angle $\alpha$ . . . . .	83
5.21	The solvent mediated potential between a pair of solvophobic blocks of relative orientation angle $\alpha = 45^\circ$ . . . . .	84
6.1	The total correlation function $h(x)$ and the structure factor $S(k)$ for hard-rods for various values of attraction strength $z_p$ . . . . .	97
6.2	The total correlation function $h(x)$ and the structure factor $S(k)$ for hard-rods with tail potential (6.4.3) for various values of bulk density $\rho_b$ . . . . .	98
6.3	The total correlation function $h(x)$ and the structure factor $S(k)$ for hard-rods for various values of attraction range $\sigma_p$ . . . . .	99
7.1	Double-Yukawa pair potential . . . . .	109
7.2	Monte Carlo simulation snapshots for different parameters . . . . .	110
7.3	Heat capacity against chemical potential from Monte Carlo simulations . . . . .	112
7.4	Ratio of lone particles in the system against chemical potential and density . . . . .	113
7.5	The static structure factor $S(k)$ for a range of different values of the chemical potential	116
7.6	The static structure factor $S(k)$ for a range of different wavevectors, $k$ . . . . .	117
7.7	The heat capacity versus chemical potential for two different box sizes . . . . .	117
7.8	Probability of finding a certain instantaneous density within a simulation . . . . .	118
7.9	Probability distribution for the density Fourier mode amplitude calculated at the cluster to stripe transition . . . . .	118
7.10	Series of density profiles calculated from the lattice DFT . . . . .	121
7.11	Phase diagram with respect to chemical potential . . . . .	122
7.12	A comparison of the average density as a function of $\mu$ from the MC simulations and DFT. Also, the DFT density profiles showing the discontinuous changes in the stripes as $\mu$ is varied . . . . .	124
7.13	Phase diagram with respect to density . . . . .	125
7.14	The dispersion relation for varying attraction strength . . . . .	127
7.15	Instability lines from lattice DFT and continuum DFT . . . . .	128

# Chapter 1

## Introduction

Liquids are important even though they generally only exist over a relatively small range of temperatures and pressures. Along with the solid and gas phases, the liquid forms one of the three states of matter formed by substances composed of simple molecules or atoms (of course there is plasma, but that state can be treated as a gas). We humans need water, the most common liquid on Earth, for our life, oil for fuel and lubrication, to mention a few uses. Microscopic particles suspended in a liquid is called a colloidal liquid. Examples of so called colloidal liquids include blood and paint. In some cases the colloids order to form patterns, which in a biological system the ordering of particles suspended in a liquid plays an important role in the formation and growth of the cells and tissues [1]. Some substances are hydrophobic, i.e. not attractive to water, a classical example would be wax or oil. Water is not the only solvent that exhibits such a behaviour. In fact one can generalise this notion by the term ‘solvophobic’ to refer to a substance for which one finds it is energetically unfavourable to be in contact with a particular solvent under consideration.

The detailed study of gases and solids started since the beginning of 19<sup>th</sup> and mid-20<sup>th</sup> Century, respectively, due to scientific advances in e.g. quantum mechanics and in applications of scattering techniques to study periodic lattices of atoms and molecules [2]. Even though theories of statistical mechanics (some in chapter 2) are applicable to any system, still comments like “*neither statistical mechanics nor chemical physics understands the liquid state*” [3] appear. This is because for the high density liquid state non-perturbative approaches are needed, as a perturbative approach based on a non-interacting gas fails. The non-perturbative approach leads to hierarchies of coupled equations involving correlation functions which are difficult to deal with analytically.

That one should expect theories for the liquid state to be accurate can be seen by recalling the principle that nature obeys as it equilibrates towards equilibrium is to evolve to the minimum of the free energy (this arises from the second law of thermodynamics) [4]. For a system with fixed number of particles  $N$ , volume  $V$  and temperature  $T$ , the particular free energy that is minimised at equilibrium is the Helmholtz free energy, given by the equation

$$F = U - TS \quad (1.0.1)$$

where  $U$  is the internal energy and  $S$  is the entropy. For a solid/crystal at low temperature, this is equivalent to minimising the internal energy  $U$  since the first term on the right hand side of Eq. (1.0.1) dominates. In contrast, for the gas which occurs at high temperatures, the second term dominates and so at equilibrium we minimise  $-TS$ , i.e. maximise the entropy  $S$ . The larger entropy implies that the gas is widely spread in a maximally disordered state. However, in the liquid, there is a subtle balance between  $U$  and  $TS$  in which case the theory needs to be good and accurate. This thesis is the latest contribution to this endeavour.

Liquids and gases do not have a rigid structure like a solid – they are both *fluids*. The high density fluid is called liquid and the low density fluid is called gas and these two fluid states can coexist for temperatures below the critical temperature. The van der Waals theory of the gas-liquid transition forms the basis of much of our understanding of fluid structure and phase behaviour [5].

The availability of super computers in 1960s, opened a window to enable the study of the theory of liquids into more depth. This became possible because the computer is able to solve the coupled equations of motion of a few hundred liquid particles (molecular dynamics) or to solve the approximate integral equation which gave an understanding of the structure of liquids to compare with ‘the exact solution’ from the computer simulations. The simulation (which is sometimes rather slow) is thus used for the verification of the theory, helping to develop better and more sophisticated theories. Nowadays, the theory of liquids is a well established subject and there exist many standard textbooks on the subject such as Refs. [6, 7, 8]. The book by Hansen and McDonald [9], is excellent and comprehensively describes the theory of liquids and is referred to throughout the thesis.

The use of thermodynamics and statistical mechanics is not limited to the study of liquids; it is increasingly used in the fields of condensed matter physics, chemical physics and material sci-

ence [10]. Examples include high temperature superconductors [11] and biomaterials [12]. Further, quantum mechanics problems can be solved using statistical mechanics as well [13].

This thesis proceeds as follows: In chapter 2, we present the background on statistical mechanics and introduce the concept of ensembles and how to find various thermodynamic properties. In chapter 3, we introduce density functional theory (DFT) which provides an approximation to solve many of the statistical mechanics problems. DFT approximations relevant to the system of interest are derived both for the continuum and lattice system. Chapter 4 looks into how a fluid behaves in bulk and when it is near a surface. All these chapters provide a good background to the following chapters in which the original results from our work are described.

In chapter 5, we study the behaviour of fluid around different nanostructures that are solvophobic or solvophilic. We start with a simple model of fluid in contact with a planar wall where the fluid density only varies in the  $z$ -direction. We then introduce another wall to form a slit and describe the confined fluid behaviour. With this result in mind, we develop a system consisting of two blocks that are chemically similar or different to each other. Here we look at the density profile and local compressibility of the fluid and compare the results. Further calculations to obtain the solvent mediated potentials between the surfaces are described, making use of chapter 4. In chapter 6, we elucidate some of the physical content of the approximate DFT used in chapter 5 by comparing the exact solution of one-dimensional hard rods to the results from the approximate DFT, which is derived in chapter 2 and chapter 3.

In chapter 7, we study a lattice model for 2D colloidal fluids where the colloids have attractive interactions at short separations, but repel at longer range. We use Monte Carlo simulations to study the system. In particular we look at the heat capacity and the structure factor. Moreover, the phase diagram obtained from the simulations is compared with the results from mean-field DFT. Finally, in chapter 8 we make a few concluding remarks and suggestions for potential future works.

## Chapter 2

# Statistical Mechanics

*Statistical mechanics tries to link from the microscopic (atomic-scale) description of a particular substance to its equilibrium macroscopic (thermodynamic) properties, such as compressibility, heat capacity, phase behaviour etc. Here we introduce the key concepts that form a basis for this thesis.*

Many of the key foundational contributions to statistical mechanics was made by Austrian physicist Ludwig Boltzmann in the 1870s by providing a theory relating the microscopic properties of individual particles to the macroscopic properties of materials as discussed in classical thermodynamics. Statistical mechanics forms a branch of physics for studying the thermodynamic behaviour of systems composed of a large number of particles, by applying probability theory [14]. The presentation of the ideas from statistical mechanics required in this thesis and presented in this chapter largely follows the standard presentation of the theory by Hansen and McDonald in Ref. [9].

For a system consisting of  $N$  identical, spherical particles of mass  $m$  in an isolated macroscopic system, the state of the system is characterised by  $6N$  generalised coordinates  $\mathbf{r}^N \equiv \{\mathbf{r}_1, \dots, \mathbf{r}_N\}$  and momenta  $\mathbf{p}^N \equiv \{\mathbf{p}_1, \dots, \mathbf{p}_N\}$ . The total energy of the system is then given by the Hamiltonian:

$$\mathcal{H}(\mathbf{r}^N, \mathbf{p}^N) = K_N(\mathbf{p}^N) + V_N(\mathbf{r}^N) + \Phi_N(\mathbf{r}^N) \quad (2.0.1)$$

where, the first term is the sum of the kinetic energy of the particles:

$$K_N(\mathbf{p}^N) = \sum_{i=1}^N \frac{\mathbf{p}_i^2}{2m}. \quad (2.0.2)$$

The second term is the potential energy due to the interactions between particles

$$V_N(\mathbf{r}^N) = \sum_{i < j} V(\mathbf{r}_i, \mathbf{r}_j) + \left[ \sum_{i < j < k} V_3(\mathbf{r}_i, \mathbf{r}_j, \mathbf{r}_k) + \dots \right] \quad (2.0.3)$$

which contains pairwise, triplets and there may be even higher body interactions, i.e.  $V(\mathbf{r}, \mathbf{r}')$  is the pair potential between two particles and  $V_3(\mathbf{r}, \mathbf{r}', \mathbf{r}'')$  is a three body potential. Throughout this thesis we consider the interactions between the particles to be only pairwise, i.e. we assume the terms in the square bracket can be neglected. The last term in the Hamiltonian

$$\Phi_N(\mathbf{r}^N) = \sum_{i=1}^N \phi(\mathbf{r}_i) \quad (2.0.4)$$

is the external potential contribution, where  $\phi(\mathbf{r})$  is the one body external potential [15].

## 2.1 Pair Potentials

The intermolecular forces between the particles are modelled using pair interactions. The simplest interaction one might conceive of is the hard sphere interaction

$$V_{\text{HS}}(r) = \begin{cases} \infty & \text{if } r < \sigma \\ 0 & \text{otherwise,} \end{cases} \quad (2.1.1)$$

where,  $r$  is the separation between the particles' centres and  $\sigma$  is the diameter of the particles. This potential is an example of a *hard core* particle, i.e. particles do not overlap each other and is used in the derivation of Fundamental Measure Theory DFT in chapter 3.

Throughout the thesis various pair potentials are used to describe the system we are considering. One such potential, the Lennard-Jones (LJ) potential, that provides a reasonable approximation for the effective potential between pairs of noble gas atoms, such as Argon, is given by:

$$V_{\text{LJ}}(r) = 4\varepsilon \left[ \left( \frac{\sigma}{r} \right)^{12} - \left( \frac{\sigma}{r} \right)^6 \right], \quad (2.1.2)$$

where  $\sigma$  is the diameter of the particle and  $\varepsilon$  is the attraction parameter. For this potential, when

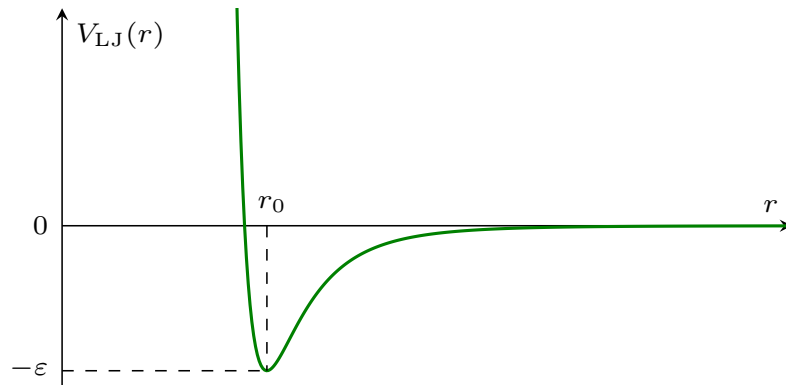


Figure 2.1: The Lennard-Jones pair interaction potential between particles.

the particle separation is smaller than a certain distance  $r_0$ , the particles are repulsive and for larger separations the particles are attractive – see Fig. 2.1. The Pauli repulsion between atomic electrons is modelled by the repulsive  $r^{-12}$  core and the induced dipole - induced dipole interaction between atoms for large separations is modelled by the attractive  $r^{-6}$  term. This attractive term is also referred to as the London dispersion potential [16]. Note that the LJ-potential is finite for all  $r > 0$ , i.e. in principle the particles can penetrate the core of another one. There are many other pair potentials one could consider, like the Square-well and Yukawa potentials; for more details see Ref. [9].

The pair potentials are not limited to the interactions between the fluid particles. The walls of any container are also made of particles and one may use a pair potential to describe the interaction with the container particles or to derive an effective one body external field exerted by the container wall. We use the LJ-potential in chapter 5 to model the interaction between the fluid and planar walls and other objects.

## 2.2 Canonical Ensemble

One can determine the average thermodynamic properties of a system by considering an ensemble which is a large collection of identical physical systems with the same macroscopic properties. Averaging over all these systems gives the ensemble average.

Consider a system where we fix the number of particles  $N$ , volume  $V$  and temperature,  $T$ . The fixed temperature can be viewed as stemming from the system being immersed in a heat bath. An

assembly of all possible microstates of the system is called a canonical ensemble. The probability density of the system being in a particular state in the canonical ensemble is

$$f(\mathbf{r}^N, \mathbf{p}^N) = \frac{1}{h^{dN} N!} \frac{e^{-\beta \mathcal{H}(\mathbf{r}^N, \mathbf{p}^N)}}{Z} \quad (2.2.1)$$

where,  $d$  is the dimensionality of the system,  $h$  is Plank's constant and  $\beta = (k_B T)^{-1}$  ( $k_B$  is the Boltzmann constant). The term  $h^{dN}$  appears in the denominator on dimensional grounds and also to be consistent with quantum statistical mechanics since we do not know exactly both the position and momentum of the particle. This is Heisenberg's uncertainty principle. A factor of  $h$  is introduced for each product  $d\mathbf{r}d\mathbf{p}$  since this can only be known to an uncertainty  $h$ . The  $1/N!$  term appears to adjust for the over counting due to the indistinguishability of the particles.  $Z$  is the partition function, which ensures  $f$  is correctly normalised [9]. The canonical partition function is defined as

$$Z = \frac{1}{h^{dN} N!} \iint e^{-\beta \mathcal{H}(\mathbf{r}^N, \mathbf{p}^N)} d\mathbf{r}^N d\mathbf{p}^N, \quad (2.2.2)$$

where  $\int d\mathbf{r}^N = \int d\mathbf{r}_1 \int d\mathbf{r}_2 \cdots \int d\mathbf{r}_N$  and similarly,  $\int d\mathbf{p}^N = \int d\mathbf{p}_1 \int d\mathbf{p}_2 \cdots \int d\mathbf{p}_N$ . The partition function is the sum over all the possible configurations of the system.

### Ensemble Average and Some Thermodynamic Functions

The average value of an arbitrary physical quantity that is a function of the phase space coordinates  $\{\mathbf{r}^N, \mathbf{p}^N\}$ , say  $B(\mathbf{r}^N, \mathbf{p}^N)$ , is defined in the canonical ensemble as

$$\langle B \rangle = \iint B(\mathbf{r}^N, \mathbf{p}^N) f(\mathbf{r}^N, \mathbf{p}^N) d\mathbf{r}^N d\mathbf{p}^N. \quad (2.2.3)$$

This is called the ensemble average of the quantity  $B$ , where  $f(\mathbf{r}^N, \mathbf{p}^N)$  is the probability density given in Eq. (2.2.1). The ensemble average of the Hamiltonian,  $\mathcal{H}$ , in Eq. (2.0.1) gives the total internal energy,  $U$ , of the system at equilibrium. Hence, in the canonical ensemble using the configurational probability in Eq. (2.2.1), we get

$$U \equiv \langle \mathcal{H} \rangle = \frac{1}{h^{3N} N! Z} \iint \mathcal{H} e^{-\beta \mathcal{H}} d\mathbf{r}^N d\mathbf{p}^N. \quad (2.2.4)$$

Hence, From Eqs. (2.2.2) and (2.2.4), we can see that [9]

$$U = \langle \mathcal{H} \rangle = -\frac{1}{Z} \frac{\partial Z}{\partial \beta} = -\frac{\partial}{\partial \beta} \ln Z. \quad (2.2.5)$$

Therefore, we obtain a macroscopic quantity,  $U$ , expressed as the derivative of  $Z$ , a sum over all microscopic states. Other derivatives of the partition function  $Z$ , can be used in a similar way to obtain expressions for many other thermodynamic quantities.

Another thermodynamic quantity is the heat capacity at constant volume, defined as

$$C_V = \left( \frac{\partial U}{\partial T} \right)_V, \quad (2.2.6)$$

which can be also be linked with statistical mechanics using the partition function  $Z$ . From Eqs. (2.2.2) and (2.2.3) one can see

$$\langle \mathcal{H}^2 \rangle = \frac{1}{Z} \frac{\partial^2 Z}{\partial \beta^2}. \quad (2.2.7)$$

Therefore, for the energy fluctuations in the system, we have the result:

$$\begin{aligned} \langle \mathcal{H}^2 \rangle - \langle \mathcal{H} \rangle^2 &= \frac{1}{Z} \frac{\partial^2 Z}{\partial \beta^2} - \left( \frac{1}{Z} \frac{\partial Z}{\partial \beta} \right)^2 \\ &= \frac{1}{Z} \frac{\partial}{\partial \beta} \left( \frac{\partial Z}{\partial \beta} \right) + \frac{\partial}{\partial \beta} \left( \frac{1}{Z} \right) \frac{\partial Z}{\partial \beta} \\ &= \frac{\partial}{\partial \beta} \left( \frac{1}{Z} \frac{\partial Z}{\partial \beta} \right) \\ &= -\frac{\partial}{\partial \beta} \langle \mathcal{H} \rangle = -\frac{\partial U}{\partial \beta}. \end{aligned} \quad (2.2.8)$$

Note also that,

$$-\frac{\partial U}{\partial \beta} = k_B T^2 \frac{\partial U}{\partial T} = k_B T^2 C_V. \quad (2.2.9)$$

Therefore, we can find the heat capacity from the energy fluctuations within the system,

$$C_V = \frac{\langle \mathcal{H}^2 \rangle - \langle \mathcal{H} \rangle^2}{k_B T^2}. \quad (2.2.10)$$

From this we see that the heat capacity is always positive, since  $\langle \mathcal{H}^2 \rangle - \langle \mathcal{H} \rangle^2 \geq 0$  and  $k_B T^2 \geq 0$ .

### The configurational integral

Later in this chapter, we see that many thermodynamic quantities can be obtained from the partition function  $Z$ . Therefore it is useful to simplify the partition function. Using Eq. (2.0.1), the partition function can be expressed as

$$Z = \frac{1}{h^{dN} N!} \int e^{-\beta K(\mathbf{p}^N)} d\mathbf{p}^N \int e^{-\beta[V(\mathbf{r}^N) + \Phi(\mathbf{r}^N)]} d\mathbf{r}^N. \quad (2.2.11)$$

This means the integrals over the momenta degrees of freedom do not depend on the integrals over the positions of the particles. Therefore, using Eq. (2.0.2), one can factorise the first integral as

$$\int \exp(-\beta K(\mathbf{p}^N)) d\mathbf{p}^N = \prod_{i=1}^N \int \exp\left(-\frac{\beta \mathbf{p}_i^2}{2m}\right) d\mathbf{p}_i. \quad (2.2.12)$$

Moreover, the components of  $\mathbf{p}_i = (p_{i,1}, p_{i,2}, \dots, p_{i,d})$  are also independent, since the components are orthogonal to each other. Therefore

$$\begin{aligned} \int \exp\left(-\frac{\beta \mathbf{p}_i^2}{2m}\right) d\mathbf{p}_i &= \int \exp\left(-\frac{\beta p_{i,1}^2}{2m}\right) dp_{i,1} \times \dots \times \int \exp\left(-\frac{\beta p_{i,d}^2}{2m}\right) dp_{i,d} \\ &= \left(\frac{2\pi m}{\beta}\right)^{d/2}, \end{aligned} \quad (2.2.13)$$

since  $\int_{-\infty}^{\infty} \exp(-\alpha^2 u^2) du = \sqrt{\pi}/\alpha$ . Thus

$$\frac{1}{h^{dN}} \int \exp(-\beta K(\mathbf{p}^N)) d\mathbf{p}^N = \frac{1}{h^{dN}} \prod_{i=1}^N \left(\frac{2\pi m}{\beta}\right)^{d/2} = \left(\frac{2\pi m}{\beta h^2}\right)^{dN/2}. \quad (2.2.14)$$

Therefore, the partition function reduces to

$$Z = Q \Lambda^{-dN}, \quad (2.2.15)$$

where  $\Lambda = \sqrt{\frac{\beta h^2}{2\pi m}}$  is the thermal de Broglie wavelength of a particle and

$$Q = \frac{1}{N!} \int \exp[-\beta(V_N + \Phi_N)] d\mathbf{r}^N \quad (2.2.16)$$

is the *configuration integral* since the remaining integration is over configuration space [15].

## Helmholtz Free Energy

The relevant thermodynamic potential for a canonical ensemble (where  $T$ ,  $V$ ,  $N$  are fixed) is the Helmholtz free energy, which is defined as [17]

$$F = U - TS, \quad (2.2.17)$$

where  $S$  is the entropy and  $U$  is the internal energy of the system. The differential form of the internal energy is given by the first law of thermodynamics (conservation of energy), which states

$$dU = TdS + \mu dN - pdV, \quad (2.2.18)$$

where  $\mu$  is the chemical potential (the energy to insert a particle into the system) and  $p$  is the pressure and it follows that

$$U = TS + \mu N - pV, \quad (2.2.19)$$

since  $S$ ,  $N$  and  $V$  are all extensive quantity (i.e. scales with the size of system). Hence, using the differential form of Eq. (2.2.17) along with (2.2.18), one can write the differential of the free energy as

$$dF = -SdT + \mu dN - pdV. \quad (2.2.20)$$

Therefore, all other thermodynamic functions can be obtained by differentiation if  $F$  is a known function of  $N$ ,  $V$  and  $T$ :

$$S = - \left( \frac{\partial F}{\partial T} \right)_{V,N}, \quad \mu = \left( \frac{\partial F}{\partial N} \right)_{T,V}, \quad p = - \left( \frac{\partial F}{\partial V} \right)_{T,N}. \quad (2.2.21)$$

For a given  $N$ ,  $V$  and  $T$ , the equilibrium state of the system corresponds to the minimum of the Helmholtz free energy. The partition function  $Z$ , which is a sum over all the microscopic states, and the macroscopic quantities of thermodynamics is related to the Helmholtz free energy [9]

$$F = -k_B T \ln Z, \quad (2.2.22)$$

which is sometimes called the *Massieu Bridge*.

## 2.3 Grand Canonical Ensemble

In the canonical ensemble discussed above, we have a fixed temperature  $T$ , volume  $V$  and total number of particles in the system  $N$ , which can be written as

$$N = \int \hat{\rho}(\mathbf{r}) \, d\mathbf{r} \quad (2.3.1)$$

where the microscopic particle density at any given instant,  $\hat{\rho}(\mathbf{r})$ , is defined as sum of Dirac- $\delta$  functions, i.e. [18]

$$\hat{\rho}(\mathbf{r}) = \sum_{i=1}^N \delta(\mathbf{r} - \mathbf{r}_i). \quad (2.3.2)$$

We now consider a system where the number of particles is not fixed, but instead the system is coupled to a “reservoir” which allows for an exchange of particles between the system and the reservoir. The average number of particles in the system is controlled by the chemical potential,  $\mu$ , which is the energy required to insert a particle into the system and is determined by the reservoir. The reservoir is essentially just another part of the system, that is much larger than the part of the system on which we are focused. This is a grand canonical ensemble (an open system).

In the grand canonical ensemble, the probability of the system being in a particular state is given by

$$f(\mathbf{r}^N, \mathbf{p}^N) = \frac{1}{h^{dN} N!} \frac{e^{-\beta(\mathcal{H} - \mu N)}}{\Xi}, \quad (2.3.3)$$

where  $\Xi$  is the grand partition function

$$\Xi = \sum_{N=0}^{\infty} \frac{1}{h^{dN} N!} \iint e^{-\beta(\mathcal{H} - \mu N)} \, d\mathbf{r}^N \, d\mathbf{p}^N \quad (2.3.4)$$

$$= \text{Tr} \, e^{-\beta(\mathcal{H} - \mu N)}. \quad (2.3.5)$$

Here,  $\text{Tr}$  denotes the classical trace, i.e. [19]

$$\text{Tr}(\cdot) \equiv \sum_{N=0}^{\infty} \frac{1}{h^{dN} N!} \iint (\cdot) \, d\mathbf{r}^N \, d\mathbf{p}^N. \quad (2.3.6)$$

Moreover, the ensemble average in the grand canonical ensemble is given by

$$\langle B \rangle = \text{Tr}(fB), \quad (2.3.7)$$

where  $f$  is given in Eq. (2.3.3) and  $B$  is an arbitrary physical quantity.

## Grand Potential

The thermodynamic potential for a grand canonical system is called the grand free energy or grand potential,  $\Omega$ , which is defined in terms of the Helmholtz free energy [9]

$$\Omega = F - \bar{N}\mu, \quad (2.3.8)$$

where  $\bar{N} = \langle N \rangle$  is the average number of particles in the system [cf. Eq. (2.2.3) above]. Similar to Eq. (2.2.20), one can write the grand potential in differential form as

$$d\Omega = -SdT - \bar{N}d\mu - pdV. \quad (2.3.9)$$

Therefore, other thermodynamic functions can be written as derivatives of  $\Omega$ :

$$S = - \left( \frac{\partial \Omega}{\partial T} \right)_{\mu, V}, \quad \bar{N} = - \left( \frac{\partial \Omega}{\partial \mu} \right)_{T, V}, \quad p = - \left( \frac{\partial \Omega}{\partial V} \right)_{T, \mu}. \quad (2.3.10)$$

The grand potential reduces to

$$\Omega = -pV \quad (2.3.11)$$

when the internal energy is defined by Eq. (2.2.19). Furthermore, the thermodynamics of a grand canonical system can be linked to statistical mechanics [cf. Eq. (2.2.22)] by the grand partition function

$$\Omega = -k_B T \ln \Xi. \quad (2.3.12)$$

In a manner analogous to what we saw in Sec. 2.2, when the system is at the equilibrium state, the grand potential is a minimum. There are many more ensembles which we do not go into details in this thesis. Examples include the micro-canonical and isobaric ensemble with fixed quantities

$U, V, N$  and  $T, p, N$ , respectively. For more details see eg. Ref. [9].

## 2.4 Particle Densities and Pair Distribution Function

Similar to the canonical partition function, one can integrate the grand canonical partition function over the momenta to give

$$\Xi = \sum_{N=0}^{\infty} \frac{z^N}{N!} \int \exp[-\beta(V_N + \Phi_N)] d\mathbf{r}^N, \quad (2.4.1)$$

where  $z = \Lambda^{-d} \exp(\beta\mu)$  is the activity. Moreover, one can generate a hierarchy of particle distribution functions if we perform only a partial trace over the positions:

$$\rho^{(n)}(\mathbf{r}_1, \mathbf{r}_2, \dots, \mathbf{r}_n) = \frac{1}{\Xi} \sum_{N \geq n}^{\infty} \frac{z^N}{(N-n)!} \int \exp[-\beta(V_N + \Phi_N)] d\mathbf{r}^{(N-n)}. \quad (2.4.2)$$

The single-particle density can be obtained by setting  $n = 1$  which is same as the microscopic density profile,  $\rho^{(1)}(\mathbf{r}) = \langle \hat{\rho}(\mathbf{r}) \rangle = \rho(\mathbf{r})$  (where  $\hat{\rho}(\mathbf{r})$  is the density operator defined in Eq. (2.3.2)) and for a homogenous fluid (i.e. no external field) we get the bulk number density  $\rho^{(1)}(\mathbf{r}) = \rho$ , i.e. a constant. All the particle density distribution functions can be expressed in terms of  $\delta$ -functions. An example is the pair density, which can be written as

$$\rho^{(2)}(\mathbf{r}_1, \mathbf{r}_2) = \left\langle \sum_{i=1}^N \sum_{\substack{j=1 \\ j \neq i}}^N \delta(\mathbf{r}_1 - \mathbf{r}_i) \delta(\mathbf{r}_2 - \mathbf{r}_j) \right\rangle. \quad (2.4.3)$$

The quantity  $\rho^{(2)}(\mathbf{r}, \mathbf{r}') d\mathbf{r} d\mathbf{r}'$  is the probability that there is simultaneously a particle in the small volume  $d\mathbf{r}$  at  $\mathbf{r}$  and another in the volume  $d\mathbf{r}'$  at  $\mathbf{r}'$ .

The structure and the thermodynamic properties of liquids can be understood by introducing the hierarchy of distribution functions. The statistical information about the average distribution of particles in the liquid at a given state point is provided by these and the  $n$ -particle distribution, measuring the extent to which the structure of a fluid deviates from complete randomness, is defined

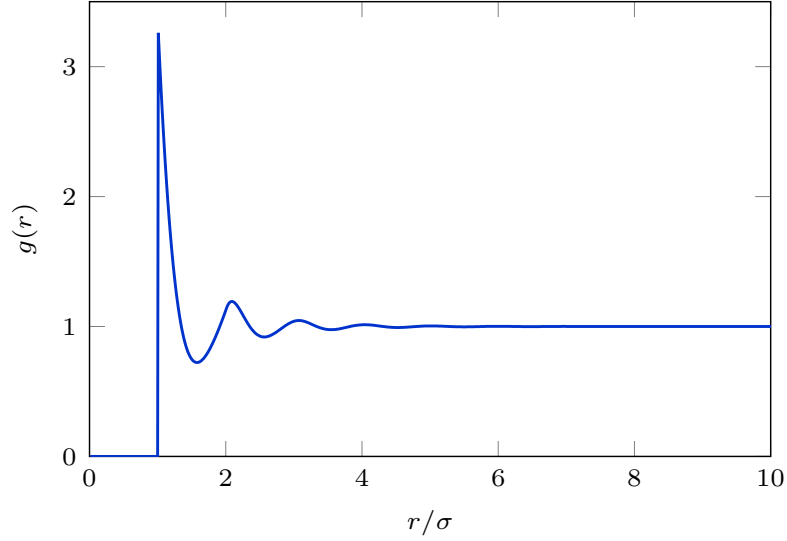


Figure 2.2: Radial distribution function  $g(r)$  for a hard sphere fluid, obtained using the Ornstein-Zernike equation and the Percus-Yevick closure, for the density  $\rho\sigma^3 = 0.75$ .

in terms of the  $n$ -particle densities as

$$g^{(n)}(\mathbf{r}_1, \mathbf{r}_2, \dots, \mathbf{r}_n) = \frac{\rho^{(n)}(\mathbf{r}_1, \mathbf{r}_2, \dots, \mathbf{r}_n)}{\prod_{i=1}^n \rho^{(1)}(\mathbf{r}_i)}, \quad (2.4.4)$$

which when the system is homogenous reduces to

$$\rho^n g^{(n)}(\mathbf{r}_1, \mathbf{r}_2, \dots, \mathbf{r}_n) = \rho^{(n)}(\mathbf{r}_1, \mathbf{r}_2, \dots, \mathbf{r}_n). \quad (2.4.5)$$

For a homogenous, isotropic system  $\rho^{(2)}$  can only depend on the relative separation  $|\mathbf{r}_1 - \mathbf{r}_2| \equiv r_{12}$ .

Hence, we have

$$\rho^{(2)}(\mathbf{r}_1, \mathbf{r}_2) = \rho^{(2)}(|\mathbf{r}_1 - \mathbf{r}_2|) = \rho^{(2)}(r_{12}) = \rho^2 g(r_{12}). \quad (2.4.6)$$

This introduces the radial (pair) distribution function  $g(r)$  which is particularly important in the physics of fluids. Crystalline solids have long ranged structural order, as the atoms are arranged into their lattice sites. In contrast, in the gas, the particles are uniformly spread in space with no long range order and only has very short range correlations between the positions of the particles. The liquid has no long range order, but does have short range structure. For all the states, Pauli exclusion repulsion between atoms makes  $g(r)$  vanish as  $r \rightarrow 0$  and in all fluids  $g(r) \rightarrow 1$  as  $r \rightarrow \infty$ .

An example of the radial distribution function for a hard sphere fluid calculated using the Ornstein-Zernike equation and the Percus-Yevick closure (see below) for the density  $\rho\sigma^3 = 0.75$  is shown in Fig. 2.2. Note that the ideal gas has  $g(r) = 1, \forall r$ .

## 2.5 Ornstein-Zernike Equation and Closure Relations

The total pair correlation function  $h^{(2)}(\mathbf{r}_1, \mathbf{r}_2)$  is defined in terms of the pair distribution function  $g^{(2)}(\mathbf{r}_1, \mathbf{r}_2)$  as

$$h^{(2)}(\mathbf{r}_1, \mathbf{r}_2) = g^{(2)}(\mathbf{r}_1, \mathbf{r}_2) - 1, \quad (2.5.1)$$

which vanishes as  $|\mathbf{r}_1 - \mathbf{r}_2| \rightarrow \infty$ . The *Ornstein-Zernike (OZ) equation* gives another correlation function  $c^{(2)}(\mathbf{r}_1, \mathbf{r}_2)$ , relating the total pair correlation function and the single particle density

$$h^{(2)}(\mathbf{r}_1, \mathbf{r}_2) = c^{(2)}(\mathbf{r}_1, \mathbf{r}_2) + \int c^{(2)}(\mathbf{r}_1, \mathbf{r}_3)\rho^{(1)}(\mathbf{r}_3)h^{(2)}(\mathbf{r}_3, \mathbf{r}_2) d\mathbf{r}_3. \quad (2.5.2)$$

The OZ equation represents the total pair correlation function as sum of a ‘direct’ correlation between particles 1 and 2 and the ‘indirect’ correlation via the other particles. Recursively using Eq. (2.5.2) makes the indirect correlation between the particles more obvious:

$$\begin{aligned} h^{(2)}(\mathbf{r}_1, \mathbf{r}_2) &= c^{(2)}(\mathbf{r}_1, \mathbf{r}_2) + \int c^{(2)}(\mathbf{r}_1, \mathbf{r}_3)\rho^{(1)}(\mathbf{r}_3)c^{(2)}(\mathbf{r}_3, \mathbf{r}_2) d\mathbf{r}_3 \\ &+ \iint c^{(2)}(\mathbf{r}_1, \mathbf{r}_3)\rho^{(1)}(\mathbf{r}_3)c^{(2)}(\mathbf{r}_3, \mathbf{r}_4)\rho^{(1)}(\mathbf{r}_4)c^{(2)}(\mathbf{r}_4, \mathbf{r}_2) d\mathbf{r}_3 d\mathbf{r}_4 + \dots \end{aligned} \quad (2.5.3)$$

Since we do not know what the pair direct correlation function  $c^{(2)}(r)$  is, the OZ equation does not by itself enable us to find the total correlation function  $h^{(2)}(r)$ . If we assume the particles are interacting via a pair potential  $V(r)$ , the exact closure relation is defined as

$$c^{(2)}(r) = h^{(2)}(r) - \ln[g^{(2)}(r)] - \beta V(r) + B(r) \quad (2.5.4)$$

where  $B(r)$  is the bridge function which is almost never known exactly [2]. The origin of Eq. (2.5.4) is discussed below in chapter 6. For purely repulsive pair potentials, such as the Yukawa potential,

a fairly good approximation is to set the bridge function  $B(r) = 0$  such that

$$c_{\text{HNC}}^{(2)}(r) = h^{(2)}(r) - \ln[g^{(2)}(r)] - \beta V(r). \quad (2.5.5)$$

This is called the *hypernetted-chain* (HNC) approximation closure [9]. For fluids with sharply repulsive cores and short ranged potentials one could use the *Percus-Yevick* (PY) approximation closure relation defined as

$$c_{\text{PY}}^{(2)}(r) = (1 - \exp[-\beta V(r)])(h^{(2)}(r) + 1). \quad (2.5.6)$$

The radial distribution function displayed in Fig. 2.2 is calculated using the Percus-Yevick closure along with the Ornstein-Zernike equation. There are many other closure approximations – see Ref. [9].

## 2.6 Static Structure Factor

The Fourier transform of the density operator,  $\hat{\rho}(\mathbf{r})$  [cf. Eq. (2.3.2)], is given as

$$\rho_{\mathbf{k}} = \int \hat{\rho}(\mathbf{r}) \exp(-i\mathbf{k} \cdot \mathbf{r}) \, d\mathbf{r} = \sum_{j=1}^N \exp(-i\mathbf{k} \cdot \mathbf{r}_j). \quad (2.6.1)$$

From this, the structure factor  $S(\mathbf{k})$  is defined as

$$S(\mathbf{k}) = \left\langle \frac{1}{N} \rho_{\mathbf{k}} \rho_{-\mathbf{k}} \right\rangle. \quad (2.6.2)$$

The structure factor is a useful quantity because one can measure it directly in experiments using neutron scattering or X-ray diffraction and is the density response of a system, initially in equilibrium, to a weak external perturbation of wavelength  $2\pi/k$ . Moreover, a relationship can be obtained between the structure factor and radial distribution function  $g(\mathbf{r})$  for a homogenous fluid

$$S(\mathbf{k}) = 1 + \rho \int [g(\mathbf{r}) - 1] \exp(-i\mathbf{k} \cdot \mathbf{r}) \, d\mathbf{r}. \quad (2.6.3)$$

The Fourier Transform of the total correlation function  $\hat{h}(\mathbf{k})$  can be used to express the above equation in a simple way:

$$S(\mathbf{k}) = 1 + \rho \hat{h}(\mathbf{k}). \quad (2.6.4)$$

Furthermore, a link to thermodynamics can be provided via the isothermal compressibility  $\chi_T$  using the long wavelength limit of the structure factor:

$$\chi_T \equiv \frac{1}{\rho} \left( \frac{\partial \rho}{\partial p} \right)_T = \frac{\beta S(0)}{\rho}. \quad (2.6.5)$$

It is important to note that the structure factor depends on direction which enables us to detect a change in the structure of pattern forming fluids (see chapter 7), hence the use of the vectorial  $\mathbf{k}$ .

## Chapter 3

# Density Functional Theory

*Once we can calculate the partition function,  $Z$ , we should in principle be able to get all the thermodynamic quantities of the system. However, it is not always possible to calculate the exact value of the partition function, since the partition function is a sum over all the possible configurations of the system. Thus an approximation is often required. Using density functional theory (DFT), we can overcome this problem by developing a good approximation for the free energy as a functional of the density profile  $\rho(\mathbf{r})$  and obtain a theory for the structure and thermodynamics of the system.*

In density functional theory (DFT), the grand free energy of a system is expressed as a functional of the average density at point  $\mathbf{r}$ . The functional has a minimum at the equilibrium density. The thermodynamics properties, such as surface tension, can be calculated using the equilibrium density. Refs. [9, 18, 19, 20, 21] give good background information and introduction to DFT. The presentation here leans heavily on these.

### 3.1 Intrinsic Free Energy

In DFT, the Helmholtz free energy of a system is expressed as a functional of the average density at point  $\mathbf{r}$ . Recall that the density profile of the system is defined as  $\rho(\mathbf{r}) = \langle \hat{\rho}(\mathbf{r}) \rangle$ , where  $\hat{\rho}(\mathbf{r})$ , the density operator, is defined in Eq. (2.3.2). Therefore, the contribution to the energy due to the external potential,  $\Phi_N$ , is the following average:

$$\langle \Phi_N \rangle = \int \rho(\mathbf{r}) \phi(\mathbf{r}) \, d\mathbf{r}, \quad (3.1.1)$$

since the total external potential for any given configuration is given by [cf: Eq. (2.0.4)]

$$\Phi_N(\mathbf{r}^N) = \sum_{i=1}^N \phi(\mathbf{r}_i) = \int \hat{\rho}(\mathbf{r})\phi(\mathbf{r}) \, d\mathbf{r}. \quad (3.1.2)$$

The contribution to the Helmholtz free energy of the system not including the contribution from the external field is called the intrinsic Helmholtz free energy,  $\mathcal{F}$ . Using Eq. (3.1.1), the intrinsic free energy,  $\mathcal{F}$ , can be written in terms of Helmholtz free energy:

$$\mathcal{F} = F - \langle \Phi_N \rangle = F - \int \rho(\mathbf{r})\phi(\mathbf{r}) \, d\mathbf{r}. \quad (3.1.3)$$

It is one of the important results of DFT that  $\mathcal{F}$  does not depend on the external potential,  $\Phi_N$ , and solely depends on the form of the interaction potentials between the particles [9, 19]. If there are no interactions between particles and no external potential, i.e.  $V_N = \Phi_N = 0$ , then the configurational integral (2.2.16) becomes

$$Q = \frac{1}{N!} \int d\mathbf{r}^N = \frac{V^N}{N!} \quad (3.1.4)$$

Using Sterling's formula,

$$\ln N! = \ln 1 + \ln 2 + \dots + \ln N \approx \int_1^N \ln x \, dx = N \ln N - N, \quad (3.1.5)$$

which is valid for large  $N$ , and using Eqs. (2.2.22) and (3.1.3), we can calculate the intrinsic free energy for an ideal gas,  $\mathcal{F}_{\text{id}}$ :

$$\begin{aligned} \mathcal{F}_{\text{id}} &= k_B T \ln \left( \frac{N! \Lambda^{dN}}{V^N} \right) \\ &= k_B T N \left( \ln \left[ \Lambda^d \frac{N}{V} \right] - 1 \right) \\ &= k_B T \int \rho(\mathbf{r}) \left( \ln[\Lambda^d \rho(\mathbf{r})] - 1 \right) \, d\mathbf{r}. \end{aligned} \quad (3.1.6)$$

Note that the total number of particles in the system  $N = \int \rho(\mathbf{r}) \, d\mathbf{r}$ . In going from the second to the third line in Eq. (3.1.6) we have assumed that the density is a constant  $\rho(\mathbf{r}) = \rho = N/V$ . However, the result in the last line of Eq. (3.1.6) is actually also true for an inhomogeneous ideal-gas.

The interaction between the particles can be included in the excess free energy,  $\mathcal{F}_{\text{ex}}$ , which together with the intrinsic free energy of the ideal gas,  $\mathcal{F}_{\text{id}}$ , forms the total intrinsic free energy:

$$\mathcal{F} = \mathcal{F}_{\text{id}} + \mathcal{F}_{\text{ex}}. \quad (3.1.7)$$

### 3.2 Grand Potential Functional

The grand potential,  $\Omega = F - \bar{N}\mu$ , can be expressed in terms of the intrinsic free energy,  $\mathcal{F}$ , using Eq. (3.1.3), such that

$$\begin{aligned} \Omega &= \mathcal{F} + \int \rho(\mathbf{r})\phi(\mathbf{r}) \, \text{d}\mathbf{r} - \bar{N}\mu. \\ &= \mathcal{F} - \int \rho(\mathbf{r})u(\mathbf{r}) \, \text{d}\mathbf{r}, \end{aligned} \quad (3.2.1)$$

where  $u(\mathbf{r}) \equiv \mu - \phi(\mathbf{r})$ . It is natural to consider the intrinsic free energy,  $\mathcal{F}$ , and the grand potential,  $\Omega$  as functionals of the density profile,  $\rho(\mathbf{r})$ . We use the notations  $\mathcal{F}[\rho]$  and  $\Omega[\rho]$  to represent the functional dependencies. Therefore, performing the Legendre transform of  $\mathcal{F}$  we obtain the functional:

$$\hat{\Omega}[\rho(\mathbf{r})] = k_B T \int \rho(\mathbf{r}) \left( \ln[\Lambda^d \rho(\mathbf{r})] - 1 \right) \, \text{d}\mathbf{r} + \mathcal{F}_{\text{ex}} - \int \rho(\mathbf{r})u(\mathbf{r}) \, \text{d}\mathbf{r}. \quad (3.2.2)$$

Recall that the equilibrium state of a grand canonical system corresponds to the minimum of the grand potential [19, 22]. It is a central result of DFT that the grand potential functional has a unique minimum corresponding to the density profile,  $\rho_0(\mathbf{r})$ , such that the system is in equilibrium [9]. In this case the grand potential functional gives the grand potential of the system, i.e.

$$\hat{\Omega}[\rho_0(\mathbf{r})] = \Omega. \quad (3.2.3)$$

It is important to note that (proof in Ref. [9]):

$$\hat{\Omega}[\rho(\mathbf{r})] \geq \Omega, \quad (3.2.4)$$

And the minimum value only occurs when  $\rho(\mathbf{r}) = \rho_0(\mathbf{r})$ . Thus, the central aim in DFT is to find the minimum of the grand potential functional, by solving the Euler-Lagrange equation

$$\left. \frac{\delta \hat{\Omega}[\rho(\mathbf{r})]}{\delta \rho(\mathbf{r})} \right|_{\rho(\mathbf{r})=\rho_0(\mathbf{r})} = 0. \quad (3.2.5)$$

Taking the functional derivative of the grand potential functional, Eq. (3.2.2), yields

$$\frac{\delta \hat{\Omega}[\rho(\mathbf{r})]}{\delta \rho(\mathbf{r})} = k_B T \ln[\Lambda^d \rho(\mathbf{r})] + \frac{\delta \mathcal{F}_{\text{ex}}[\rho(\mathbf{r})]}{\delta \rho(\mathbf{r})} - u(\mathbf{r}) = 0. \quad (3.2.6)$$

Taking repeated functional derivatives of the excess functional,  $\mathcal{F}_{\text{ex}}[\rho]$ , with respect to the density profile generates a series of correlation functions. The first of these is the one-body direct correlation function, defined as [9, 18, 19]

$$c^{(1)}(\mathbf{r}) \equiv -\beta \frac{\delta \mathcal{F}_{\text{ex}}[\rho(\mathbf{r})]}{\delta \rho(\mathbf{r})}. \quad (3.2.7)$$

The second is the two-body direct correlation function

$$c^{(2)}(\mathbf{r}, \mathbf{r}') \equiv -\beta \frac{\delta^2 \mathcal{F}_{\text{ex}}[\rho(\mathbf{r})]}{\delta \rho(\mathbf{r}) \delta \rho(\mathbf{r}')}, \quad (3.2.8)$$

and taking  $n$ -derivatives yields in an analogous way the  $n$ -body direct correlation function

$$c^{(n)}(\mathbf{r}_1, \mathbf{r}_2, \dots, \mathbf{r}_n).$$

The form of the excess free energy functional  $\mathcal{F}_{\text{ex}}[\rho]$  is determined by the nature of the interactions between the particles,  $V_N$ . The form of these varies, depending on the type of system being considered.

### 3.3 Fundamental Measure Theory for Hard Spheres

The density functional (3.2.2) can be written as

$$\Omega[\rho] = \mathcal{F}_{\text{id}}[\rho] + \mathcal{F}_{\text{ex}}[\rho] - \int \rho(\mathbf{r}) u(\mathbf{r}) \, d\mathbf{r}, \quad (3.3.1)$$

where  $\mathcal{F}_{\text{id}}$  is the ideal-gas free energy,  $\mathcal{F}_{\text{ex}}$  is the excess free energy and  $u(\mathbf{r}) \equiv \mu - \phi(\mathbf{r})$ . Recall that  $\mu$  is the chemical potential and  $\phi$  is the external potential. All the terms except the excess

free energy,  $\mathcal{F}_{\text{ex}}$ , which is the free energy contribution arising from the interactions between the particles, are known. This section shows some approximations for the excess free energy for a fluid of hard-spheres interacting via the potential (2.1.1) and follows the excellent review by Roth [23].

The excess free energy functional can be written in terms of the local excess free energy per particle  $f_{\text{ex}}(\mathbf{r})$ :

$$\mathcal{F}_{\text{ex}} = \int \rho(\mathbf{r}) f_{\text{ex}}(\mathbf{r}) \, \text{d}\mathbf{r}. \quad (3.3.2)$$

For one-dimensional (1D) hard rods, it can be proved that  $f_{\text{ex}}$  is a function of a weighted density (see chapter 6) and therefore it is sensible to assume that the theory retains this structure for 3D systems. This is a well trodden route for developing approximations. For example, the weighted density approximation (WDA), by Curtin and Ashcroft [24], for the excess free energy functional is defined as

$$\mathcal{F}_{\text{ex}}^{\text{WDA}} = \int \rho(\mathbf{r}) f_{\text{ex}}^0(\bar{\rho}(\mathbf{r})) \, \text{d}\mathbf{r}, \quad (3.3.3)$$

where  $f_{\text{ex}}^0(\bar{\rho})$ , is the excess free energy per particle for a uniform fluid. The weighted average of the physical density  $\rho(\mathbf{r})$  with respect to a weight function, is called the weighted density,  $\bar{\rho}(\mathbf{r})$ , which is defined as

$$\bar{\rho}(\mathbf{r}) = \int w(\mathbf{r} - \mathbf{r}') \rho(\mathbf{r}') \, \text{d}\mathbf{r}'. \quad (3.3.4)$$

The weight function,  $w$ , must satisfy the normalisation condition

$$\int w(|\mathbf{r} - \mathbf{r}'|) \, \text{d}\mathbf{r}' = 1. \quad (3.3.5)$$

Choosing the appropriate weight functions causes some difficulty in implementing the WDA method. The WDA looks at the local excess free energy, which lead to the formulation of modified-WDA which starts with the global excess free energy. Further extensions were then made to the approximation to include both local and global contributions to the excess free energy [18]. The real breakthrough in this approach came with the development of fundamental measure theory by Rosenfeld. These theories have become the basis of almost all modern work.

For particles interacting via the pair potential,  $V(r)$ , one can show that the virial expansion of

the excess free energy,  $\mathcal{F}_{\text{ex}}$ , at low densities yields

$$\beta\mathcal{F}_{\text{ex}} = -\frac{1}{2} \iint \rho(\mathbf{r})\rho(\mathbf{r}')f(|\mathbf{r} - \mathbf{r}'|) d\mathbf{r} d\mathbf{r}' + \mathcal{O}(\rho^3), \quad (3.3.6)$$

where,  $f(r)$  is the Mayer- $f$  function defined by [9]

$$f(r) = e^{-\beta V(r)} - 1. \quad (3.3.7)$$

The Mayer- $f$  function has the useful property that when  $r = |\mathbf{r} - \mathbf{r}'| \rightarrow \infty$  then  $f \rightarrow 0$ . In this section, we consider fluids of particles of radius  $R = \sigma/2$  interacting via the hard-sphere pair potential (2.1.1). The Mayer- $f$  function thus becomes

$$f(r) = \begin{cases} -1 & \text{if } r < 2R \\ 0 & \text{otherwise.} \end{cases} \quad (3.3.8)$$

In his breakthrough paper, Rosenfeld [25] was able to decompose the Mayer- $f$  function for hard spheres, using a set of weight functions, such that

$$-f(r) = w_3 \otimes w_0 + w_0 \otimes w_3 + w_2 \otimes w_1 + w_1 \otimes w_2 - \vec{w}_2 \otimes \vec{w}_1 - \vec{w}_2 \otimes \vec{w}_1, \quad (3.3.9)$$

where the convolution of the weight functions is denoted by the symbol  $\otimes$ , defined as

$$w_\alpha \otimes w_\beta(\mathbf{r}) = \int w_\alpha(\mathbf{r}')w_\beta(\mathbf{r} - \mathbf{r}') d\mathbf{r}'. \quad (3.3.10)$$

The scalar and vector weight functions are given by

$$w_3(\mathbf{r}) = \Theta(R - |\mathbf{r}|), \quad (3.3.11)$$

$$w_2(\mathbf{r}) = \delta(R - |\mathbf{r}|), \quad (3.3.12)$$

$$\vec{w}_2(\mathbf{r}) = \frac{\mathbf{r}}{|\mathbf{r}|} \delta(R - |\mathbf{r}|), \quad (3.3.13)$$

$$w_1(\mathbf{r}) = \frac{w_2(\mathbf{r})}{4\pi R}, \quad (3.3.14)$$

$$w_0(\mathbf{r}) = \frac{w_2(\mathbf{r})}{4\pi R^2}, \quad (3.3.15)$$

$$\vec{w}_1(\mathbf{r}) = \frac{\vec{w}_2(\mathbf{r})}{4\pi R}. \quad (3.3.16)$$

Here,  $\Theta(r)$  is the Heaviside step function and  $\delta(r)$  is the Dirac- $\delta$  function. Integration over the different weight functions  $w_\alpha(r)$  results in expressions for the volume  $V$ , surface area  $S$ , radius of curvature  $R$  and Euler characteristics of the particles (spheres), which are the ‘fundamental geometric measures’ of a sphere for  $\alpha = 3$ ,  $\alpha = 2$ ,  $\alpha = 1$  and  $\alpha = 0$ , respectively. This property leads to the name ‘fundamental measure theory’ and also the connection that the Mayer- $f$  function for hard-spheres has a geometric interpretation.

Another way to decompose the Mayer- $f$  is

$$-f(r) = w_3 \otimes \tilde{w}_0 + \tilde{w}_0 \otimes w_3 + w_2 \otimes \tilde{w}_1 + \tilde{w}_1 \otimes w_2, \quad (3.3.17)$$

where the weight functions  $w_3$  and  $w_2$  are same as the Rosenfeld’s weights. This decomposition avoids the use of the vector weight functions. The remaining weight functions,  $\tilde{w}_1$  and  $\tilde{w}_0$  are given in terms of the derivatives of the Dirac- $\delta$  function,

$$\tilde{w}_1(\mathbf{r}) = \frac{1}{8\pi} \delta'(R - |\mathbf{r}|), \quad (3.3.18)$$

$$\tilde{w}_0(\mathbf{r}) = -\frac{1}{8\pi} \delta''(R - |\mathbf{r}|) + \frac{1}{2\pi|\mathbf{r}|} \delta'(R - |\mathbf{r}|). \quad (3.3.19)$$

However, it has been shown that both the decomposition in Eq. (3.3.9) and that in Eq. (3.3.17) are

equivalent.

The weighted densities,  $n_\alpha(\mathbf{r})$ , are calculated such that one can recover the excess free energy in Eq. (3.3.6), exactly at a low density:

$$\lim_{\rho \rightarrow 0} \beta \mathcal{F}_{\text{ex}} = -\frac{1}{2} \iint \rho(\mathbf{r}) \rho(\mathbf{r}') f(|\mathbf{r} - \mathbf{r}'|) \, d\mathbf{r} \, d\mathbf{r}' \quad (3.3.20)$$

$$= \int [n_0(\mathbf{r})n_3(\mathbf{r}) + n_1(\mathbf{r})n_2(\mathbf{r}) - \vec{n}_1(\mathbf{r}) \cdot \vec{n}_2(\mathbf{r})] \, d\mathbf{r}. \quad (3.3.21)$$

This leads the weighted densities to be defined as the convolution of the density profile with each of the different weight functions

$$n_\alpha(\mathbf{r}) = \int \rho(\mathbf{r}') w_\alpha(\mathbf{r} - \mathbf{r}') \, d\mathbf{r}'. \quad (3.3.22)$$

It should be noted that for a uniform fluid with bulk density  $\rho_b$ , both of the vector weighted densities reduce to zero.

The excess free energy functional  $\mathcal{F}_{\text{ex}} = \mathcal{F}_{\text{ex}}^{\text{HS}}$  (since we only consider the hard spheres), can be written in the form

$$\mathcal{F}_{\text{ex}}^{\text{HS}} = \int \Phi(n_\alpha(\mathbf{r})) \, d\mathbf{r}, \quad (3.3.23)$$

where,  $\Phi$  is a function of the weighted densities, called the reduced free energy density, for which the following ansatz was used

$$\Phi = f_1(n_3)n_0 + f_2(n_3)n_1n_2 + f_3(n_3)\vec{n}_1 \cdot \vec{n}_2 + f_4(n_3)n_2^3 + f_5(n_3)n_2\vec{n}_2 \cdot \vec{n}_2. \quad (3.3.24)$$

Note that the  $\mathbf{r}$  dependence of the weighted densities is dropped henceforth for brevity. The unknown

functions,  $f_1, \dots, f_5$ , have expansions

$$f_1 = n_3 + \mathcal{O}(n_3^2) \quad (3.3.25)$$

$$f_2 = 1 + \mathcal{O}(n_3) \quad (3.3.26)$$

$$f_3 = -1 + \mathcal{O}(n_3) \quad (3.3.27)$$

$$f_4 = \frac{1}{24\pi} + \mathcal{O}(n_3) \quad (3.3.28)$$

$$f_5 = -\frac{3}{24\pi} + \mathcal{O}(n_3) \quad (3.3.29)$$

Since the two decompositions of the Mayer- $f$  function are equivalent, the ansatz reduces to

$$\Phi = f_1(n_3)n_0 + f_2(n_3)(n_1n_2 - \vec{n}_1 \cdot \vec{n}_2) + f_4(n_3)(n_2^3 - 3n_2\vec{n}_2 \cdot \vec{n}_2), \quad (3.3.30)$$

due to the following conditions

$$f_3(n_3) = -f_2(n_3) \quad (3.3.31)$$

$$f_5(n_3) = -3f_4(n_3). \quad (3.3.32)$$

Rosenfeld was able to calculate the unknown functions, using the scaled particle theory equation [26]

$$\lim_{R \rightarrow \infty} \frac{\beta\mu_{\text{ex}}}{\mathcal{V}} = \beta p. \quad (3.3.33)$$

where  $R$  and  $\mathcal{V}$  are the radius and the volume of the sphere respectively,  $\mu_{\text{ex}}$  is the excess chemical

potential and  $p$  is the pressure. Rosenfeld found the functions to be

$$f_1^{\text{RF}}(n_3) = -\ln(1 - n_3) \quad (3.3.34)$$

$$f_2^{\text{RF}}(n_3) = \frac{1}{1 - n_3} \quad (3.3.35)$$

$$f_4^{\text{RF}}(n_3) = \frac{1}{24\pi(1 - n_3)^2}. \quad (3.3.36)$$

Hence, the excess free energy density can be written as

$$\Phi^{\text{RF}} = -n_0 \ln(1 - n_3) + \frac{n_1 n_2 - \vec{n}_1 \cdot \vec{n}_2}{1 - n_3} + \frac{n_2^3 - 3n_2 \vec{n}_2 \cdot \vec{n}_2}{24\pi(1 - n_3)^2}. \quad (3.3.37)$$

However, this is not the only way to find the unknown functions,  $f_1$ ,  $f_2$  and  $f_4$ . The White-Bear version of FMT [27] uses the same functions  $f_1$  and  $f_2$  as the Rosenfeld version, but with the function  $f_4$  given by

$$f_4(n_3) = \frac{n_3 + (1 - n_3)^2 \ln(1 - n_3)}{36\pi n_3^2 (1 - n_3)^2}. \quad (3.3.38)$$

Therefore, using Eq. (3.3.30) one can write the excess free energy density as

$$\Phi^{\text{WB}} = -n_0 \ln(1 - n_3) + \frac{n_1 n_2 - \vec{n}_1 \cdot \vec{n}_2}{1 - n_3} + (n_2^3 - 3n_2 \vec{n}_2 \cdot \vec{n}_2) \frac{n_3 + (1 - n_3)^2 \ln(1 - n_3)}{36\pi n_3^2 (1 - n_3)^2}. \quad (3.3.39)$$

The one-body correlation function given in Eq. (3.2.7) can thus be written as

$$c^{(1)}(\mathbf{r}) = -\beta \frac{\delta \mathcal{F}_{\text{ex}}[\rho(\mathbf{r})]}{\delta \rho(\mathbf{r})} = -\sum_{\alpha} \int d\mathbf{r}' \frac{\partial \Phi(\{n_{\alpha}\})}{\partial n_{\alpha}} \frac{\delta n_{\alpha}(\mathbf{r}')}{\delta \rho(\mathbf{r})}. \quad (3.3.40)$$

To calculate the equilibrium fluid density profile, the above expression is input into the Euler-Lagrange equation (3.2.6). By splitting the chemical potential  $\mu = \mu_{\text{id}} + \mu_{\text{ex}}$  into the ideal gas contribution  $\mu_{\text{id}} = \beta^{-1} \ln \lambda^3 \rho_b$ , where  $\rho_b$  is the bulk density, and the excess contribution  $\mu_{\text{ex}} = -\beta c^{(1)}(\infty) = -\beta c^{(1)}[\rho_b]$ , we can re-write the Euler-Lagrange equation as

$$\rho(\mathbf{r}) = \rho_b \exp(-\beta V_{\text{ext}}(\mathbf{r}) + c^{(1)}(\mathbf{r}) + \beta \mu_{\text{ex}}). \quad (3.3.41)$$

This is the equation we work with to self-consistently solve for the density profile. In all the

DFT calculations in this thesis, the density functional, Eq. (3.2.2), was minimised using Picard iteration [28]. The Picard iteration is done via the following algorithm:

1. Initialise the density profile with ideal-gas profile  $\rho^{(0)}(\mathbf{r}) = \rho_b \exp(-\beta V_{\text{ext}}(\mathbf{r}))$ , or a profile previously obtained for a near-by state point.
2. A new density profile,  $\rho^{\text{new}}(\mathbf{r})$ , is calculated using Eq. (3.3.41).
3. The new density is updated by mixing with the previous density via a mixing parameter  $\alpha$ :  

$$\rho^{(l)}(\mathbf{r}) = \alpha \rho^{\text{new}}(\mathbf{r}) + (1 - \alpha) \rho^{(l-1)}(\mathbf{r}).$$
4. Go to Step 2 until the solution is converged.

Here,  $l$  is the iteration step and the mixing parameter  $\alpha \in [0, 1]$ . Too large a value of the mixing parameter  $\alpha$  leads to instabilities in the iteration and can end up with unphysical density distributions such as negative densities, whilst if  $\alpha$  is too small, it leads to slow convergence. In simple DFT calculations,  $\alpha$  taking a value in the range (0.01, 0.2) is typical. Nevertheless, a smart choice of the mixing parameter can improve the convergence. One such optimal way of finding the mixing parameter  $\alpha$  is described in Ref. [23] which calculates a new  $\alpha$  at each iteration.

For the DFT calculations presented below in chapter 5, we use the White-Bear version of FMT [27] to approximate the excess free energy functional. In bulk, the White-Bear generates the Carnahan-Starling equation of state, which is slightly more accurate than that of the original Rosenfeld functional. The convolutions for both the weighted densities and the one-body direct correlation function, can be performed in Fourier space if the system is periodic. Non-periodic systems are made periodic by making the system so large such that there are no wrap-around effects from structures interacting with their own periodic image. Note that Eq. (3.3.39) becomes undefined if  $n_3(\mathbf{r}) \geq 1$  at any value of  $\mathbf{r}$ . If during the iteration this occurs, it can lead to a break down of the numerical method.

### 3.4 Mean-Field Approximation for Attraction

So far, we have considered a purely repulsive hard sphere system with pair potential,  $V_{\text{HS}}$ . However, in reality most fluids are not composed of purely repulsive (hard) particles. Therefore, to go beyond

hard spheres, we have to describe particles with an additional attraction. This is done by treating the attraction as a perturbation to the interaction between the particles such that the overall potential due to the interactions between two particles is

$$V(\mathbf{r}, \mathbf{r}') = V_r(\mathbf{r}, \mathbf{r}') + \lambda V_p(\mathbf{r}, \mathbf{r}') \quad 0 \leq \lambda \leq 1, \quad (3.4.1)$$

where  $V_r$  is the pair potential of reference fluid,  $V_p$  is the perturbation potential and  $\lambda$  is the “charging” parameter such that it has value of 0 when it is the reference system and 1 for the full system. If we take the functional derivative of the excess free energy,  $\mathcal{F}_{\text{ex}}$ , with respect to pair potential,  $V(\mathbf{r}, \mathbf{r}')$ , and then formally integrate back up again, we obtain the following expression for the excess free energy

$$\mathcal{F}_{\text{ex}} = \mathcal{F}_{\text{ex}}^r + \frac{1}{2} \int_0^1 \iint \frac{\delta \mathcal{F}}{\delta V(\mathbf{r}, \mathbf{r}')} V_p(\mathbf{r}, \mathbf{r}') \, d\mathbf{r} \, d\mathbf{r}' \, d\lambda. \quad (3.4.2)$$

where  $\mathcal{F}_{\text{ex}}^r$  is the intrinsic free energy of the the reference fluid. It can be shown that the functional derivative can be written as

$$\frac{\delta \mathcal{F}}{\delta V(\mathbf{r}, \mathbf{r}')} = \frac{1}{2} \rho(\mathbf{r}) \rho(\mathbf{r}') g(\mathbf{r}, \mathbf{r}'), \quad (3.4.3)$$

where  $g(\mathbf{r}, \mathbf{r}')$  is the radial distribution function for the inhomogeneous fluid. Making the rather crude but surprisingly effective approximation in this integral that  $g(\mathbf{r}, \mathbf{r}') \approx 1$ , the intrinsic excess free energy,  $\mathcal{F}_{\text{ex}}$ , can be written as

$$\mathcal{F}_{\text{ex}} = \mathcal{F}_{\text{ex}}^r + \mathcal{F}_{\text{ex}}^p, \quad (3.4.4)$$

where, the energy contribution due to the perturbation potential is given by

$$\mathcal{F}_{\text{ex}}^p = \frac{1}{2} \iint \rho(\mathbf{r}) \rho(\mathbf{r}') V_p(|\mathbf{r} - \mathbf{r}'|) \, d\mathbf{r} \, d\mathbf{r}'. \quad (3.4.5)$$

This approximation (sometimes termed as the van der Waals theory of non-uniform fluids) is the basis of almost all perturbation theories. The above mean-field like approximation is implemented throughout this thesis with the reference pair potential that we use being given by the hard sphere potential – i.e. we assume  $V_r \approx V_{\text{HS}}$ . In chapter 6 we return to Eq. (3.4.5) and discuss in greater detail the physical content of this approximation.

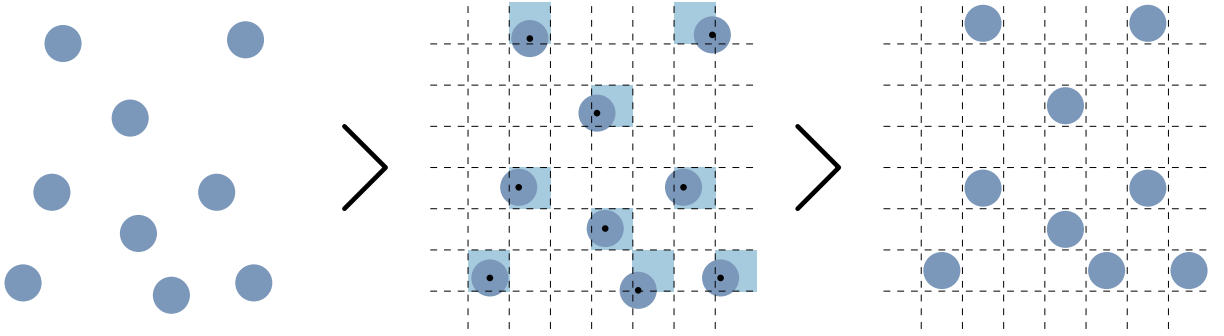


Figure 3.1: Starting with a given continuum configuration of particles, we can create a corresponding lattice model by mapping the centre of each particle to a lattice site on a grid.

### 3.5 Lattice DFT

In the previous sections we described continuum DFT, for systems of particles that can be in any position within space. One can transfer a continuum model into a discrete lattice model by mapping the centre of each particle to a lattice site, as shown in Fig. 3.1. This approximation greatly simplifies the description of the fluid and allows one to develop an understanding of the fluid structure at larger length scales than the full continuum theories. This section follows closely the presentation of Ref. [28].

We denote a particular configuration of particles by a set of occupation numbers  $\{m_i\}$ , such that, if the site  $i$  is empty then  $m_i = 0$  and  $m_i = 1$  otherwise – i.e. we have assumed that the lattice sites contain no more than 1 particle. It is important to note that  $i$  here is used as a short form for the lattice point with position  $(j, k)$  where  $j$  and  $k$  are integers, since the lattice we consider is two-dimensional (2D). Hence, the configurational part of the Hamiltonian is given by [cf. Eq. (2.0.1)]

$$E(\{m_i\}) = \sum_{i=1}^M m_i \Phi_i + \frac{1}{2} \sum_{i,j} V_{i,j} m_i m_j \quad (3.5.1)$$

where  $\Phi_i$  is the external potential at the lattice site  $i$  and the energy contribution due to the interactions between particles is given by the second term. Here,  $V_{i,j}$  is the pair potential of two particles at sites  $i$  and  $j$ . Akin to the continuum version, we have assumed that there are no three-body or higher-body interactions.

The probability, Eq. (2.2.1), of being in a particular configuration  $\{m_i\}$  for the lattice model is

now given by

$$P(\{m_i\}) = \frac{e^{-\beta E(\{m_i\})}}{Z}, \quad (3.5.2)$$

with  $Z$  being the partition function. Since the sum of all probabilities must be 1, the partition function of the lattice model is

$$Z = \sum_{\text{all states}} e^{-\beta E_{\text{state}}}, \quad (3.5.3)$$

where ‘state’ is short hand for a particular configuration  $\{m_i\}$ . The partition function can also be written as  $Z = \text{Tr}^L(e^{-\beta E})$  where,

$$\text{Tr}^L x = \sum_{\text{all states}} x = \sum_{m_1=0}^1 \sum_{m_2=0}^1 \cdots \sum_{m_M=0}^1 x. \quad (3.5.4)$$

Calculating  $Z$  is rather tricky, however we can do it when  $V_{i,j} = 0$  (when the particles don’t interact with each other). To start with, we also set  $\Phi_i = 0 \forall i$  such that there is no external field (homogeneous fluid). Hence, from Eqs. (3.5.1) and (3.5.2) we have  $P\{m_i\} = 1/Z$ . This shows that there is equal probability for all configurations to occur. Consider the case when there are  $N$  particles in the system that are identical and there are  $M$  lattice sites where these particles can be placed. The total number of ways this can be done is the partition function in this case. Hence,

$$Z = \frac{M!}{N!(M-N)!}. \quad (3.5.5)$$

Substituting the above into the expression for the Helmholtz free energy in Eq. (2.2.22) and doing some rearranging we get

$$\beta F = -\ln M! + \ln N! + \ln(M-N)!. \quad (3.5.6)$$

Using Sterling’s formula (3.1.5) for large  $N$  we have

$$\beta F = -M \ln M + N \ln N + (M-N) \ln(M-N). \quad (3.5.7)$$

Also, note that the density of the particles in the system is the average number of particles per lattice site, i.e. the density  $\rho = N/M$ . Substituting this into the above equation and doing some

rearranging we get

$$\frac{\beta F}{M} = \rho \ln \rho + (1 - \rho) \ln(1 - \rho). \quad (3.5.8)$$

This result is for a homogenous fluid that has a uniform density  $\rho$  throughout. However, in an inhomogeneous fluid the density will vary spatially due to the external potential  $\Phi_i$ . The Helmholtz free energy of the inhomogeneous fluid can be approximated using the average density at site  $i$  as

$$\begin{aligned} \rho_i &= \langle m_i \rangle \quad (\text{statistical average}) \\ &= \text{Tr}^L m_i P_{\text{state}}. \end{aligned} \quad (3.5.9)$$

The probability of a particular state occurring in a grand canonical system is

$$P_{\text{state}} = \frac{1}{\Xi} e^{-\beta(E_{\text{state}} - \mu N)}, \quad (3.5.10)$$

where  $N$  is the total number of particles and the normalising factor is the grand partition function:

$$\Xi = \text{Tr}^L e^{-\beta(E_{\text{state}} - \mu N)}. \quad (3.5.11)$$

Rearranging the grand potential (2.3.12) such that

$$\Xi = e^{-\beta\Omega} \quad (3.5.12)$$

and equating to the above equation (3.5.11) gives

$$e^{-\beta\Omega} = \text{Tr}^L e^{-\beta(E_{\text{state}} - \mu N)}. \quad (3.5.13)$$

By choosing a reference system with Hamiltonian  $E_0$  that is inhomogeneous (i.e.  $\Phi_i \neq 0$ ) and with no interactions between neighbouring pairs of particles ( $V_{i,j} = 0$ ), and also rewriting the energy of a particular state,  $E = E_0 + E - E_0 = E_0 + \Delta E$ , we have

$$e^{-\beta\Omega} = \text{Tr}^L e^{-\beta(E_0 - \mu N)} e^{-\beta\Delta E}. \quad (3.5.14)$$

From Eq. (3.5.10) one has  $P_0 = e^{-\beta(E_0 - \mu N)} / \Xi_0$ . Hence, the statistical average value of any quantity  $x$  in the reference system is given by

$$\langle x \rangle_0 = \text{Tr}^L \left( \frac{e^{-\beta(E_0 - \mu N)}}{\Xi_0} x \right). \quad (3.5.15)$$

Therefore, from Eq. (3.5.12) one has  $\Xi_0 = e^{-\beta\Omega_0}$  and using Eq. (3.5.14) we obtain

$$e^{-\beta\Omega} = e^{-\beta\Omega_0} \langle e^{-\beta\Delta E} \rangle_0. \quad (3.5.16)$$

Moreover  $\langle e^{-x} \rangle \geq e^{-\langle x \rangle}$ , since  $e^{-x}$  is a convex function of  $x$ . Thus, we obtain the following inequality

$$e^{-\beta\Omega} \geq e^{-\beta\Omega_0} e^{-\beta\langle \Delta E \rangle_0}. \quad (3.5.17)$$

Taking the logarithm of the above equation gives the Gibbs-Bogoliubov inequality

$$\Omega \leq \Omega_0 + \langle \Delta E \rangle_0, \quad (3.5.18)$$

which shows that there exists an upper bound on the grand potential,  $\Omega$ , that depends only on the reference system  $E_0$ . This enables us to find an approximation for  $\Omega$  by minimising the right hand side of the inequality.

In order to carry on, we choose [cf. Eq. (3.5.1)]

$$E_0 = \sum_{i=1}^M (\Phi_i + \varphi_i) m_i \quad (3.5.19)$$

where  $\Phi_i$  is the external potential, and  $\varphi_i$  are set of parameters that for the moment are not determined. We will use them below as variational parameters to determine a best estimate for  $\Omega$ .

Now from Eq. (3.5.11)

$$\begin{aligned}
\Xi_0 &= \text{Tr}^L e^{-\beta(E_0 - \mu N)} \\
&= \sum_{m_1=0}^1 \sum_{m_2=0}^1 \cdots \sum_{m_M=0}^1 e^{-\beta \sum_{i=1}^M \gamma_i m_i} \\
&= \left[ \sum_{m_1=0}^1 e^{-\beta \gamma_1 m_1} \right] \left[ \sum_{m_2=0}^1 e^{-\beta \gamma_2 m_2} \right] \cdots \left[ \sum_{m_M=0}^1 e^{-\beta \gamma_M m_M} \right] \\
&= \left[ 1 + e^{-\beta \gamma_1} \right] \left[ 1 + e^{-\beta \gamma_2} \right] \cdots \left[ 1 + e^{-\beta \gamma_M} \right] \\
&= \prod_{i=1}^M \left( 1 + e^{-\beta \gamma_i} \right)
\end{aligned} \tag{3.5.20}$$

where  $\gamma_i = \Phi_i + \varphi_i - \mu$ . Also, rearranging and substituting Eq. (3.5.10) into Eq. (3.5.9) we get,

$$\begin{aligned}
\rho_i &= \frac{1}{\Xi_0} \sum_{m_1=0}^1 \sum_{m_2=0}^1 \cdots \sum_{m_M=0}^1 m_i e^{-\beta \sum_{j=1}^M \gamma_j m_j} \\
&= \frac{\sum_{m_i=0}^1 m_i e^{-\beta \sum_{j=1}^M \gamma_j m_j}}{\sum_{m_i=0}^1 e^{-\beta \sum_{j=1}^M \gamma_j m_j}} = \frac{e^{-\beta \gamma_i}}{1 + e^{-\beta \gamma_i}}.
\end{aligned} \tag{3.5.21}$$

The above equation implies:

$$1 - \rho_i = \frac{1}{1 + e^{-\beta \gamma_i}} \quad \text{and} \quad \rho_i = e^{-\beta \gamma_i} (1 - \rho_i). \tag{3.5.22}$$

Hence, we can write Eq. (3.5.20) as  $\Xi_0 = \prod_{i=1}^M \frac{1}{1 - \rho_i}$ . Therefore, the grand free energy becomes:

$$\begin{aligned}
\Omega_0 &= -k_B T \ln \Xi_0 = -k_B T \ln \left( \prod_{i=1}^M \frac{1}{1 - \rho_i} \right) \\
&= -k_B T \sum_{i=1}^M \ln \left( \frac{1}{1 - \rho_i} \right) \\
&= k_B T \sum_{i=1}^M \ln (1 - \rho_i).
\end{aligned} \tag{3.5.23}$$

This can be re-written in more illuminating form:

$$\begin{aligned}\Omega_0 &= k_B T \sum_{i=1}^M (\rho_i + 1 - \rho_i) \ln(1 - \rho_i) \\ &= k_B T \sum_{i=1}^M [\rho_i \ln(1 - \rho_i) + (1 - \rho_i) \ln(1 - \rho_i)].\end{aligned}\quad (3.5.24)$$

Note that Eq. (3.5.22) gives  $\ln(1 - \rho_i) = \beta\gamma_i + \ln \rho_i$ . Hence the above equation can be expressed as

$$\Omega_0 = k_B T \sum_{i=1}^M [\rho_i \ln(\rho_i) + (1 - \rho_i) \ln(1 - \rho_i)] + \sum_{i=1}^M \gamma_i \rho_i. \quad (3.5.25)$$

Recall  $\gamma_i = \Phi_i + \varphi_i - \mu$ , therefore

$$\Omega_0 = k_B T \sum_{i=1}^M [\rho_i \ln(\rho_i) + (1 - \rho_i) \ln(1 - \rho_i)] + \sum_{i=1}^M (\Phi_i + \varphi_i - \mu) \rho_i. \quad (3.5.26)$$

Note that we can write  $\Omega = F - \mu \sum_{i=1}^M \rho_i$ , where,

$$F = k_B T \sum_{i=1}^M [\rho_i \ln(\rho_i) + (1 - \rho_i) \ln(1 - \rho_i)] + \sum_{i=1}^M (\Phi_i + \varphi_i) \rho_i. \quad (3.5.27)$$

In fact, if we had worked in the canonical ensemble and calculated  $Z$  as defined in Eq. (3.5.3), together with the approximation  $E_0 \approx \sum_{i=1}^M \tilde{\gamma}_i m_i$  where  $\tilde{\gamma}_i = \Phi_i + \varphi_i$ , then using Eq. (2.2.22) we would obtain the expression above.

From the definition of  $E_0$  we have,  $\Delta E = E - E_0$  and from Eq. (3.5.1) we have

$$\Delta E = \frac{1}{2} \sum_{i,j} V_{i,j} m_i m_j - \sum_{i=1}^M \varphi_i m_i. \quad (3.5.28)$$

Since  $\rho_i = \langle m_i \rangle$ , we have

$$\langle \Delta E \rangle_0 = \frac{1}{2} \sum_{i,j} V_{i,j} \rho_i \rho_j - \sum_{i=1}^M \varphi_i \rho_i. \quad (3.5.29)$$

From Eqs. (3.5.26) and (3.5.29) we have the upper bound for the grand potential,  $\hat{\Omega}$ ,

$$\begin{aligned}\hat{\Omega} &= \Omega_0 + \langle \Delta E \rangle_0 \\ &= k_B T \sum_{i=1}^M [\rho_i \ln(\rho_i) + (1 - \rho_i) \ln(1 - \rho_i)] + \frac{1}{2} \sum_{i,j} V_{i,j} \rho_i \rho_j + \sum_{i=1}^M (\Phi_i - \mu) \rho_i\end{aligned}\quad (3.5.30)$$

By comparing Eqs. (3.5.26) and (3.5.30) we see that  $\varphi_i = \frac{1}{2} \sum_j V_{i,j} \rho_j$ , where  $\varphi_i$  is the mean field, i.e. the effective field at site  $i$  due to other particles around it.

On comparing the above equation which constitutes a lattice DFT with the continuum DFT (3.2.2), we notice that there are some similarities with the sums over lattice sites being converted into integrals. In chapter 7, we use the lattice DFT to obtain phase diagram for fluids with competing interactions and compare the results with that obtained by Monte Carlo simulation (details of MC simulation can be found in that chapter).

## Chapter 4

# Bulk and Interfacial Phase Behaviour of Simple Fluids

### 4.1 Bulk Phase Behaviour

Phase transitions happen regularly in nature. We are all familiar with the phase transitions of water, namely boiling and freezing. Regions in parameter space where a substance is stable in a particular phase is represented by a phase diagram. In order to create the phase diagram one should know where two different phases coexist. For different phases to coexist in equilibrium, they should be in thermal, mechanical and chemical equilibrium. Consider a system with two phases  $a$  and  $b$ . If these two phases are in coexistence, then the following conditions hold:

$$\text{Thermal equilibrium : } T_a = T_b \quad (4.1.1)$$

$$\text{Mechanical equilibrium : } p_a = p_b \quad (4.1.2)$$

$$\text{Chemical equilibrium : } \mu_a = \mu_b \quad (4.1.3)$$

where  $T_\alpha$ ,  $p_\alpha$  and  $\mu_\alpha$  is the temperature, pressure and chemical potential of the system when it is of phase  $\alpha$ , where  $\alpha = a, b$ .

The region where the phase separation occurs can be calculated using the Helmholtz free energy  $F$ . We define  $f = F/V$  as free energy per volume and the boundary of the unstable region, called

the spinodal, can be calculated as the locus of

$$\frac{\partial^2 f}{\partial \rho^2} = 0. \quad (4.1.4)$$

This defines the locus where the compressibility (2.6.5) diverges. Using  $\rho = N/V$ , the chemical potential (2.2.21) in the fluid is given by

$$\mu = \frac{\partial F}{\partial N} = \frac{\partial f}{\partial \rho} \quad (4.1.5)$$

and the pressure in the fluid is given by

$$p = -\frac{\partial F}{\partial V} = \rho \left( \frac{\partial f}{\partial \rho} \right) - f \quad (4.1.6)$$

$$= \rho \mu - f. \quad (4.1.7)$$

Suppose the phase coexistence that we are interested in is gas-liquid phase coexistence, therefore let  $\rho_l$  and  $\rho_g$  be the densities of the coexisting liquid and gas, respectively. Then, to find the coexistence we need to satisfy the following conditions:

$$\left. \frac{\partial f}{\partial \rho} \right|_{\rho=\rho_l} = \left. \frac{\partial f}{\partial \rho} \right|_{\rho=\rho_g} \quad (4.1.8)$$

$$\left[ \rho \left( \frac{\partial f}{\partial \rho} \right) - f \right]_{\rho=\rho_l} = \left[ \rho \left( \frac{\partial f}{\partial \rho} \right) - f \right]_{\rho=\rho_g}. \quad (4.1.9)$$

For the model fluid that we consider below in chapter 5, we assume that the particles interact via hard-sphere pair potential plus an attractive tail  $v(r)$  that is given by the attractive part of the Lennard-Jones (LJ) potential in Eq. (2.1.2). Therefore, the pair interaction between the fluid particles,  $V(r) = V_{\text{HS}}(r) + v(r)$ , where

$$v(r) = \begin{cases} -4\varepsilon \left(\frac{\sigma}{r}\right)^6 & r \geq \sigma \\ 0 & r < \sigma, \end{cases} \quad (4.1.10)$$

and where  $\sigma$  is the diameter of the particle and  $\varepsilon$  is the attraction strength coefficient. We assume the free energy contribution due to the attraction between the particles is given by the mean-field

approximation given in Eq. (3.4.5). Hence, for a bulk fluid with density  $\rho_b$  we have

$$f_{\text{ex}}^{\text{p}} = \frac{1}{2V} \iint \rho(\mathbf{r})\rho(\mathbf{r}')v(|\mathbf{r} - \mathbf{r}'|) d\mathbf{r} d\mathbf{r}' = \frac{1}{2}\rho_b^2 \int v(\mathbf{r}) d\mathbf{r} = \frac{1}{2}\rho_b^2 \hat{v}(0), \quad (4.1.11)$$

where the integrated interaction strength  $\hat{v}(0)$  is given by

$$\hat{v}(0) = 4\pi \int_0^\infty r^2 v(r) dr = -\frac{16\pi}{3}\varepsilon\sigma^3. \quad (4.1.12)$$

Moreover, for the hard-sphere contribution we use the White-Bear version of the FMT (3.3.39) and this gives

$$f_{\text{ex}}^{\text{HS}} = -n_0 \ln(1 - n_3) + \frac{n_1 n_2}{1 - n_3} + \frac{n_3^3 [n_3 + (1 - n_3)^2 \ln(1 - n_3)]}{36\pi n_3^2 (1 - n_3)^2}, \quad (4.1.13)$$

since the vector weighted densities vanish for a bulk fluid and for the scalar weighted densities we have [23]

$$n_0 = \rho_b, \quad n_1 = \rho_b \frac{\sigma}{2}, \quad n_2 = 4\pi\rho_b \left(\frac{\sigma}{2}\right)^2, \quad n_3 = \frac{4\pi\rho_b}{3} \left(\frac{\sigma}{2}\right)^3. \quad (4.1.14)$$

Hence, the free energy per volume becomes

$$\beta f = \rho_b [\ln(\rho_b) - 1] + f_{\text{ex}}^{\text{HS}} + f_{\text{ex}}^{\text{p}}, \quad (4.1.15)$$

where the first term comes from the ideal gas contribution. Eq. (4.1.15) together with Eqs. (4.1.4), (4.1.8) and (4.1.9) can be used to obtain the gas-liquid coexistence curve (binodal) and the spinodal [c.f. Eq. (4.1.4)], as shown in Fig. 4.1. We see that for  $T < T_c$ , where the critical temperature  $T_c \approx 1.5\varepsilon/k_B$ , there is coexistence between a low density gas phase and a higher density liquid phase. The density difference between these phases increases as  $T$  is decreased.

## 4.2 Fluids at Interfaces

In the presence of an external field such as a wall, the fluid density is no longer uniform. If the attraction between the fluid particles is weaker than the attraction between the wall and the fluid, one can expect to find more fluid particles near the surface than in bulk. If, on approaching bulk gas-liquid phase coexistence (which occurs at  $\mu = \mu_{\text{coex}}$ ) from the gas side, we observe a thick

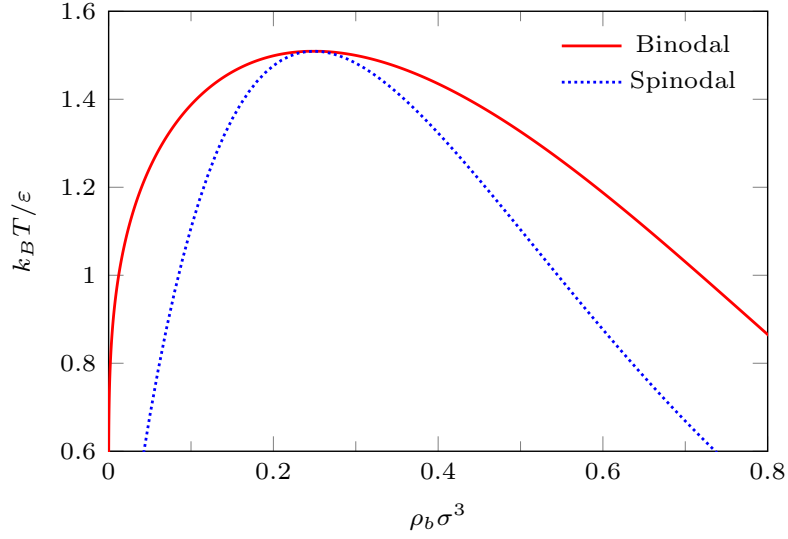


Figure 4.1: Bulk fluid phase diagram in the density versus temperature plane.

(macroscopic) layer of the liquid in contact with the surface. This is referred to as wetting. If on the other hand, fluid particles prefer to be with one another more than near the surface, then the liquid will seek to lower its contact with the surface. This is referred to as partial wetting. If there are no fluid particles near the surface, this is referred to as complete drying.

One can generalise the differential expression for the grand potential in Eq. (2.3.9) to include a contribution from a planar interface

$$d\Omega = -SdT - Nd\mu - pdV + \gamma dA, \quad (4.2.1)$$

where  $A$  is the interfacial area and  $\gamma$  is the *interfacial tension*. This expression applies both to the interface between a fluid and a solid or to the interface between the gas and liquid phases. In the latter case,  $\gamma$  is the gas-liquid interfacial tension  $\gamma_{gl}$ . From Eq. (4.2.1) one can obtain the interfacial tension  $\gamma$  as the derivative of the grand potential:

$$\gamma = \left( \frac{\partial \Omega}{\partial A} \right)_{T, \mu, V}. \quad (4.2.2)$$

Moreover, one can integrate Eq. (4.2.1) to obtain the grand potential [cf. Eq. (2.3.11)]:

$$\Omega = -pV + \gamma A. \quad (4.2.3)$$

Note that for the bulk fluid system, e.g. a fluid with no interface, one has  $\Omega_b = -pV$  and the interfacial tension can be defined as the excess grand potential per unit area:

$$\gamma = \frac{\Omega - \Omega_b}{A} \equiv \frac{\Omega_{ex}}{A}, \quad (4.2.4)$$

where  $\Omega_{ex}$  is the excess grand potential. The differential of the excess grand potential is

$$d\Omega_{ex} = -S_{ex}dT - \Gamma d\mu + \gamma dA = \gamma dA + Ad\gamma, \quad (4.2.5)$$

where  $\Gamma$  is the *Gibbs adsorption*, given by the equation

$$\Gamma = - \left( \frac{\partial \gamma}{\partial \mu} \right)_{T,V}. \quad (4.2.6)$$

Given the fluid density profile at a solid wall with normal along the  $z$ -axis and surface located at  $z = 0$  one can also calculate the adsorption via

$$\Gamma = \int_0^\infty (\rho(z) - \rho_b) dz. \quad (4.2.7)$$

### 4.2.1 Binding Potential

For a system containing a single planar solid surface, with phase  $a$  in bulk and a film of phase  $b$  of thickness  $l$  adsorbed on the wall, the additional contribution to the free energy per area for having a film of finite thickness  $l$  is given by  $\omega(l)$ , known as the binding potential [28, 29, 30, 31]. At bulk coexistence ( $\Delta\mu = 0$ ), the binding potential  $\omega(l) \rightarrow 0$  as  $l \rightarrow \infty$ .  $\Delta\mu = \mu - \mu_{\text{coex}}$  is the difference between the value of the chemical potential and the value at coexistence. Thus,  $\omega(l)$  can be thought of as an effective interaction potential between the two interfaces. Hence, the excess grand potential can be written as

$$\Omega_{ex} = A[\gamma_{sa} + \gamma_{ab} + \omega(l) + \Gamma \Delta\mu], \quad (4.2.8)$$

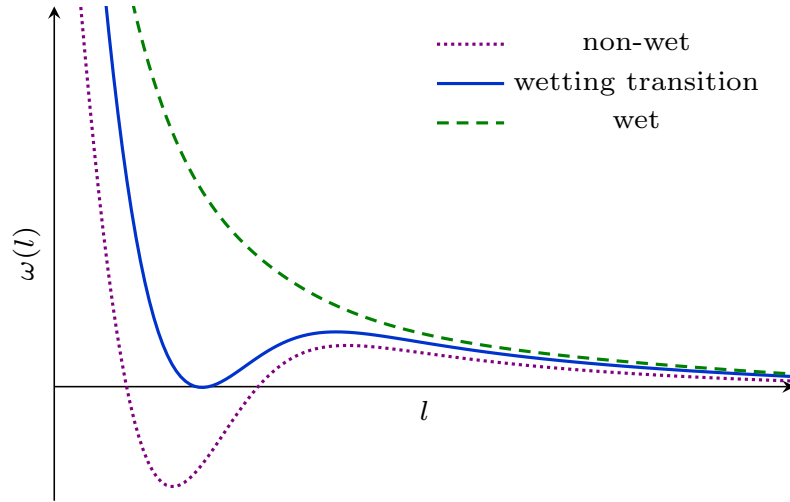


Figure 4.2: A schematic sketch of binding potential for wetting, where  $l$  is the thickness of the film of liquid on the wall. Note that at the (first order) wetting transition there are two global minima. The graph for drying looks similar, but in this case  $l$  is the thickness of the gas layer adsorbed on the wall.

where  $\gamma_{sa}$  and  $\gamma_{ab}$  is the surface-phase  $a$  and phase  $a$ - $b$  interfacial tensions, respectively.

A sketch of the binding potential for wetting is shown Fig. 4.2. Note that for drying, the overall shape and behaviour is similar. For drying (also for wetting) film, the minimum of the binding potential tells us whether the fluid dries (wets) the surface or not. The minimum of the binding potential at  $l \rightarrow \infty$  at coexistence indicates that the surface is dry (wet). If the minimum occurs at a finite value  $l = l_0$ , then the surface is partially dry (wet), i.e. the fluid forms a drying (wetting) film of thickness  $l_0$  on the surface.

For a fluid of particles of diameter  $\sigma$  interacting via the LJ potential (2.1.2) with attraction coefficient  $\varepsilon$  in contact with a planar solid surface that is composed of particles with diameter  $\sigma_{wf}$  and attraction  $\varepsilon_{wf}$ , the binding potential (using the sharp-kink approximation) can be shown to be [32]:

$$\omega(l) = \frac{b(T)}{l^2} + \frac{c(T)}{l^3} + \mathcal{O}\left(\frac{1}{l^4}\right), \quad (4.2.9)$$

where the temperature dependent Hamaker constant  $b(T)$  and coefficient  $c(T)$  for a drying film are

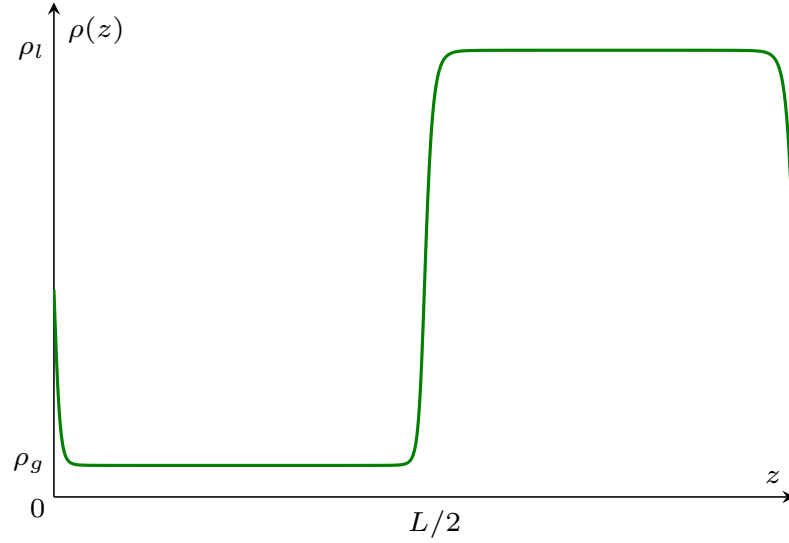


Figure 4.3: Density profile showing gas-liquid coexistence calculated using the DFT on a domain of length  $L$ . The density profile shows two gas-liquid interfaces due to periodic boundary conditions.  $\rho_g$  and  $\rho_l$  are the coexisting gas and liquid densities, respectively.

given by

$$b(T) = \frac{\pi}{3}(\rho_g \varepsilon \sigma^3 - \rho_w \varepsilon_{wf} \sigma_{wf}^3) \Delta \rho \sigma^3 \quad (4.2.10)$$

$$c(T) = \frac{2\pi}{3} dw \rho_w \varepsilon_{wf} \Delta \rho \sigma_{wf}^6 \quad (4.2.11)$$

and where  $\Delta \rho = \rho_l - \rho_g$  is the difference in the coexisting densities and the excluded length  $dw = (\sigma + \sigma_{wf})/2$ . Since all the quantities in the expression for  $c(T)$  are positive we have  $c(T) > 0$  for all temperatures. However,  $b(T)$  changes sign from negative to positive on increasing the temperature. This is because, as the temperature increases, the gas density  $\rho_g$  increases. Note that complete drying occurs when  $w(l) > 0$  (when the minimum is at  $l \rightarrow \infty$ ), i.e. when  $b(T) > 0$  which is satisfied when  $\rho_g \varepsilon \sigma^3 > \rho_w \varepsilon_{wf} \sigma_{wf}^3$ . Hence, one finds that  $\varepsilon_{wf}^c = \varepsilon \rho_g / \rho_w$  is the critical value of the wall-fluid attraction strength at which critical drying occurs.

### 4.2.2 Young's Equation

Using Eq. (4.2.4) and the DFT discussed in chapter 3 one can calculate the interfacial tension. It is important to note that the interfacial tension can only be calculated at coexistence, since it is at

coexistence that there is a gas-liquid interface. We assume that the fluid density only varies in the  $z$ -direction and is invariant in the  $x$  and  $y$ -directions. Also assuming the system is of finite length, with periodic boundary conditions in the  $z$ -direction, we seek to find an equilibrium density profile with initial guess for the profile

$$\rho(z) = \begin{cases} \rho_g & z < L/2 \\ \rho_l & \text{otherwise} \end{cases} \quad (4.2.12)$$

The resulting equilibrium density profile is shown in Fig. 4.3. Due to the periodic boundary conditions we get two gas-liquid interfaces. Therefore, we need to adjust Eq. (4.2.4) such that

$$\gamma_{gl} = \frac{\Omega - \Omega_b}{2A}, \quad (4.2.13)$$

where  $\Omega$  is the grand potential corresponding to the density profile displayed in Fig. 4.3. Note that in such an effective 1D system, we have unit interfacial area.

A similar approach can be used to find the surface-gas and surface-liquid interfacial tensions. One must find the equilibrium density profile with the boundary condition  $\rho(z \rightarrow \infty) = \rho_b$ , where  $\rho_b$  is either the gas or the liquid bulk density. The grand potential is found from the equilibrium density profile at the wall and then using Eq. (4.2.4) we can find the corresponding interfacial tensions. In this case, we do not need to divide by 2 [like we need to find  $\gamma_{gl}$  using Eq. (4.2.13)], since there is only one interface.

A relationship connecting the interfacial tensions and the macroscopic contact angle  $\theta$  that a droplet makes with a surface was derived in 1805 by Young [33] and is known as Young's equation:

$$\cos \theta = \frac{\gamma_{sg} - \gamma_{sl}}{\gamma_{gl}}. \quad (4.2.14)$$

Thus, having calculated the three interfacial tensions, one can calculate  $\theta$ . The contact angle enables to easily identify the wetting and drying scenarios.  $\theta$  takes values from  $0^\circ$  to  $180^\circ$  with  $\theta = 0^\circ$  corresponding to when the interface is completely wet and  $\theta = 180^\circ$  to when the interface is completely dry [cf. Fig. 4.4]. A system with contact angle  $\theta \geq 90^\circ$  is called a solvophobic system since the solvent is repelled by the surface and if  $\theta < 90^\circ$  then the system is called a solvophilic

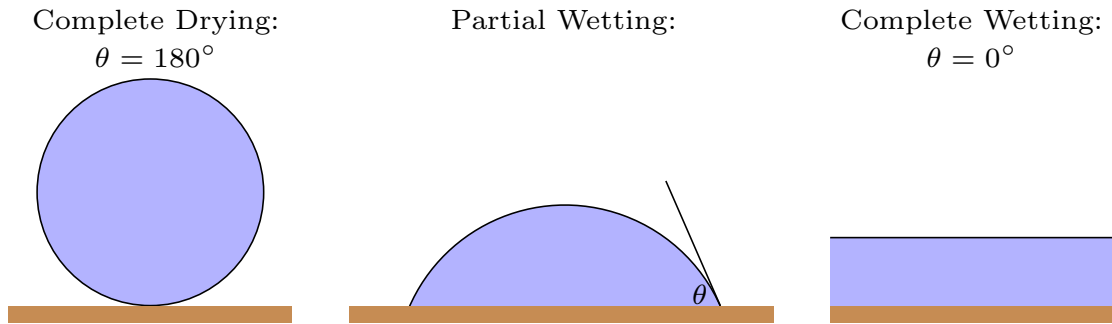


Figure 4.4: A schematic view of different shapes a liquid (blue) forms on a surface (brown). The surface is said to be completely dry when the contact angle is  $\theta = 180^\circ$  (left) and completely wet when  $\theta = 0^\circ$  (right). The centre diagram shows a partial wetting case when the liquid does not completely wet or dry the surface in which case the contact angle is  $0^\circ < \theta < 180^\circ$ .

system. We return to this in the following chapter.

### 4.2.3 Order of Phase Transition

Phase transitions (including surface phase transitions) can occur either continuously or discontinuously, with a ‘jump’ in some physical quantity (e.g. the adsorption in surface phase transitions), often referred to as the order parameter for the transition. This behaviour is characterised by the ‘order’ of the transition, which considers a thermodynamical potential (in our case, the surface free energy) and its derivative. It is called a first order phase transition if the first derivative of the thermodynamical potential is discontinuous and second order if the first derivative is continuous and the second derivative is discontinuous [34]. The second order transition is also called a critical transition.

When the contact angle  $\theta \rightarrow 0^\circ$ , it is called a wetting transition and when  $\theta \rightarrow 180^\circ$ , it is called drying transition. Note that the binding potential shown in Fig. 4.2 is typical of a first order wetting transition. Experimentally, most wetting transitions are first order and it is rare to find experimental studies of wetting that are critical; only few such cases exist. Nevertheless, they have been observed in simulation and theoretical studies that look closely into critical wetting. The theoretical studies often make a mean field approximation based on Landau theory and DFT. When it comes to simulations, the studies become complicated due to the finite size effects [35, 36]. A general review on wetting transitions can be found in Ref. [37].

Similar to critical wetting, the experimental studies of critical drying are sparse due to challenges in fabricating the surface that have large contact angle. Nevertheless, the emergence of superhydrophobic surfaces [38], which can be used as self cleaning surfaces or in chemical separation process, will potentially lead to more experimental studies. Nevertheless, it is well established in theoretical studies that critical drying occurs for any liquid that exhibits liquid-gas coexistence adsorbed at a planar hard wall [39, 40]. With simulation, it was only recently that there were evidence for critical drying and this was for SPC/E water by using MC simulations [41]. For more about drying transitions see Refs. [42, 43].

#### 4.2.4 Solvation Force and Kelvin's Equation

In chapter 5 we deal with fluids between two planar solid surfaces in which case one can generalise Eq. (4.2.1) for the differential of the total grand potential by including an additional term  $f_s AdL$  such that [18]

$$d\Omega = -SdT - Nd\mu - pdV + 2\gamma dA - f_s AdL, \quad (4.2.15)$$

where  $L$  is the distance between the two surfaces (of area  $A$ ) and  $f_s$  is referred to as the *solvation force* (excess pressure in the fluid due to confinement). Since  $dV = AdL$ , the solvation force is given by:

$$f_s = -\frac{1}{A} \left( \frac{\partial \Omega}{\partial L} \right) - p. \quad (4.2.16)$$

One can note that solvation force vanishes in the limit  $L \rightarrow \infty$ . The solvent mediated potential (or solvation potential) between the two surfaces is defined as

$$W(L) = \frac{1}{A} [\Omega_{ex}(L) - \Omega_{ex}(L \rightarrow \infty)], \quad (4.2.17)$$

such that the solvation force  $f_s = -\partial W / \partial L$ . This is the solvent-mediated force between the surfaces.

Furthermore, one can determine the value of the distance between the surfaces  $L$  when capillary evaporation occurs by comparing the grand potentials. Capillary evaporation is when there is a sudden change of the density between two surfaces from liquid-like to gas-like. The grand potential

when the gas phase is present between the surfaces is given by

$$\Omega_g = -p_g AL + 2A\gamma_{sg}, \quad (4.2.18)$$

where  $p_g$  is the pressure of the gas and  $\gamma_{sg}$  is the surface-gas interfacial tension. Similarly, the grand potential for when the liquid phase is between the surfaces is given by

$$\Omega_l = -p_l AL + 2A\gamma_{sl}, \quad (4.2.19)$$

where  $p_l$  is the pressure of the liquid and  $\gamma_{sl}$  is the surface-liquid interfacial tension. Capillary evaporation occurs when  $\Omega_l = \Omega_g$ . Using Young's equation (4.2.14) together with Eqs. (4.2.18) and (4.2.19) we obtain

$$(p_l - p_g)L = -2\gamma_{gl} \cos \theta. \quad (4.2.20)$$

One can approximate  $p_l - p_g$  for a system not too far away from coexistence by Taylor expanding  $p$  around the value at  $\mu = \mu_{\text{coex}}$ . We have

$$p = p_{\text{coex}} + \left. \frac{\partial p}{\partial \mu} \right|_{\text{coex}} \Delta\mu + \dots, \quad (4.2.21)$$

where  $\Delta\mu = \mu - \mu_{\text{coex}}$ . For fixed temperature, Eq. (2.3.9) becomes

$$\begin{aligned} 0 &= -d\Omega - Nd\mu - pdV \\ &= -d(-pV) - Nd\mu - pdV = Vdp - Nd\mu. \end{aligned} \quad (4.2.22)$$

From this we obtain the Gibbs-Duhem relation  $(\partial p / \partial \mu)_T = N/V = \rho$ . Hence, Eq. (4.2.21) for the pressure of the liquid or gas at a state point not too far away from coexistence becomes

$$p_l = p_{\text{coex}} + \rho_l \Delta\mu, \quad (4.2.23)$$

$$p_g = p_{\text{coex}} + \rho_g \Delta\mu. \quad (4.2.24)$$

Therefore, Eq. (4.2.20) gives the separation between the two walls when capillary evaporation occurs

as

$$L = \frac{-2\gamma_{gl} \cos \theta}{\Delta\rho\Delta\mu}, \quad (4.2.25)$$

since  $p_l - p_g = (\rho_l - \rho_g)\Delta\mu = \Delta\rho\Delta\mu$ . This equation is known as Kelvin's equation [29].

## Chapter 5

# Solvent fluctuations around solvophobic, solvophilic and patchy nanostructures and the accompanying solvent mediated interactions

*Using classical density functional theory (DFT) we calculate the density profile  $\rho(\mathbf{r})$  and local compressibility  $\chi(\mathbf{r})$  of a simple liquid solvent in which a pair of blocks with (microscopic) rectangular cross-section are immersed. We consider blocks that are solvophobic, solvophilic and also ones that have both solvophobic and solvophilic patches. Large values of  $\chi(\mathbf{r})$  correspond to regions in space where the liquid density is fluctuating most strongly. We seek to elucidate how enhanced density fluctuations correlate with the solvent mediated force between the blocks, as the distance between the blocks and the chemical potential of the liquid reservoir vary. For sufficiently solvophobic blocks, at small block separations and small deviations from bulk gas-liquid coexistence, we observe a strongly attractive (near constant) force, stemming from capillary evaporation to form a low density gas-like intrusion between the blocks. The accompanying  $\chi(\mathbf{r})$  exhibits structure which reflects the incipient gas-liquid interfaces that develop. We argue that our model system provides a means to understanding the basic physics of solvent mediated interactions between nanostructures, and between objects such as proteins in water, that possess hydrophobic and hydrophilic patches.*

## 5.1 Introduction

Understanding the properties of water near hydrophobic surfaces continues to attract attention across several different disciplines [44, 45], ranging from the design of self-cleaning materials [46, 47] to biological self-assembly and protein interactions [48]. Likewise, understanding the (water mediated) interactions between hydrophobic and hydrophilic entities is important in many areas of physical chemistry and chemical physics. In a recent article, Kanduč *et al.* [49] survey the field and describe informatively how the behaviour of soft-matter at the nano-scale depends crucially on surface properties and outline the key role played by water mediated interactions in many technological and biological processes. These include colloid science, where altering the surface chemistry can change enormously the effective interactions, e.g. those preventing aggregation, and biological matter where effective membrane-membrane interactions can be important in biological processes.

In attempting to ascertain the nature of effective interactions, it is crucial to know whether a certain substrate, or entity, is hydrophilic or hydrophobic. For a macroscopic (planar) substrate the degree of hydrophobicity is measured by Young's contact angle  $\theta$ . A strongly hydrophobic surface, such as a self-assembled monolayer (SAM), paraffin or hydrocarbon, can have  $\theta > 120^\circ$ , while a strongly hydrophilic surface can often correspond to complete wetting, i.e.  $\theta = 0^\circ$ , meaning a water drop spreads across the whole surface. However, in the majority of systems encountered in the physical chemistry of colloids, in nanoscience and in situations pertinent to biological systems, the entities immersed in water do not have a macroscopic surface area. Thus it is important to ask to what extent ideas borrowed from a macroscopic (capillarity) description, which simply balance bulk (volume) and surface (area) contributions to the total grand potential but which make specific predictions for the effective interaction between two immersed macroscopic hydrophobic entities, remain valid at the nanoscale. For example, Huang *et al.* [50] consider the phenomenon of capillary evaporation of a simple point charge (SPC) water model between two hydrophobic oblate (ellipsoidal) plates. These authors discuss the validity of the macroscopic formula at which evaporation occurs and the form of the solvent mediated force between the plates. More recently, Jabes *et al.* [51] investigate the solvent-induced interactions for SPC/E water between curved hydrophobes; they consider the influence of different types of confining geometry and conclude that macroscopic thermodynamic (capillarity) arguments work surprisingly well, even at length scales corresponding

to a few molecular (water) diameters. The survey article Ref. [49] emphasises the usefulness of capillarity ideas for analysing water mediated forces between two entities that have different adsorbing strengths.

Such observations raise the general physics question as to how well should one expect capillarity arguments to work for nanoscale entities immersed in an arbitrary solvent. Are these observations specific to water? This seems most unlikely. In this chapter we argue that insight into fundamental aspects of solvent mediated interactions, particularly those pertaining to solvophobes, are best addressed by considering the effective, solvent mediated interactions between nanostructures immersed in a simple Lennard-Jones (LJ) liquid. By focusing on a model liquid with much simpler intermolecular forces than those in water, one can investigate more easily and more systematically the underlying physics, e.g. the length scales relevant for phenomena such as capillary evaporation and how these determine the effective interactions.

A second, closely related, aspect of our present study is concerned with the strength and range of density fluctuations in water close to hydrophobic substrates. It is now accepted that for water near a macroscopic strongly hydrophobic substrate the local number density of the water is reduced below that in bulk for the first one or two adsorbed molecular layers. Accompanying this reduction in local density there is growing evidence for a substantial increase in fluctuations in the local number density; these increase for increasing water contact angle. An illuminating review [52] surveys the field up to 2011, describing earlier work on density fluctuations, from the groups of Garde, Hummer, and Chandler. The basic idea of Garde and co-workers is that a large value of some, appropriately defined, local compressibility reflects the strength of density fluctuations in the neighbourhood of the substrate and should provide a quantitative measure of the degree of hydrophobicity of the hydrophobic entity [52]. The idea is appealing. However, even for a macroscopic planar substrate, there are problems in deciding upon the appropriate measure. Once again, this issue is not specific to water. If strong fluctuations occur at hydrophobic surfaces one should also expect these to occur at solvophobic surfaces, for similar values of chemical potential deviation from bulk coexistence. In other words, pronounced fluctuations cannot be specific to water near hydrophobic substrates. This argument was outlined recently [53, 41].

Evans and Stewart [53] discuss the merits of various different quantities that measure surface fluctuations. They argue that the compressibility  $\chi(\mathbf{r})$ , defined as the derivative of the equilibrium

density,  $\rho(\mathbf{r})$ , with respect to the chemical potential  $\mu$  at fixed temperature  $T$ :

$$\chi(\mathbf{r}) \equiv \left( \frac{\partial \rho(\mathbf{r})}{\partial \mu} \right)_T \quad (5.1.1)$$

provides the most natural and useful measure for quantifying the local fluctuations in an inhomogeneous liquid. This quantity was introduced much earlier [30, 31, 54], in studies of wetting/drying and confined fluids and is, of course, calculated in the grand canonical ensemble. The usual isothermal compressibility [9]  $\kappa_T = \chi_b / \rho_b^2$ , where  $\chi_b \equiv (\partial \rho_b / \partial \mu)_T$  is the bulk value of the compressibility; recall that  $\chi_b \rightarrow \infty$  on approaching the bulk fluid critical point. Note that  $\chi(\mathbf{r})$  can be expressed [41] as the correlator

$$\chi(\mathbf{r}) = \beta \langle N \hat{\rho}(\mathbf{r}) - \langle N \rangle \langle \hat{\rho}(\mathbf{r}) \rangle \rangle \quad (5.1.2)$$

where  $\beta = (k_B T)^{-1}$ ,  $\hat{\rho}(\mathbf{r})$  is the particle density operator,  $N = \int \hat{\rho}(\mathbf{r}) d\mathbf{r}$  is the number of particles and  $\langle \dots \rangle$  denotes a grand canonical average. Thus  $\langle \hat{\rho}(\mathbf{r}) \rangle = \rho(\mathbf{r})$  and  $\langle N \rangle$  is the average number of particles. Clearly  $\chi(\mathbf{r})$  correlates the local number density at  $\mathbf{r}$  with the total number of particles in the system. The measures of  $\chi(\mathbf{r})$  introduced by other authors [55, 56] are designed for molecular dynamics computations which are performed in the canonical ensemble rather than in the grand canonical ensemble. The latter is more appropriate for adsorption studies.

Using DFT, Evans and Stewart [53] calculated  $\chi(z)$  defined by Eq. (5.1.1) for LJ liquids near planar substrates, with the wall at  $z = 0$ . They investigated substrates which ranged from neutral ( $\theta \approx 90^\circ$ ) to very solvophobic ( $\theta \approx 170^\circ$ ) and found that this quantity is enhanced over bulk, exhibiting a peak for  $z$  within one or two atomic diameters of the substrate. The height of the peak increased significantly as  $\theta$  increased and the substrate became more solvophobic. In subsequent investigations, using Grand Canonical Monte Carlo (GCMC) for SPC/E water [41] and GCMC plus DFT for a LJ liquid [42] at model solvophobic substrates, it was observed the the maximum in  $\chi(z)$  increases rapidly as the strength of the wall-fluid attraction is reduced, thereby increasing  $\theta$  towards  $180^\circ$ , i.e. towards complete drying. For different choices of wall-fluid potentials the drying transition is continuous (critical) and the thickness of the intruding gas-like layer as well as the maximum in  $\chi(z)$  diverge as  $\cos \theta \rightarrow -1$  [41, 42]. These observations pertain to the liquid at coexistence, where  $\mu = \mu_{\text{coex}}^+$ .

Much is made in the literature concerning the depleted local density and accompanying enhanced surface fluctuations of water at hydrophobic surfaces as arising from the particular properties of water, namely the hydrogen-bonding and the open tetrahedrally coordinated liquid structure, which is said to be disrupted by the presence of large enough hydrophobic objects. However, following from Refs. [53, 41] we show here that much of this phenomenology is also observed when a simple LJ like solvent that is near to bulk gas-liquid phase coexistence is in contact with solvophobic objects. The particular entities we consider are i) planar surfaces of infinite area and ii) long blocks with a finite rectangular-cross-section. For these objects to be solvophobic, we treat them as being composed of particles to which the solvent particles are attracted weakly, compared to the strength of the attraction between solvent particles themselves. The contact angle of the solvent liquid at the planar solvophobic substrate considered here is  $\theta \approx 144^\circ$ . We also consider the behaviour at solvophilic objects, for which the contact angle at the corresponding planar substrate is  $\theta \approx 44^\circ$ .

The simple LJ like solvent we consider consists of particles with a hard-sphere pair interaction plus an additional attractive tail potential that decays  $\sim r^{-6}$ , where  $r$  is the distance between the solvent particles. We use classical density functional theory (DFT) [19, 18, 9], treating the hard core interactions using the White-Bear version of fundamental measure theory (FMT) [27, 23], together with a mean-field treatment of the attractive interactions, to calculate the solvent density profile  $\rho(\mathbf{r})$  and local compressibility  $\chi(\mathbf{r})$ . An advantage of using DFT is that having calculated  $\rho(\mathbf{r})$ , one then has access to all thermodynamic quantities including the various interfacial tensions. Calculating the grand potential as a function of the distance between the blocks yields the effective solvent mediated potential; minus the derivative of this quantity is the solvent mediated force between the blocks.

When both blocks are solvophobic *and* the liquid is at a state point near to bulk gas-liquid phase coexistence, we find that the solvent mediated force between these is strongly attractive at short distances due to the formation of a gas-like intrusion. Proximity to coexistence can be quantified by the difference  $\Delta\mu = \mu - \mu_{\text{coex}}$ , where  $\mu_{\text{coex}}$  is the value at bulk gas-liquid coexistence. For a slit pore consisting of two parallel surfaces of infinite extent that are sufficiently solvophobic,  $\theta > 90^\circ$ , a first order transition, namely capillary evaporation, occurs as  $\Delta\mu \rightarrow 0$ , corresponding to the stabilisation of the incipient gas phase in the slit of finite width [57, 58, 59]. The formation of the gas-like intrusion between the blocks that we consider here occurs at smaller  $\Delta\mu$ . This is

not a genuine first order surface phase transition, owing to the finite size of the blocks. However, this phenomenon is intimately related to the capillary evaporation that occurs between parallel planar surfaces with both dimensions infinite. It turns into the genuine capillary evaporation phase transition as the height of our blocks is increased to  $\infty$ . Note that some authors in the water community, e.g. Refs. [45], [50] and Remsing *et al.* [60], refer to this phenomenon as “dewetting”, but given that this term is also used to describe a film of liquid on a single planar surface breaking up to form droplets, a network pattern or other structures [61, 62, 63, 64, 65], we prefer to use the more accurate term, capillary evaporation. The important matter of nomenclature was emphasised in a Faraday Discussion on hydrophobic and structured surfaces; see Refs. [66, 67].

We also present results for the local compressibility  $\chi(\mathbf{r})$  in the vicinity of the blocks. Maxima in  $\chi(\mathbf{r})$  correspond to points in space where the density fluctuations are the greatest. We find that the formation of the gas-like intrusion between the hydrophobic blocks is associated with a local value of  $\chi(\mathbf{r})$  that is much greater than the bulk value. However, we find that the solvent density fluctuations are not necessarily at points in space that one might initially expect. For example, when there is a gas-like intrusion, the value of  $\chi(\mathbf{r})$  is larger at the entrance to the gap between the blocks, rather than in the centre of the gap.

We are not the first to use DFT to study liquids near corners and between surfaces. Bryk *et al.* [68] calculated the solvent mediated (depletion) potential between a hard-sphere colloidal particle, immersed in a solvent of smaller hard-spheres, and planar substrates or geometrically structured substrates, including a right-angled wedge. They found that in the wedge geometry there is a strong attraction of the colloid to inner corners, but there is a free energy barrier repelling the colloid from an outer corner (edge) of a wedge. Hopkins *et al.* [69] studied the solvent mediated interaction between a spherical (soft-core) particle, several times larger than the (soft-core) solvent particles, and a planar interface. They showed that when the binary solvent surrounding the large particle (colloid) is near to liquid-liquid phase coexistence, thick (wetting) films rich in the minority solvent species can form around it and on the interface. This has a profound effect on the solvent mediated potential, making it strongly attractive. A similar effect, due to proximity to liquid-liquid phase separation, was found for the solvent mediated potential between pairs of spherical colloidal particles [69, 70, 71]. Analogous effects arising from proximity to gas-liquid phase coexistence, i.e. when  $\Delta\mu$  is small were found in a very recent study [72]. Such investigations, studying the influence

of proximity to bulk phase coexistence on the solvent mediated potential between pairs of spherical particles, provide insight regarding what one might expect in the cases studied here, namely pairs of hydrophobic, hydrophilic and patchy blocks.

The strong attractive forces between solvophobic objects, decreased local density and enhanced fluctuations close to the substrate, all occur when the liquid is near to bulk gas-liquid phase coexistence, i.e. when  $\Delta\mu$  is small. Note that liquid water at ambient conditions is near to saturation. For water at ambient conditions  $\beta\Delta\mu \sim 10^{-3}$ . This dimensionless quantity provides a natural measure of over-saturation, indicating where our results might be appropriate to water and to other solvents. The other key ingredient in determining the physics of effective interactions is the liquid-gas surface tension  $\gamma_{lg}$ , which is especially large for water. More precisely, it is the ratio  $\gamma_{lg}/(\Delta\mu\rho_l)$ , where  $\rho_l$  is the density of the coexisting liquid, that sets the length scale for the capillary evaporation of any liquid; see Eq. (5.3.9) below. The length scale in water is, of course, especially important. The influential article by Lum *et al.* [73] underestimates this. Subsequent articles [74] and the informative piece [75] by Cerdeiriña *et al.* point to the fact that for water under ambient conditions the characteristic length for capillary evaporation is  $L_c \sim 1.5 \mu\text{m}$ . The latter authors analyse why this length scale is so long and conclude this is due primarily to the large value of  $\gamma_{lg}$  of water at room temperature.

The chapter is arranged as follows: In Sec. 5.2 we define the model solvent and the DFT used to describe it. Results for the fluid at a single planar substrate (wall) and between two identical walls are discussed in Sec. 5.3. Then, in Sec. 5.4, we build a model for the two rectangular blocks and analyse the density profiles and local compressibility around the pair of blocks, comparing with results for the planar substrates. We examine the effect of changing the distance between the two blocks; this enables us to determine effective solvent mediated interactions between the blocks. These interactions differ enormously between an identical pair of solvophobic and a pair of solvophilic blocks. We also consider the case of i) a solvophobic and a solvophilic block and ii) blocks made from up to three patches that can be either solvophobic or solvophilic. The density and local compressibility profiles exhibit a rich structure in these cases and the resulting effective interactions exhibit considerable variety. We conclude in Sec. 5.5 with a discussion of our results.

## 5.2 Model Solvent

DFT [19, 18, 9] introduces the thermodynamic grand potential functional  $\Omega[\rho]$  as a functional of the fluid one-body density profile,  $\rho(\mathbf{r})$ . The profile which minimises  $\Omega[\rho]$  is the equilibrium profile and for this profile the functional is equal to the grand potential for the system. For a fluid of particles interacting via a hard-sphere pair potential plus an additional attractive pair potential  $v(r)$ , the grand potential functional can be approximated as follows [19, 18, 9]:

$$\Omega[\rho] = \mathcal{F}_{\text{id}}[\rho] + \mathcal{F}_{\text{ex}}^{\text{HS}}[\rho] + \frac{1}{2} \iint \rho(\mathbf{r})\rho(\mathbf{r}')v(|\mathbf{r} - \mathbf{r}'|) \, \mathbf{d}\mathbf{r} \, \mathbf{d}\mathbf{r}' + \int \rho(\mathbf{r})(\phi(\mathbf{r}) - \mu) \, \mathbf{d}\mathbf{r}, \quad (5.2.1)$$

where  $\mathcal{F}_{\text{id}} = k_B T \int \rho(\mathbf{r})(\ln[\Lambda^3 \rho(\mathbf{r})] - 1) \, \mathbf{d}\mathbf{r}$  is the ideal-gas contribution to the free energy, with Boltzmann's constant  $k_B$ , temperature  $T$  and thermal de Broglie wavelength  $\Lambda$ .  $\mathcal{F}_{\text{ex}}^{\text{HS}} = \int \Phi(\{n_\alpha\}) \, \mathbf{d}\mathbf{r}$  is the hard-sphere contribution to the excess free energy, which we treat using the White-Bear version of FMT [27, 23], i.e. the free energy density  $\Phi$  is a function of the weighted densities  $\{n_\alpha\}$ .  $\phi(\mathbf{r})$  is the external potential and  $\mu$  is the chemical potential. The attractive interaction between the particles is assumed to be given by a simple interaction potential, incorporating London dispersion forces,

$$v(r) = \begin{cases} -4\varepsilon \left(\frac{\sigma}{r}\right)^6 & r \geq \sigma \\ 0 & r < \sigma, \end{cases} \quad (5.2.2)$$

where  $\sigma$  is the hard-sphere diameter and  $\varepsilon > 0$  is the attraction strength.

In Fig. 5.1 we display the bulk fluid phase diagram, showing the gas-liquid coexistence curve (binodal) and spinodal calculated from Eq. (5.2.1). Bulk gas-liquid phase separation occurs when  $T < T_c$ , where the critical temperature  $T_c = 1.509\varepsilon/k_B$  and the critical density  $\rho_c \sigma^3 = 0.249$ . The results presented in the remainder of the chapter are calculated along the isotherm with  $T = 0.8 T_c$ . We approach bulk gas-liquid coexistence from the liquid side, varying the chemical potential to determine the bulk liquid density. At coexistence, the chemical potential  $\mu = \mu_{\text{coex}}$  takes the same value for both liquid and gas phases. We define  $\Delta\mu = \mu - \mu_{\text{coex}}$ , which gives a measure of how far a given bulk state is from coexistence. In Fig. 5.2 we display the bulk liquid density as a function of  $\beta\Delta\mu$ , for  $T = 0.8 T_c$ .

In addition to calculating density profiles and thermodynamic properties of the system, we also

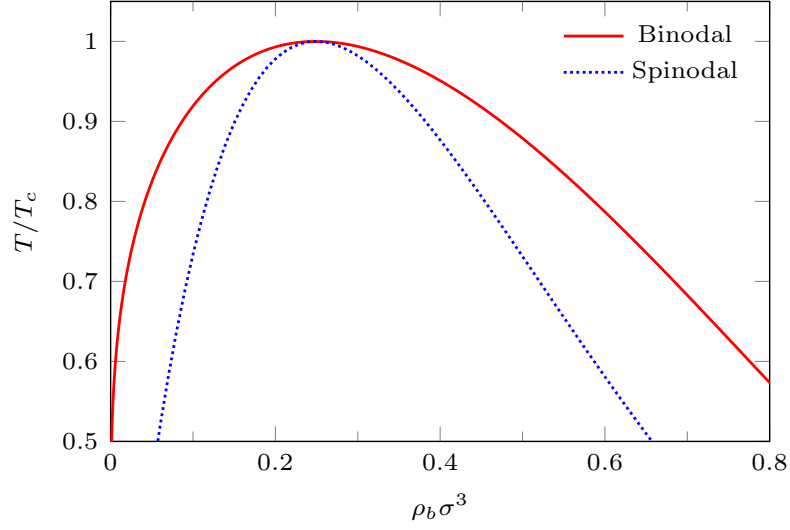


Figure 5.1: Bulk fluid phase diagram in the density versus temperature plane.  $T_c$  is the critical temperature.

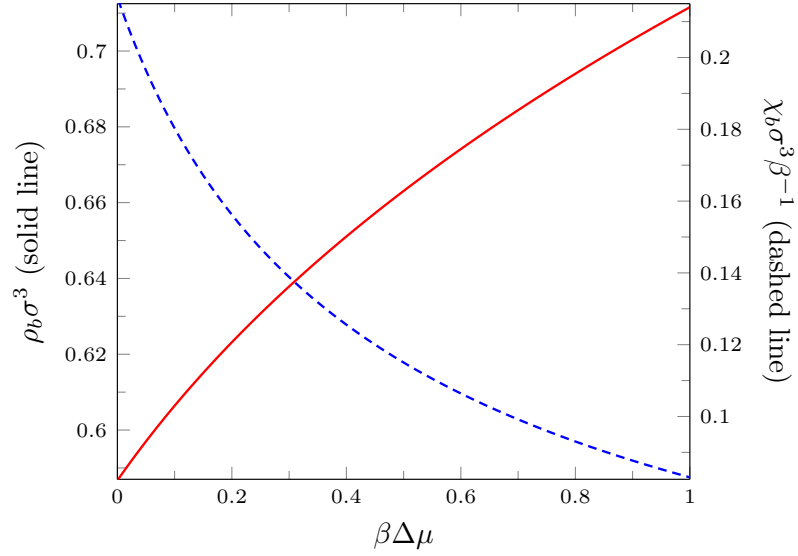


Figure 5.2: The bulk liquid density (solid line) and bulk compressibility (dashed line) as a function of  $\Delta\mu = (\mu - \mu_{\text{coex}})$ , for fixed temperature  $T = 0.8T_c$ .

calculate the local (position dependent) compressibility in Eq. (5.1.1). In order to calculate this quantity, we use the finite difference approximation:

$$\chi(\mathbf{r}) = \frac{\rho(\mathbf{r}; \mu + \delta\mu) - \rho(\mathbf{r}; \mu - \delta\mu)}{2\delta\mu}, \quad (5.2.3)$$

with  $\beta\delta\mu = 10^{-4}$ . The bulk value of the compressibility  $\chi_b \equiv (\partial\rho_b/\partial\mu)_T$ , as a function of the chemical potential, is also shown in Fig. 5.2, for  $T = 0.8T_c$ . We see that as the chemical potential is increased away from the value at coexistence, the bulk density increases (solid line) and  $\chi_b$  decreases (dashed line).

### 5.3 Liquid at Planar Walls

Before presenting results for the liquid solvent around various different rectangular blocks, we describe its behaviour in the presence of a single planar wall and confined between two parallel planar walls. This is a prerequisite for understanding the behaviour around the blocks.

#### 5.3.1 Single Hard Wall with an Attractive Tail

Initially, we treat the wall as being made of a different species of particle having a uniform density distribution and interacting with the fluid via a pair potential of the same form as the potential between the fluid particles, i.e. a hard-sphere potential together with the attractive pair potential

$$v_{wf}^h(r) = \begin{cases} -4\varepsilon_{wf}^h \left(\frac{\sigma}{r}\right)^6 & r \geq \sigma \\ 0 & r < \sigma. \end{cases} \quad (5.3.1)$$

This is the same as the potential in Eq. (5.2.2), but with  $\varepsilon$  replaced by the wall-fluid attraction strength parameter  $\varepsilon_{wf}^h > 0$ . Thus, the external one-body potential due to a substrate made of particles having uniform density  $\rho_w$ , occupying the half space  $z < 0$  (i.e. the wall surface is located at  $z = 0$ ), is

$$\phi(\mathbf{r}) \equiv \phi(z) = \rho_w \int_{z < 0} d\mathbf{r}' v_{wf}^h(|\mathbf{r} - \mathbf{r}'|), \quad (5.3.2)$$

for  $z \geq \sigma/2$  and  $\phi(z) = \infty$  for  $z < \sigma/2$ . From this we obtain

$$\phi(z) = \begin{cases} -\frac{2}{3}\varepsilon_{wf}^h \rho_w \sigma^3 \pi \left(\frac{\sigma}{z}\right)^3 & z \geq \sigma/2 \\ \infty & z < \sigma/2, \end{cases} \quad (5.3.3)$$

where  $z$  is the perpendicular distance from the surface of the wall. Henceforth, for simplicity, we set  $\rho_w \sigma^3 = 1$ .

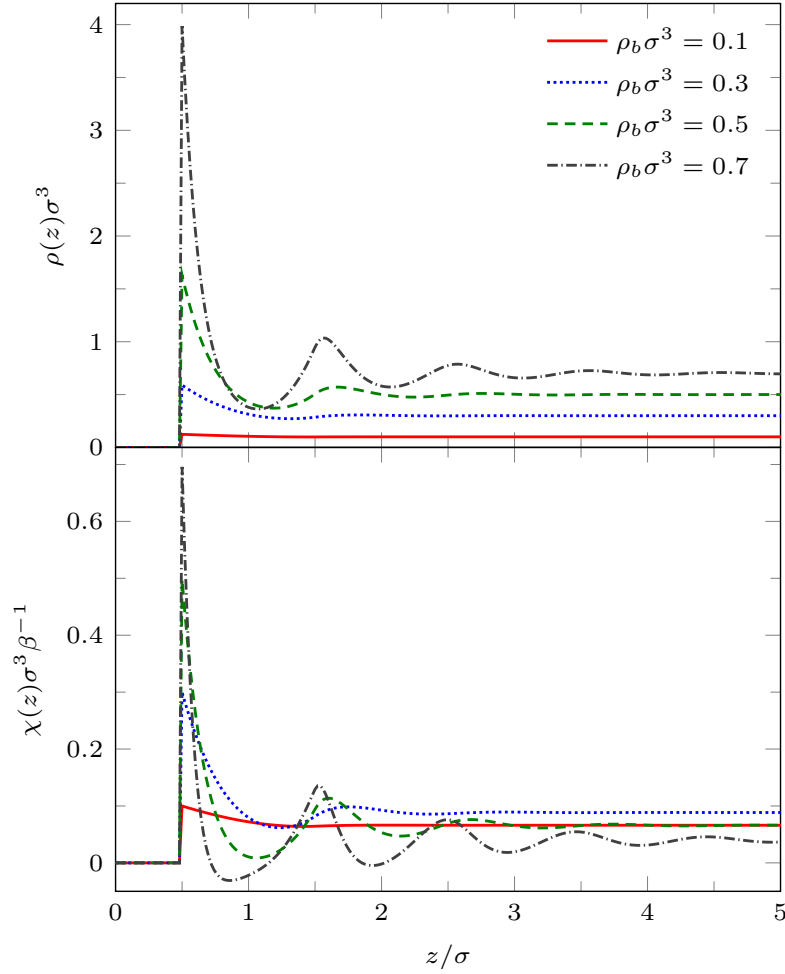


Figure 5.3: Density profiles  $\rho(z)$  and local compressibility  $\chi(z)$  for a fluid of hard spheres against a hard planar wall ( $\varepsilon_{wf}^h = 0$ ) for different bulk densities.

In Fig. 5.3 we display the fluid density profiles and the local compressibility for the hard-sphere fluid ( $\varepsilon = 0$ , equivalent to  $T \rightarrow \infty$ ) against a planar hard wall ( $\varepsilon_{wf}^h = 0$ ). This is useful for comparing with the later results, in order to assess the influence of the attractive interactions. We see that for low values of the bulk fluid density  $\rho_b$ , the density profile has little structure, as does  $\chi(z)$ . Note that  $\chi(z)$  has large contributions due to packing and/or due to being near to criticality. Increasing the bulk fluid density, we observe oscillations developing near to the wall arising from packing. The local compressibility  $\chi(z)$  also develops significant oscillations near the wall. For higher values of  $\rho_b$  we see that the contact value  $\chi(\frac{\sigma}{2}^+)$  is significantly larger than the bulk value. We also note that it is possible for the local compressibility  $\chi(z)$  to be *negative*, while of course the bulk value  $\chi_b$  must be positive. This is because for larger values of  $\rho_b$ , the local density values at

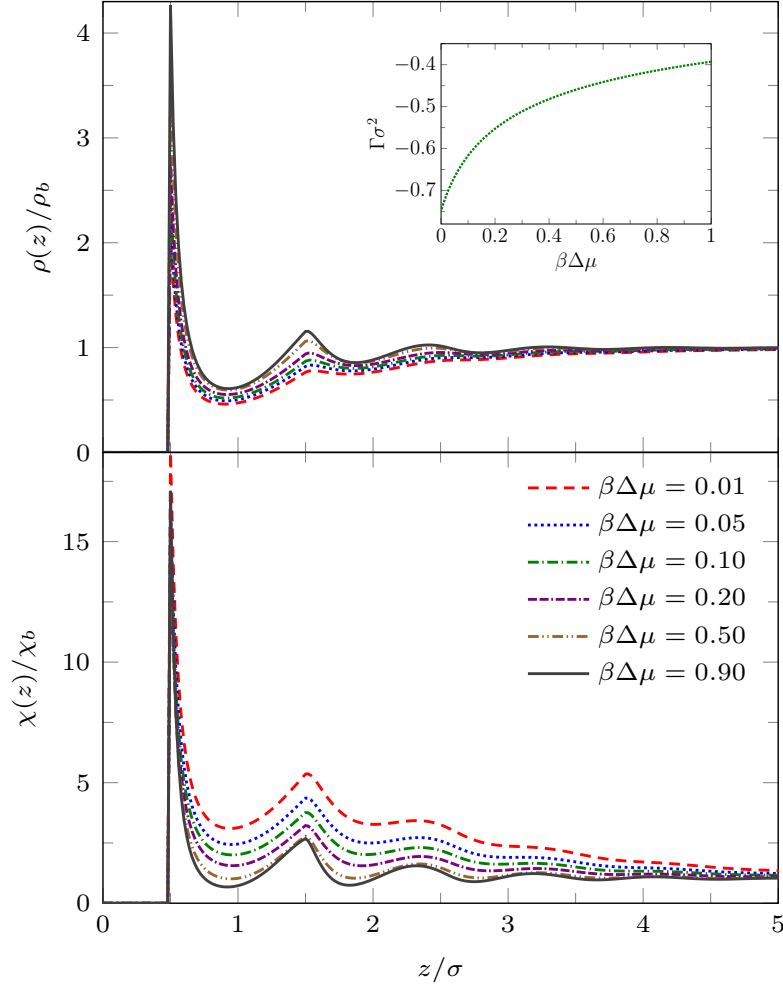


Figure 5.4: Scaled density profile and local compressibility for the liquid with temperature  $T = 0.8 T_c$  at a single planar wall, Eq. (5.3.3), with  $\beta\varepsilon_{wf}^h = 0.13$ . The corresponding bulk density  $\rho_b$  and compressibility  $\chi_b$  can be obtained from Fig. 5.2. Note that the contact angle for this choice of parameters is  $\theta \approx 144^\circ$ . The inset in the upper panel shows the adsorption as a function of  $\beta\Delta\mu$ .

the minima of the oscillations are much smaller than in bulk, reflecting the fact that layering of the fluid at the wall becomes more pronounced.

We turn now to the case  $\varepsilon > 0$  and consider the temperature  $T = 0.8 T_c$ , where bulk gas-liquid phase separation occurs. We set the wall attraction to be  $\beta\varepsilon_{wf}^h = 0.13$ , which is rather weak, corresponding to a solvophobic substrate with contact angle  $\approx 144^\circ$  at this temperature. The contact angle  $\theta$  is calculated using Young's equation

$$\gamma_{wg} = \gamma_{wl} + \gamma_{gl} \cos \theta, \quad (5.3.4)$$

where  $\gamma_{wg}$ ,  $\gamma_{wl}$  and  $\gamma_{gl}$  are the wall-gas, wall-liquid and gas-liquid surface tensions, respectively. These interfacial tensions are each calculated separately via DFT in the usual manner (see e.g. Ref. [54] and references therein). The contact angle of  $\approx 144^\circ$  is chosen for solvophobic surfaces and  $\approx 43.7^\circ$  for solvophilic surfaces such that they are not at the extremes but still have a fair separation between them. Moreover, they are the range of the contact angles found in biological systems.

Fig. 5.4 shows liquid density profiles and the local compressibility (both divided by their respective bulk values) on the isotherm  $T = 0.8T_c$ . At this temperature the bulk density of the liquid at coexistence with the gas is  $\rho_b\sigma^3 \approx 0.587$ . For larger values of  $\beta\Delta\mu$ , away from coexistence, the density profiles exhibit oscillations at the wall, similar to the density profile for pure hard-spheres against the hard wall (Fig. 5.3). As coexistence is approached, the oscillations in the density profiles are slightly eroded, although for this value of  $\beta\varepsilon_{wf}^h = 0.13$ , the changes in the density profile are not particularly striking. This can also be seen from the inset in Fig. 5.4 which displays the adsorption

$$\Gamma = \int_0^\infty dz(\rho(z) - \rho_b). \quad (5.3.5)$$

Note that  $\Gamma$  is negative and remains finite as  $\beta\Delta\mu \rightarrow 0$ . However, as can be seen from the lower panel of Fig. 5.4, where we display the corresponding local compressibility profiles  $\chi(z)$ , there is a significant increase in the local compressibility in layers adjacent to wall as coexistence is approached,  $\beta\Delta\mu \rightarrow 0^+$ . We note also that the compressibility has oscillations whose maxima match those in the density profiles.

### 5.3.2 Single Soft Lennard-Jones Wall

The wall, Eq. (5.3.3), considered in the previous subsection leads to the fluid density profile and local compressibility having a very sharp (and discontinuous) first peak at  $z = \sigma/2$ , particular to this wall potential. The contact density  $\rho(\sigma/2)$  is related to the bulk pressure via a sum rule (see e.g. Eq. (68a) in Ref. [76]), which is satisfied by the present DFT. For general wall-potentials there is no *explicit* formula for  $\rho(\sigma/2)$ . However, it is clear from the relation emerging from the sum rule that this quantity must be very large for a potential such as (5.3.3) [76]. Real molecular fluids interact with substrates via continuous (softer) potentials. Thus, we now consider a planar wall

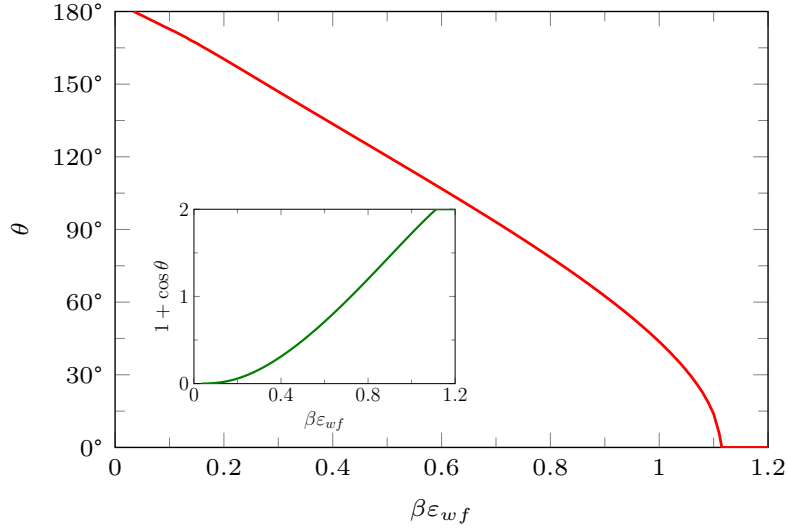


Figure 5.5: Contact angle  $\theta$  as a function of the wall attraction strength  $\beta\varepsilon_{wf}$  in Eq. (5.3.7) for  $T = 0.8T_c$ . The inset plots  $(1 + \cos\theta)$  versus  $\beta\varepsilon_{wf}$ . Note that  $(1 + \cos\theta) \rightarrow 0$  tangentially as  $\beta\varepsilon_{wf} \rightarrow 0.0344$ . By contrast,  $(1 + \cos\theta) \rightarrow 2$  linearly as  $\beta\varepsilon_{wf} \rightarrow 1.11$ . Thus, drying is critical and wetting is first order for this choice of wall.

composed of particles that interact with the fluid particles via the LJ pair potential

$$v_{wf}(r) = 4\varepsilon_{wf} \left[ \left( \frac{\sigma}{r} \right)^{12} - \left( \frac{\sigma}{r} \right)^6 \right], \quad (5.3.6)$$

where  $\varepsilon_{wf} > 0$  is the coefficient determining the strength of wall attraction. Thus, using Eq. (5.3.2) with  $v_{wf}^h$  replaced by  $v_{wf}$ , for  $z > 0$  and  $\phi(z) = \infty$  for  $z \leq 0$ , we have

$$\phi(z) = \begin{cases} 4\varepsilon_{wf}\rho_w\sigma^3\pi \left( \frac{\sigma^9}{45z^9} - \frac{\sigma^3}{6z^3} \right) & z > 0 \\ \infty & z \leq 0, \end{cases} \quad (5.3.7)$$

where  $z$  is the perpendicular distance from the wall. The contact angle calculated using Eq. (5.3.4) for the liquid against this soft wall for  $T = 0.8T_c$  is shown in Fig. 5.5. When we set the wall attraction to be  $\beta\varepsilon_{wf} = 0.3$ , then the contact angle is  $\theta \approx 144^\circ$ , which is the same contact angle that the fluid has against the hard wall with an attractive tail potential (5.3.3), with  $\beta\varepsilon_{wf}^h = 0.13$  – as treated in Fig. 5.3. Note that in Fig. 5.5 the drying transition, where  $\theta \rightarrow 180^\circ$ , occurs at  $\beta\varepsilon_{wf} = 0.0344$  and is continuous (critical). The numerical result from DFT for this value agrees precisely with the analytical prediction from the binding potential treatment for the same model potentials treated

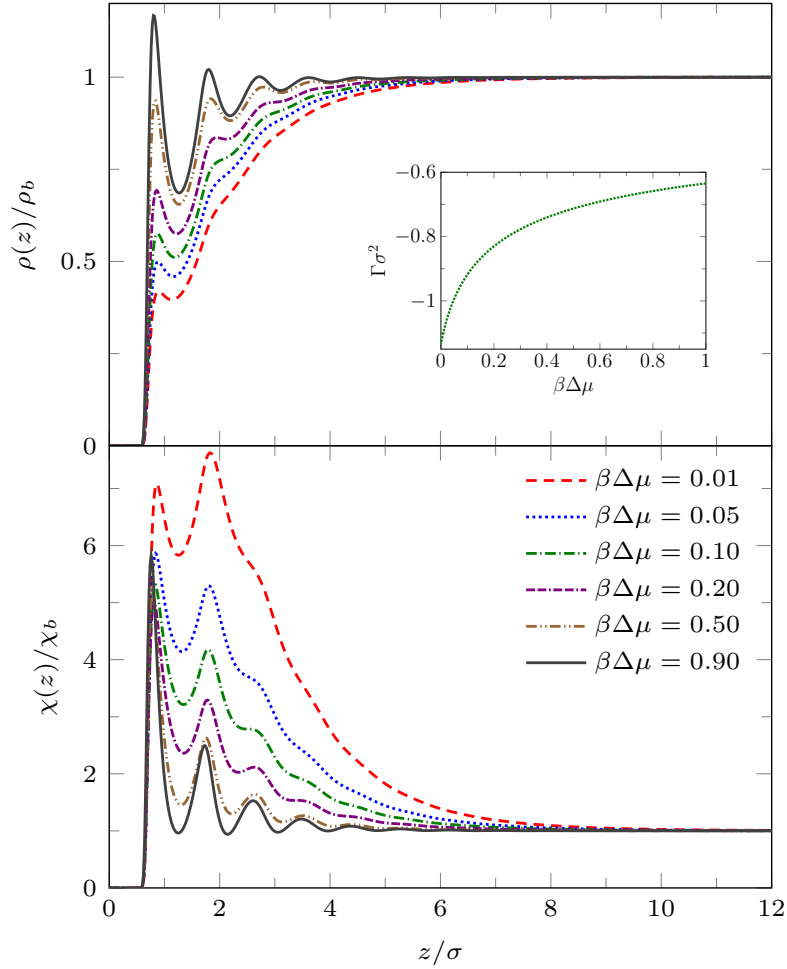


Figure 5.6: Scaled liquid density profile and local compressibility at a single planar wall, Eq. (5.3.7), with  $T = 0.8T_c$  and  $\beta\varepsilon_{wf} = 0.3$ . The bulk densities corresponding to the chemical potentials  $\beta\Delta\mu$  in the key can be read from Fig. 5.2. Note that the contact angle for this choice of parameters is  $\theta \approx 144^\circ$ . The inset in the upper panel shows the adsorption as a function of  $\beta\Delta\mu$ .

in the sharp-kink approximation [32]. The latter predicts a continuous drying transition when  $\beta\varepsilon_{wf}(\rho_w\sigma^3) = \beta\varepsilon(\rho_g\sigma^3)$ , where  $\rho_g$  is the density of the coexisting gas at the given temperature. What is striking about this result is that it also applies for the wall potential in Eq. (5.3.3), i.e. critical drying occurs at the same value  $\beta\varepsilon_{wf}^h = \beta\varepsilon_{wf} = 0.0344$ . This is a consequence of both potentials having the same asymptotic decay as  $z \rightarrow \infty$ . However, for the potential in Eq. (5.3.3) wetting,  $\theta = 0^\circ$ , occurs at a much smaller value of  $\beta\varepsilon_{wf}^h$ . Thus, the overall behaviour of  $(1 + \cos\theta)$  vs wall strength is sensitive to the precise form of the wall potential.

Fig. 5.6 shows liquid density profiles and the local compressibility (both divided by their respec-

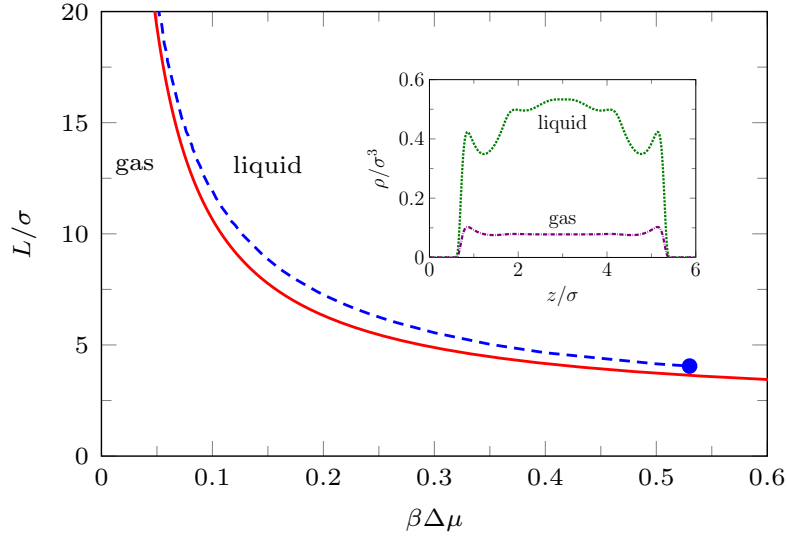


Figure 5.7: The figure shows the capillary evaporation line calculated via DFT (dashed) and that from the Kelvin equation (5.3.9) (solid), for two parallel planar walls with  $\beta\varepsilon_{wf} = 0.3$  and  $T = 0.8 T_c$ . The critical point of the capillary evaporation is marked with a circle. For values of  $L$  below the critical value, there is no capillary evaporation. The inset shows the coexisting gas and liquid density profiles when  $L = 6\sigma$ , i.e.  $\beta\Delta\mu \approx 0.266$ .

tive bulk values) on the isotherm  $T = 0.8 T_c$ . For large values of  $\beta\Delta\mu$  the density profiles exhibit oscillations at the wall similar to the density profiles for the walls in Figs. 5.3 and 5.4. However, as coexistence is approached the degree to which the oscillations in the density profiles near the wall are eroded is greater than for the case of the wall (5.3.3) and a region of depleted density appears at the wall. Note that for this value of  $\varepsilon_{wf}$ , the low density film close to the wall remains finite in thickness right up to coexistence,  $\beta\Delta\mu \rightarrow 0$ , since the wall-liquid interface is only partially dry:  $\theta < 180^\circ$ . This can also be seen from the inset which shows the adsorption (5.3.5). Although  $\Gamma$  is somewhat larger in magnitude than for the wall potential (5.3.3), displayed in the inset to Fig. 5.4, it remains finite at coexistence. In the lower panel of Fig. 5.6 we display the corresponding local compressibility profiles  $\chi(z)$  in the vicinity of this solvophobic surface. We observe that in the first few adsorbed layers, the local compressibility increases significantly i.e. the range over which  $\chi(z)/\chi_b$  is significantly greater than unity increases as  $\beta\Delta\mu \rightarrow 0$ . Moreover the maximum near  $z/\sigma = 2$ , corresponding to the second particle layer, grows rapidly as  $\beta\Delta\mu$  decreases.

### 5.3.3 Two Planar Walls

We now consider briefly a pair of planar walls, where the distance between the walls is  $L$ . The external potential is

$$\phi_{2w}(z) = \phi(z) + \phi(L - z), \quad (5.3.8)$$

where  $\phi(z)$  is given by the soft wall Eq. (5.3.7). Capillary evaporation from this planar slit can occur as  $\beta\Delta\mu \rightarrow 0$ , whereby the liquid between the two solvophobic planar walls evaporates as coexistence is approached. The value of  $L$  at which this occurs can be estimated from the Kelvin equation [29, 57]:

$$L^* \approx \frac{-2\gamma_{lg} \cos \theta}{\Delta\mu(\rho_l - \rho_g)} \quad (5.3.9)$$

where  $L^* \equiv L - 2\sigma$  is defined as roughly the distance between maxima of the density profile, corresponding to the first adsorbed layer at each wall.  $L^*$  is the effective distance between the walls.  $\gamma_{lg}$  is the gas-liquid interfacial tension,  $\theta$  is the single planar wall contact angle, and  $\rho_g$  and  $\rho_l$  are the coexisting gas and liquid densities, respectively. Eq. (5.3.9) is appropriate to a partial drying situation [29].

Fig. 5.7 shows the capillary evaporation phase transition line, comparing the prediction from the Kelvin equation (5.3.9) with that calculated from DFT. This is the line in the  $(\Delta\mu, L)$  plane where the gas-filled slit and liquid-filled slit are at thermodynamic coexistence, i.e. these states have the same grand potential, temperature, and chemical potential. The inset in Fig. 5.7 shows the density profiles of coexisting gas and liquid states for  $L = 6\sigma$ . As we expect, the Kelvin equation is accurate for large  $L$ , but is less reliable for small  $L$ . Nevertheless for values down to  $L \approx 4\sigma$  and  $\beta\Delta\mu = 0.53$ , where the critical point occurs in DFT, the Kelvin equation prediction remains fairly good. This may come as a surprise to some readers, given that the equation is based on macroscopic thermodynamics. Note that Eq. (5.3.9) does not account for a capillary critical point [29, 57]. We have also investigated the solvent mediated potential between two planar walls, i.e. the excess grand potential arising from confinement. The derivative of this quantity with respect to  $L$  jumps at capillary evaporation. We return to this later.

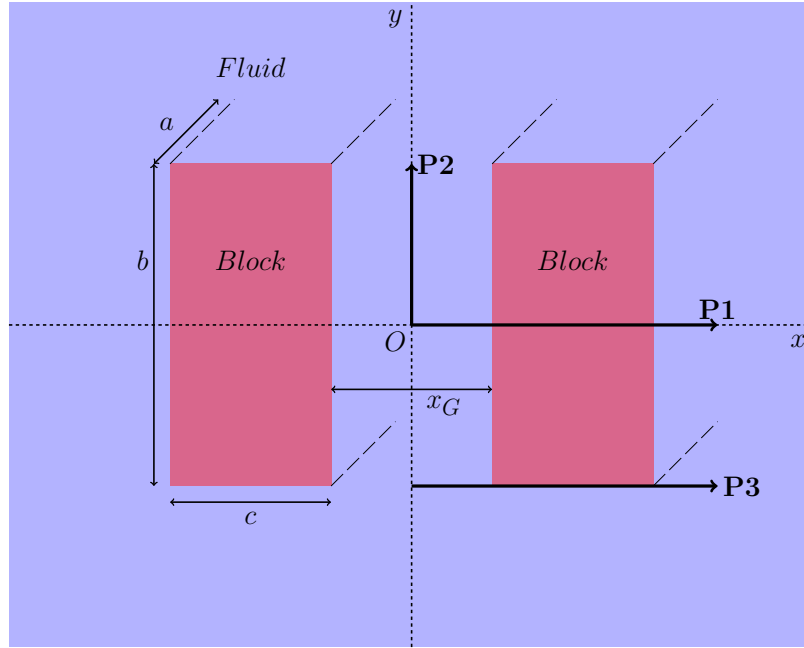


Figure 5.8: An illustration of two rectangular cross-section solid blocks immersed in the liquid. The cross sectional area of each block is  $b \times c$  and the length of the blocks is  $a$ . We assume  $a \rightarrow \infty$ . In the case sketched here, the blocks are made of a uniform density of particles of the same diameter  $\sigma$  as the liquid particles, interacting with the liquid particles via the potential in Eq. (5.3.6). “P1”, “P2” and “P3” denote three different paths along which we display density profiles and the local compressibility in Figs. 5.9 to 5.13, below.

## 5.4 Two Rectangular Blocks

In this section we describe the properties of the liquid around two rectangular cross-section beams of length  $a$  – the two “blocks” illustrated in Fig. 5.8. We assume that the blocks are long, i.e. we take the limit  $a \rightarrow \infty$ . The distance between the closest faces of the blocks is  $x_G$  and we set the size of the cross-section of the two blocks to be  $b \times c$ , where  $b = 8\sigma$  and  $c = 3\sigma$ . We locate the origin of our Cartesian coordinate system to be midway between the two blocks.

The external potential due to the two blocks is defined in a manner analogous to that used above for the planar wall potential [cf. Eq. (5.3.2)]; i.e. the potential due to the two blocks is

$$\phi(\mathbf{r}) = \rho_w \int_{\mathcal{D}} d\mathbf{r}' v_{wf}(|\mathbf{r} - \mathbf{r}'|), \quad (5.4.1)$$

where  $\mathcal{D}$  is the region of space occupied by each of the blocks. The parameter  $\varepsilon_{wf}$  characterises the strength of the attraction between the blocks and the fluid. When  $\varepsilon_{wf}$  is small, the blocks are

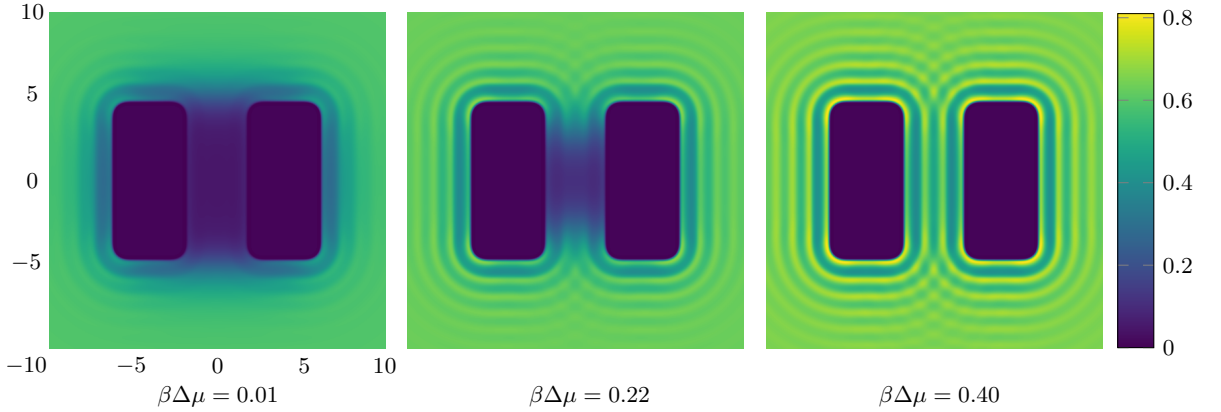


Figure 5.9: Density profile  $\sigma^3\rho(x, y)$  around the pair of solvophobic blocks separated a distance  $x_G = 5\sigma$  apart, for three values of the chemical potential. The temperature  $T = 0.8T_c$  and wall attraction strength  $\beta\varepsilon_{wf} = 0.3$ .

solvophobic, but for larger values of  $\varepsilon_{wf}$  they are solvophilic. Later we consider blocks having some sections that are solvophobic and others that are solvophilic: these are the so called “patchy” blocks. Note that the region  $\mathcal{D}$  is where the fluid is completely excluded, with  $\phi(\mathbf{r}) = \infty$  and is made of two volumes with cross sectional area  $b \times c = 8\sigma \times 3\sigma$ . However, the effective exclusion cross-sectional area of each block is  $\approx b^* \times c^* = 10\sigma \times 5\sigma$ , which includes an exclusion zone of width  $\sigma$  around each of the blocks. Note that the external potential around blocks was calculated by numerically integrating Eq. (5.4.1).

## 5.4.1 Two Solvophobic Blocks

### 5.4.1.1 Blocks at fixed separation $x_G$

The results we present first are for a pair of blocks with soft solvophobic surfaces with  $\beta\varepsilon_{wf} = 0.3$ , at the temperature  $T = 0.8T_c$ . Recall that for the single soft planar wall this value of  $\varepsilon_{wf}$  corresponds to a contact angle  $\theta \approx 144^\circ$  and that for the pair of planar walls the capillary evaporation critical point is at  $\beta\Delta\mu = \beta\Delta\mu_{cc} = 0.53$  – see Fig. 5.7. In Figs. 5.9 and 5.10 we display density profiles and the local compressibility  $\chi(\mathbf{r})$ , for various  $\beta\Delta\mu$  and fixed  $x_G = 5\sigma$ .

The density profiles in Fig. 5.9 show that as coexistence is approached, i.e. as  $\beta\Delta\mu \rightarrow 0$ , the density in the space between the pair of blocks becomes very small, i.e. gas-like. This is somewhat analogous to the capillary evaporation observed between two infinite planar walls – see Fig. 5.7. For larger values of  $\beta\Delta\mu$ , away from the value where bulk gas-liquid coexistence occurs, we see

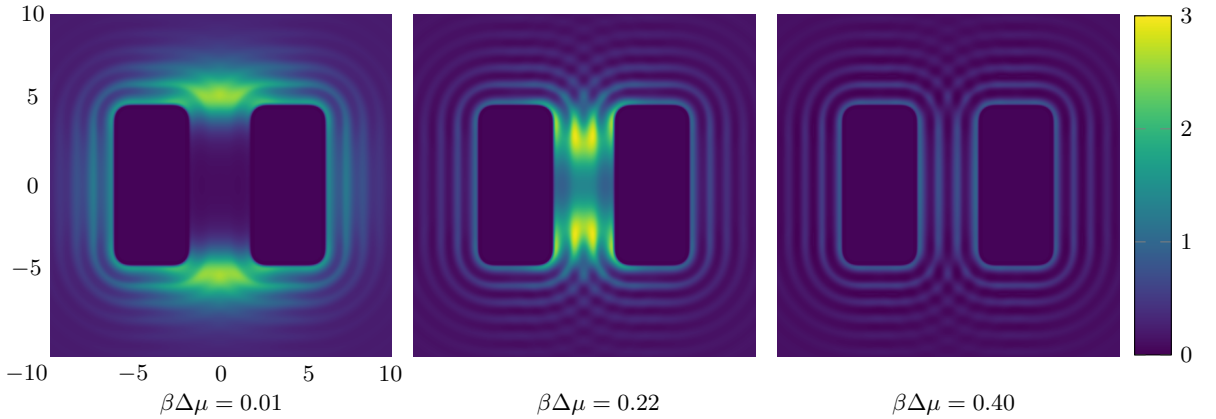


Figure 5.10: The local compressibility  $k_B T \sigma^3 \chi(x, y)$  around the pair of solvophobic blocks, for three states approaching bulk coexistence. The corresponding density profiles are displayed in Fig. 5.9.

oscillations in the density profile arising from the packing of the liquid particles around the blocks. We also note that the density is higher near the corners of the blocks.

The local compressibility  $\chi(\mathbf{r})$  provides a measure of the strength of the local fluctuations within the fluid and so large values of this quantity reveals regions in space where the local density fluctuations are greatest. In Fig. 5.10, we see that for  $\beta\Delta\mu = 0.4$ , well away from bulk coexistence, the local compressibility is largest around the surface of the two blocks, decreasing in an oscillatory manner as the distance from the blocks increases. When the chemical potential deviation is smaller,  $\beta\Delta\mu = 0.22$ , the local compressibility in the vicinity of the outside of the blocks is similar to the case for the larger value of  $\beta\Delta\mu = 0.4$ . However, in the region between the two blocks, we see that the local compressibility is significantly larger, indicating strong fluctuations in this region. For  $\beta\Delta\mu = 0.22$ , we see from Fig. 5.9 that the average density in the gap between the blocks is intermediate between the bulk gas and liquid coexisting densities and so we expect that typical microstates of the system include both gas-like and liquid-like average densities in the gap. The fluctuations of the system between these two typical states are what lead to the high values of the local compressibility.

Approaching even closer to the bulk coexistence point leads to the gas being stabilised in the gap between the blocks – see the density profiles for  $\beta\Delta\mu = 0.01$  in Fig. 5.9. For this value of  $\beta\Delta\mu$  we see from Fig. 5.10 that the region where the local compressibility is largest is not in the gap between the blocks, but is instead at the entrance to this region, where there is an ‘interface’

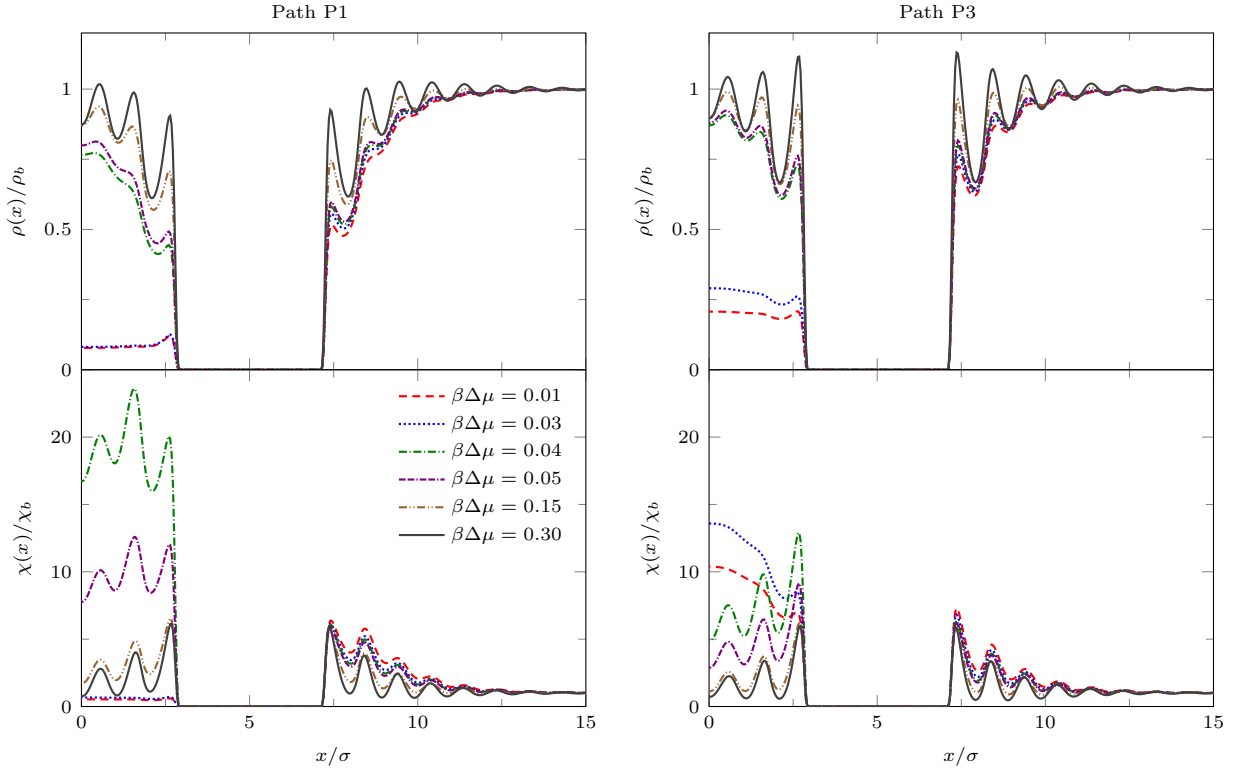


Figure 5.11: Left: density profiles  $\rho(x) \equiv \rho(x, 0)$  (top) and local compressibility  $\chi(x) \equiv \chi(x, 0)$  (bottom) of the fluid along path P1 for various values of the chemical potential and for  $T = 0.8 T_c$ ,  $\beta\varepsilon_{wf} = 0.3$  and fixed distance  $x_G = 7\sigma$  between the blocks. Right: the corresponding functions  $\rho(x) \equiv \rho(x, \pm b/2)$  and  $\chi(x) \equiv \chi(x, \pm b/2)$  on path P3. Note that  $\rho(\mathbf{r}), \chi(\mathbf{r}) \equiv 0$  within the block.

between the bulk liquid and the gas-like intrusion between the blocks. It is the fluctuations in this interface that lead to the maxima in the local compressibility  $\chi(x, y)$ .

We now present results for  $x_G = 7\sigma$ , i.e. with the gap between the blocks being slightly larger. In order to display in more detail the properties of the density profiles and local compressibility around the pair of blocks, we plot these along the three different paths P1, P2 and P3, illustrated in Fig. 5.8. The density and compressibility profiles are, of course, symmetrical around the mid-line through the gap between the blocks, so we display profiles around the right hand block only. From Fig. 5.8 we see that paths P1 and P2 are along the lines of symmetry and path P3 is along the horizontal side of the block.

In Fig. 5.11, we display results along paths P1 and P3. On both paths, both the density and the local compressibility are, of course, zero within the block. Focussing first along the portion of path P1 not in the gap between the blocks, we see that the profiles for varying  $\beta\Delta\mu$  are very similar to

those displayed in Fig. 5.6 for the planar LJ wall: as  $\beta\Delta\mu$  is decreased, the density in the vicinity of the wall decreases and the maxima in  $\chi(\mathbf{r})$  near the wall increase. Comparing with the density profiles along the parallel path P3, along the horizontal size of the blocks, we see that away from the gap between the blocks the local density is slightly higher than along path P1 (this is the influence of the corner), but both the density and compressibility follow the same trend as along path P1.

Moving on to examine the behaviour in the gap between the blocks, in Fig. 5.11 we see that on decreasing  $\beta\Delta\mu$ , along path P1 the density decreases and at  $\beta\Delta\mu \lesssim 0.04$  there is a discontinuous change in the density profile. The density profiles for  $\beta\Delta\mu = 0.03$  and  $0.01$  are almost identical and correspond to a dilute ‘gas’ state. The strong fluctuations connected to the onset of this transition result in very large values of  $\chi(x, 0)$  for  $\beta\Delta\mu = 0.05$  and  $0.04$ .  $\chi(x, 0)$  exhibits a discontinuous change in the gap between the blocks at the value of  $\beta\Delta\mu$  where the density profile jumps. Moreover, along the portion of path P3 along the end of the gap between the blocks, we also observe a large jump in the density profile as coexistence is approached. Along path P3 the local compressibility also jumps. Unlike on path P1, where in the gap  $\chi(x, 0)$  takes small gas-like values for  $\beta\Delta\mu = 0.03$  and  $0.01$ , on path P3  $\chi(0, \pm b/2)/\chi_b$  is very large for these values of  $\beta\Delta\mu$ , reflecting the occurrence of gas-liquid interfacial fluctuations. All of this is reminiscent of the capillary evaporation observed for two planar solvophobic walls. However, the transition occurs at a smaller value of  $\beta\Delta\mu$  due to the finite dimensions of the blocks. Specifically, the transition occurs at  $\beta\Delta\mu \lesssim 0.04$ , whereas for the planar slit with  $L = 7\sigma$  evaporation occurs at  $\beta\Delta\mu = 0.21$ ; see Fig. 5.7.

In Fig. 5.12 we display density profiles and the local compressibility along path P2 (see Fig. 5.8), which starts from the origin (the mid point between the blocks) and goes along the positive  $y$ -axis. For small  $\beta\Delta\mu$ , i.e.  $\beta\Delta\mu = 0.03$  and  $0.01$ , we see that the density is gas-like in the gap between the blocks, increasing to the bulk liquid value outside the gap,  $y \gtrsim 8\sigma$ . The density profile changes discontinuously at  $\beta\Delta\mu \lesssim 0.04$  and for larger values, the density is liquid-like throughout path P2. For smaller values of the chemical potential,  $\beta\Delta\mu \lesssim 0.04$ , there is a local maximum in the local compressibility along this path and the location of the maximum occurs roughly where the density profile  $\rho(0, y)/\rho_b = 0.5$ . Thus, as the chemical potential is varied, the local compressibility maximum splits and shifts along the  $y$ -axis in the gap between the blocks. Recall that along the  $y$ -axis the system is symmetric around the origin, therefore for small  $\beta\Delta\mu$  there is a peak in  $\chi(\mathbf{r})$  at each of the entrances to the gap, i.e. for  $y \approx \pm 5\sigma$  [cf. Fig. 5.10].

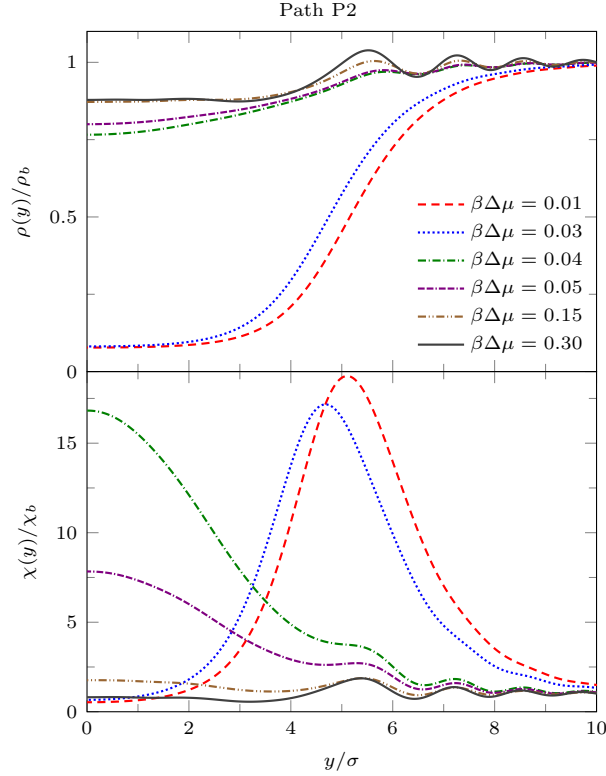


Figure 5.12: Density profiles  $\rho(y) \equiv \rho(0, y)$  and local compressibility  $\chi(y) \equiv \chi(0, y)$  along path P2 for various values of the chemical potential and for  $T = 0.8T_c$ ,  $\beta\epsilon_{wf} = 0.3$  and fixed distance  $x_G = 7\sigma$  between the blocks ( $y = 0$ ) into the bulk liquid ( $y = \infty$ ) parallel to the vertical surfaces of the two blocks – see Fig. 5.8.

#### 5.4.1.2 Varying the separation between the blocks

In Fig. 5.13 we show how the mid-point density  $\rho(0, 0) \equiv \rho_0$ , varies as the distance between the two blocks  $x_G$  is changed. The figure also shows how the local compressibility at the origin  $\chi(0, 0) \equiv \chi_0$  varies with  $x_G$ . For  $\beta\Delta\mu = 0.1, 0.2$  and  $0.3$  there is a discontinuous change in the density. The magnitude of the ‘jump’ gets larger as  $\beta\Delta\mu$  approaches zero. Note that if the density, or more precisely the adsorption, jumps from one finite to another finite value at a particular value of  $x_G$  then so must the local compressibility. This is a signature of the first order transition which occurs in the present mean-field DFT treatment. For  $\beta\Delta\mu \gtrsim 0.4$  the density varies smoothly with  $x_G$ . In the lower panel of Fig. 5.13 we observe a peak in  $\chi_0$  when the mid-point density crosses  $\rho_0/\rho_b = 0.5$ . The height of this peak appears to be maximal at  $\beta\Delta\mu \approx 0.4$ , the value at which the transition in  $\rho_0$  appears to change from discontinuous to continuous. In other words, capillary evaporation

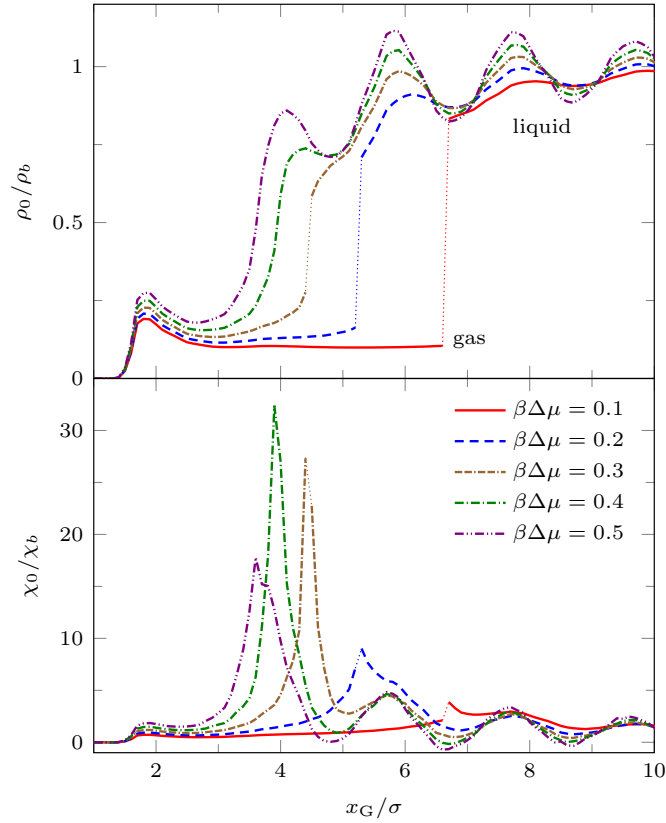


Figure 5.13: Mid point density,  $\rho(0,0) = \rho_0$ , and compressibility  $\chi(0,0) = \chi_0$ , as a function of the distance between the blocks  $x_G$ , for various values of the chemical potential and fixed  $T$ . These are for fixed  $T = 0.8T_c$  and  $\beta\varepsilon_{wf} = 0.3$ . The jumps in  $\rho_0$  are marked with dotted lines for  $\beta\Delta\mu = 0.1, 0.2$  and  $0.3$ . There are accompanying jumps in  $\chi_0$  at the same state points, that are not easy to ascertain on the scale of these plots. For  $\beta\Delta\mu = 0.5, 0.4$  we observe continuous variation of  $\rho_0$  and  $\chi_0$ . There is no sharp, first order transition. A critical transition must occur, within mean-field, between  $\beta\Delta\mu = 0.3$  and  $0.4$ , resulting in a divergence of  $\chi_0$ .

still manifests itself as a first order transition, with its accompanying critical point, in our mean-field treatment of ‘evaporation’ between two blocks of finite cross-sectional area. Bearing in mind the effectively one-dimensional nature ( $b$  and  $c$  finite but  $a \rightarrow \infty$ ) of the capillary-evaporation-like transition we observe in the fluid between the blocks, we expect the divergence in  $\chi_0$  to be rounded, in reality, by finite size effects. Likewise, we expect the jump in  $\rho_0$  to be rounded in reality.

In Fig. 5.14 we display a plot of the excess grand potential per unit length,  $W(x_G) \equiv (\Omega(x_G) - \Omega_\infty)/a$ , as a function of  $x_G$ .  $\Omega_\infty \equiv \Omega(x_G \rightarrow \infty)$  is the value of the grand potential when the two blocks are far apart.  $W(x_G)$  is the solvent mediated interaction potential per unit length between the two blocks. Since  $W(x_G)$  becomes increasingly negative as  $x_G$  decreases, this indicates that the

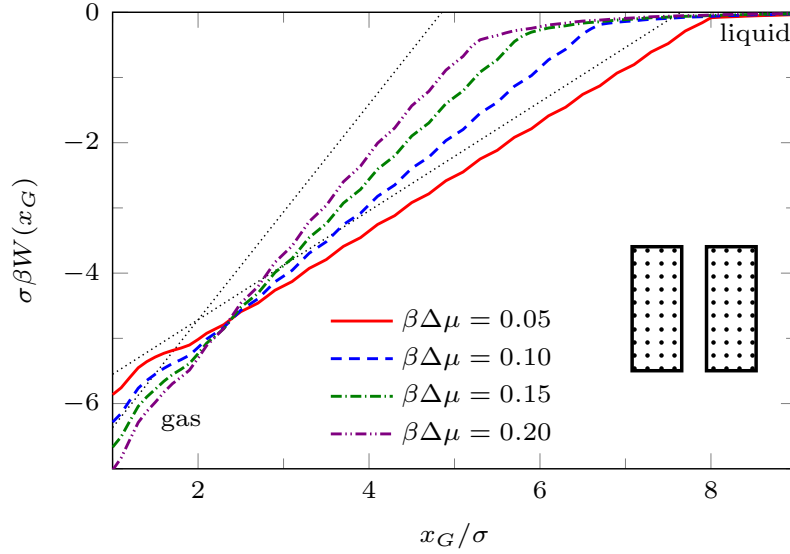


Figure 5.14: The solvent mediated potential (excess grand potential) between a pair of solvophobic blocks, as a function of distance between blocks  $x_G$  for fixed  $T = 0.8T_c$  and  $\beta\varepsilon_{wf} = 0.3$ . The dotted lines are the estimates for the two cases  $\beta\Delta\mu = 0.05$  (lower) and  $0.20$  (upper) calculated from Eq. (5.4.4), with  $E = 0$ . The DFT results display two branches – see text.

solvent mediated interaction between the pair of solvophobic blocks is attractive. For smaller  $\beta\Delta\mu$ , i.e. for states nearer to coexistence, the solvent mediated potential  $W(x_G)$  is longer ranged; the gas intrusion between the blocks lowers the free energy out to larger separations. Close inspection of Fig. 5.14 shows that there are actually two solution branches to the grand potential. For  $\beta\Delta\mu \gtrsim 0.4$  there is only a single smooth branch (not shown). When there are two branches, the one at large  $x_G$  corresponds to the case when the density between the blocks is liquid-like and the other, at smaller  $x_G$ , to when there is a gas-like intrusion. Where the branches meet corresponds to the value of  $x_G$  where the evaporation transition occurs for a given  $\beta\Delta\mu$ . The solvent mediated force between the blocks jumps at the transition. Note that the potential  $W(x_G)$  in Fig. 5.14 for *finite* size blocks (i.e. finite  $b$ ) is very different from the corresponding potential between two infinite planar walls (i.e.  $b \rightarrow \infty$ ). For example, from Fig. 5.14 we see that when  $\beta\Delta\mu = 0.05$  the two branches in  $W(x_G)$  meet at  $x_G \approx 8\sigma$ . In contrast, for the infinite walls at the same  $\beta\Delta\mu$ , the two branches meet at  $x_G \approx 21\sigma$ .

In the same manner used to derive the Kelvin equation (5.3.9), we can use macroscopic thermodynamics to obtain a simple estimate for  $W(x_G)$ . The grand potential of the system with no

blocks present is  $\Omega_0 = -p_l V$ , where  $p_l$  is the pressure of the bulk liquid and  $V$  is the volume of the system. The grand potential of the system with one block present in the liquid is

$$\Omega_1 = -p_l(V - ab^*c^*) + 2(ac^* + ab^*)\gamma_{wl} + 4aE_l \quad (5.4.2)$$

where,  $a$ ,  $b^*$ ,  $c^*$  are the effective dimensions of the block, as illustrated in Fig. 5.8. Note that  $b^*c^* > bc$  is the effective cross sectional area of the block, which includes the fluid exclusion region around the blocks, as discussed below Eq. (5.4.1). Thus  $(V - ab^*c^*)$  is the volume occupied by the liquid. Recall that we assume the block is long, i.e.  $a \rightarrow \infty$ .  $2(ac^* + ab^*)$  is the surface area of the block in contact with the liquid and  $\gamma_{wl}$  is the planar wall-liquid interfacial tension.  $E_l$  is a free energy per unit length so that the final term in Eq. (5.4.2) is the line-tension-like contribution to the grand potential arising from the four edges of the block (corners on the cross-section in Fig. 5.8) in contact with the liquid.

Similarly, we can estimate the grand potential when there are two blocks present. If the pair of blocks are close enough together (see e.g. the density profile for  $\beta\Delta\mu = 0.01$  in Fig. 5.9) there is a portion of ‘gas’ phase between the blocks, so the grand potential is

$$\begin{aligned} \Omega_2 = & -p_l(V - 2ab^*c^* - ab^*x_G^*) - p_g ab^*x_G^* \\ & + (4ac^* + 2ab^*)\gamma_{wl} + 2ab^*\gamma_{wg} + 2ax_G^*\gamma_{gl} \\ & + 4aE_l + 4aE_{gl}, \end{aligned} \quad (5.4.3)$$

where  $p_g$  is the pressure of the gas at the same chemical potential as the (bulk) liquid.  $x_G^*$  is the effective thickness of the ‘gas’ region between the blocks and as when implementing the Kelvin equation (5.3.9), we set  $x_G^* = x_G - 2\sigma$ .  $\gamma_{wg}$  is the planar wall-gas interfacial tension,  $\gamma_{gl}$  is the planar gas-liquid interfacial tension and  $E_{gl}$  is the free energy per unit length contribution, i.e. the final term in Eq. (5.4.3) is due to the inner edges of the blocks connecting to a gas-liquid interface. Hence, from Eqs. (5.4.2), (5.4.3) and (5.3.4) the solvent mediated potential,  $W(x_G^*) = (\Omega_2 - 2\Omega_1 + \Omega_0)/a$ , is given by

$$W(x_G^*) \approx E + 2b^*\gamma_{lg} \cos \theta + [2\gamma_{gl} + b^*(\rho_l - \rho_g)\Delta\mu]x_G^*, \quad (5.4.4)$$

where  $E = 4(E_{gl} - E_l)$ . We have used the standard Taylor expansion of the pressures around

the value at gas-liquid bulk coexistence,  $p_{\text{coex}}$ , to give  $p_l - p_g \approx (\rho_l - \rho_g)\Delta\mu$ , where  $\rho_l$  and  $\rho_g$  are the coexisting bulk liquid and gas densities, respectively. Eq. (5.4.4) predicts that the solvent mediated potential is linear in the distance between the blocks  $x_G^*$ , and thus the force  $-\partial W/\partial x_G^* = -2\gamma_{gl} - b^*(\rho_l - \rho_g)\Delta\mu$  is constant when there is a gas-like state between the blocks. The result from Eq. (5.4.4), with  $E = 0$ , is displayed as the thin dotted lines in Fig. 5.14 for the two extreme cases,  $\beta\Delta\mu = 0.05$  and  $0.2$ . One can see that the gradient of  $W(x_G)$  predicted by Eq. (5.4.4) agrees very well with the DFT results. However, each line is shifted vertically relative to the DFT curve. This is probably the consequence of having neglected the unknown contribution from the edges,  $E$ . The difference between the result from Eq. (5.4.4) and the DFT implies that  $|E| < 0.5k_B T/\sigma$ . Note that the force  $-\partial W/\partial x_G^*$  does not depend on  $E$ , nor on  $\cos\theta$ . That the macroscopic thermodynamic result in Eq. (5.4.4) agrees rather well with the microscopic DFT results might, once again, come as a surprise to some readers, bearing in mind the microscopic cross-sectional size of the blocks and that the distance between these is only a few solvent particle diameters. The validity of Eq. (5.4.4) is partly due to the fact that the correlation length in the intruding gas state is rather short, but this kind of agreement between results of microscopic DFT and simple macroscopic thermodynamic estimates has been observed previously for related problems; see e.g. Refs. [70, 71, 69, 72]. Note that the condition  $W(x_G^*) = 0$  in Eq. (5.4.4) yields

$$x_G^* = \frac{-2\gamma_{lg} \cos\theta}{(\rho_l - \rho_g)\Delta\mu + 2\gamma_{lg}/b^*} \quad (5.4.5)$$

for the separation at which capillary evaporation occurs for identical blocks, i.e. the ‘gas’ is thermodynamically stable relative to the liquid for smaller separations. This is a particular case of the formula introduced by Lum and Luzar [77]. In the limit  $b^* \rightarrow \infty$ , the solvent mediated force per unit area is constant, equal to  $(\rho_l - \rho_g)\Delta\mu$ , in the ‘gas’. The same result is valid for  $\Delta\mu \rightarrow 0$ , in the condensed ‘liquid’ in the case of capillary condensation [29].

### 5.4.2 Two Solvophilic Blocks

So far we have discussed the properties of an identical pair of solvophobic blocks. Now we increase the parameter  $\varepsilon_{wf}$  so that the surface of the blocks attracts more strongly the liquid, i.e. the surfaces of the blocks become solvophilic. We set  $\beta\varepsilon_{wf} = 1$ , which for the planar wall has the contact angle

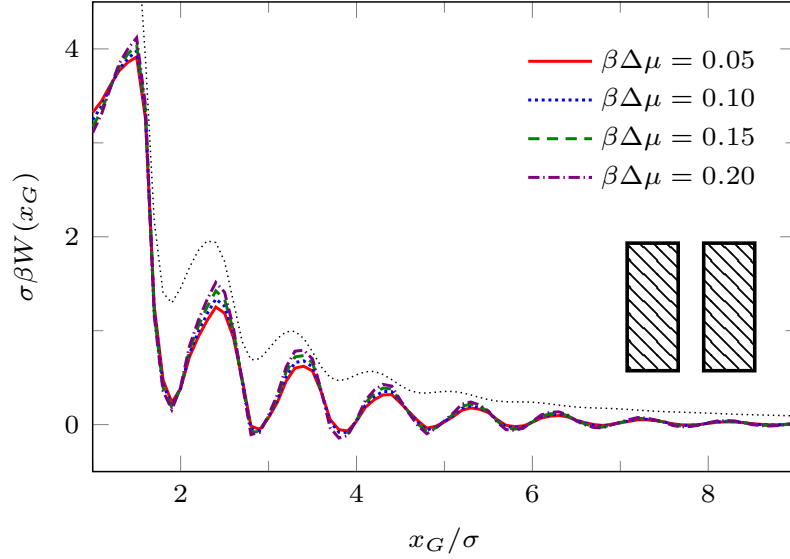


Figure 5.15: The solvent mediated potential (excess grand potential) between a pair of solvophilic blocks, as a function of distance between blocks  $x_G$  for fixed  $T = 0.8T_c$  and  $\beta\varepsilon_{wf} = 1$ . Note that the contact angle for this choice of parameters is  $\theta \approx 44^\circ$ . The black dotted line is the corresponding potential per unit area between infinite walls multiplied by  $b$ , the height of the blocks.

$\theta = 43.7^\circ$ , see Fig. 5.5. The density profiles for the blocks of the same dimensions (not displayed) are, for all values of  $\beta\Delta\mu$ , qualitatively similar to the profile corresponding to  $\beta\Delta\mu = 0.4$  in Fig. 5.9, but with higher densities at the surface of the blocks and larger amplitude oscillations in the density profile around the blocks. The same is true for the local compressibility. The key difference between a pair of solvophobic blocks and a pair of solvophilic blocks is that there is no capillary evaporation of the liquid in the gap between the solvophilic blocks as  $\beta\Delta\mu \rightarrow 0$ . This has profound consequences for the solvent mediated potential.

Fig. 5.15 shows the solvent mediated potential  $W(x_G)$  between the solvophilic blocks. We see pronounced oscillations as the distance between the blocks is decreased. Also, since  $W(x_G)$  decreases (albeit in damped oscillatory fashion) as  $x_G$  is increased, this indicates that the effective interaction potential between a pair of solvophilic blocks is repulsive. Note that  $W(x_G)$  is almost independent of  $\beta\Delta\mu$  in this particular case. The results in Fig. 5.15 are quite similar to those obtained for two planar walls with the same  $\beta\varepsilon_{wf}$  (thin dotted black line). Note that for planar walls the asymptotic decay,  $L \rightarrow \infty$ , of the excess grand potential per unit area  $W(L)$  is known [78, 79] for various choices of the fluid-fluid and wall-fluid potentials. For our present choice [Eqs. (5.2.2) and (5.3.7)], with

$\beta\varepsilon_{wf} = 1$ , theory predicts  $\beta W(L) \sim 0.933L^{-2}$ , as  $L \rightarrow \infty$ , i.e. the solvent mediated force per unit area  $-(\partial W/\partial L)_{T,\mu}$  is repulsive and decays  $\sim L^{-3}$  [see Appendix A]. We are not able to investigate the asymptotics numerically for blocks.

### 5.4.3 One Solvophobic and One Solvophilic Block and Patchy Blocks

The two previous subsections discuss the solvent mediated interactions  $W(x_G)$  between pairs of blocks that are identical. We now present results for  $W(x_G)$  for the case when one of the blocks is solvophobic and the other is solvophilic. We also consider various pairs of block having a mixture of solvophobic and solvophilic patches. We split each block into a maximum of three segments. The DFT results for the solvent mediated potentials between the various blocks are shown in Fig. 5.16, with the inset giving a sketch of the arrangement of the patches: dotted regions are solvophobic and diagonally striped regions are solvophilic. In all cases in Fig. 5.16, we notice that there is a local minimum of  $W(x_G)$  occurring when  $x_G \approx 2\sigma$ . This is the distance at which the two exclusion zones around the blocks meet, so that for  $x_G$  less than this value, the fluid density between the blocks is almost zero. In general, the range of the solvent mediated interaction decreases as  $\beta\Delta\mu$  is increased. Note that having blocks with only one solvophobic segment causes the solvent mediated potential  $W(x_G)$  to become attractive. Nevertheless,  $W(x_G)$  retains the oscillatory behaviour of the pure solvophilic blocks observed in Fig. 5.15. Furthermore, the oscillations in the potential are enhanced when the solvophilic patches are together on the ends of the blocks – see Fig. 5.16(d). In Fig. 5.17 we display a series of density profiles and local compressibility profiles corresponding to all the cases displayed in Fig. 5.16. We observe that whenever two solvophobic segments are opposite one another, a gas-like region forms between the blocks provided these are sufficiently close (as they are in Fig. 5.17) and this leads to large values of the local compressibility  $\chi(\mathbf{r})$  in these regions.

It is particularly instructive to compare the results in Figs. 5.16(e) and 5.17(e), corresponding to two solvophobic patches facing each other at both ends of the blocks, with the corresponding ones for identical uniform solvophobic blocks, Figs. 5.9, 5.10 and 5.14. For  $\beta\Delta\mu = 0.05$ , the solvent mediated potential in Fig. 5.16(e) has a form close to that in Fig. 5.14. The separation,  $x_G \approx 5\sigma$ , at which capillary evaporation occurs is smaller for the patchy case than for the uniform case,  $x_G \approx 8\sigma$ . However, in both cases one finds a linear solvent mediated potential at small separations; the magnitude of the force is similar in both cases. Such behaviour is consistent with reduced area

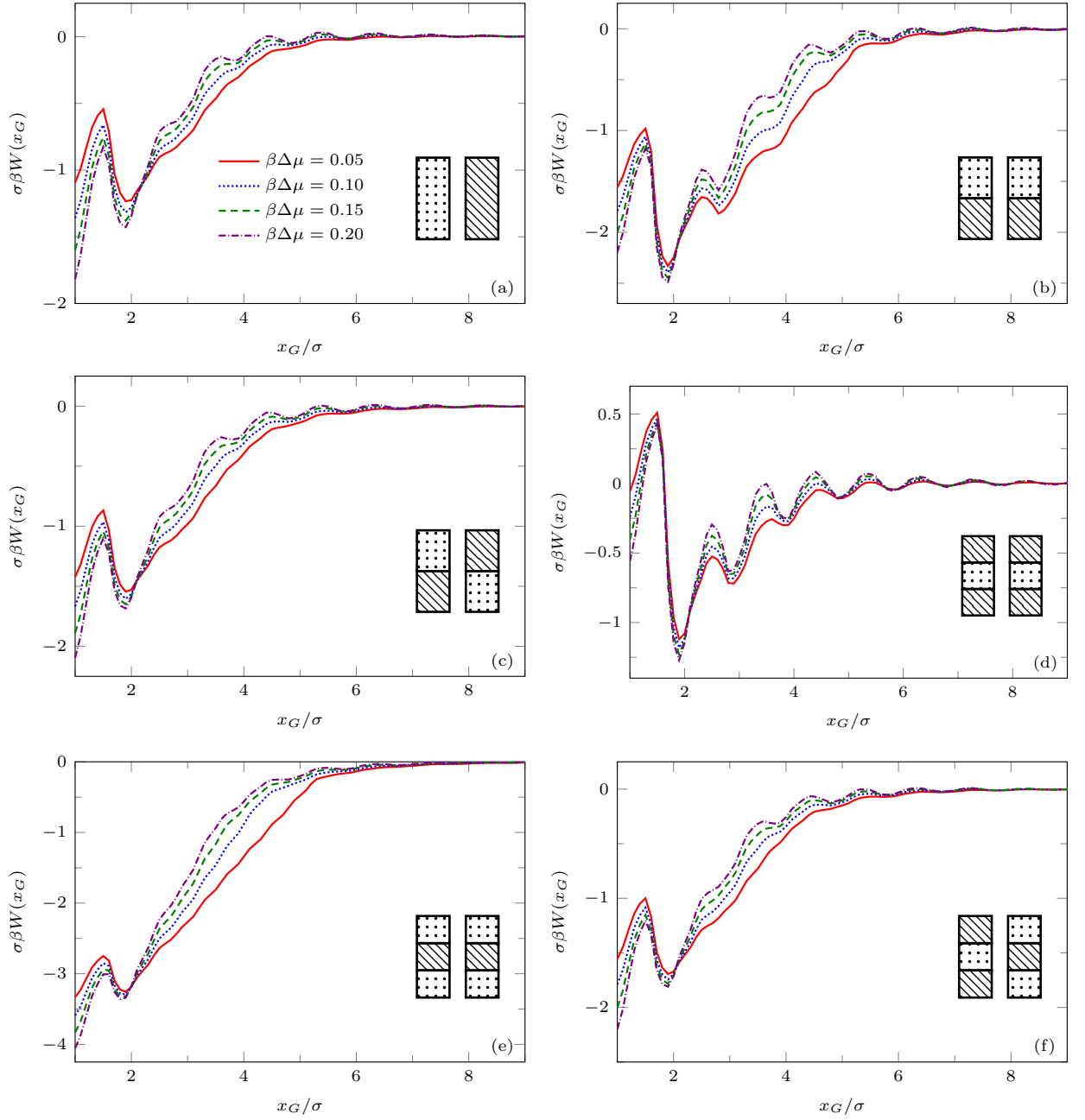


Figure 5.16: The solvent mediated potential (excess grand potential) between various pairs of blocks as a function of distance between blocks,  $x_G$ , for fixed  $T = 0.8 T_c$ . The structure of each block is specified by the inset where dots represent solvophobic areas ( $\beta\varepsilon_{wf} = 0.3$ ) and the diagonal lines represent solvophilic areas ( $\beta\varepsilon_{wf} = 1$ ). When patchy blocks are aligned the same way, we call this ‘even’ alignment, otherwise we refer to this as ‘odd’. Thus, in (b) there is even and in (c) odd alignment. For (d)-(f) the block is split into three segments; (d) and (e) are even while (f) is odd.

of (facing) solvophobic regions. Recall that for two identical blocks Eq. (5.4.4) implies that the force does not depend on  $\cos\theta$ .

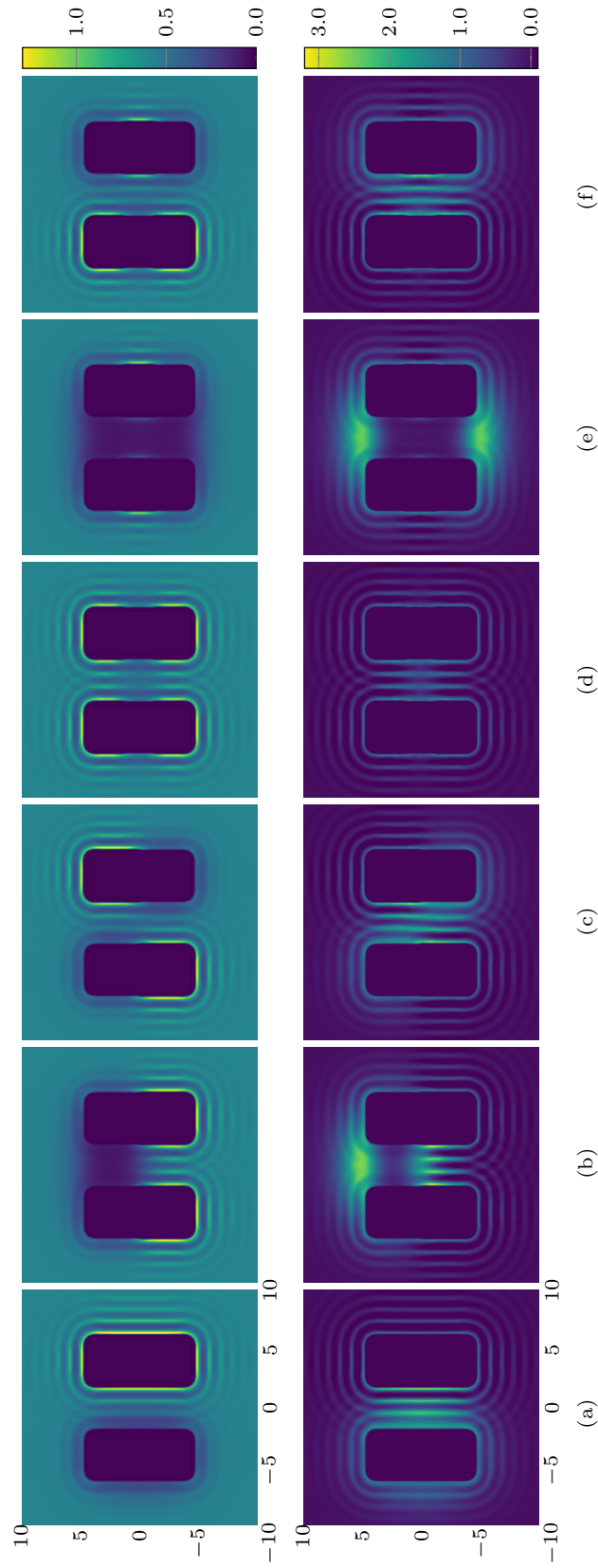


Figure 5.17: Liquid density profiles  $\sigma^3\rho(x, y)$  (top) and the local compressibility  $k_B T \sigma^3 \chi(x, y)$  (bottom) around different pairs of blocks for the temperature  $T = 0.8T_c$  and chemical potential  $\beta\Delta\mu = 0.01$ . In all cases the blocks are a distance  $x_G = 5\sigma$  apart. The labels (a)-(f) refer to the same pair of blocks as described in Fig. 5.16.

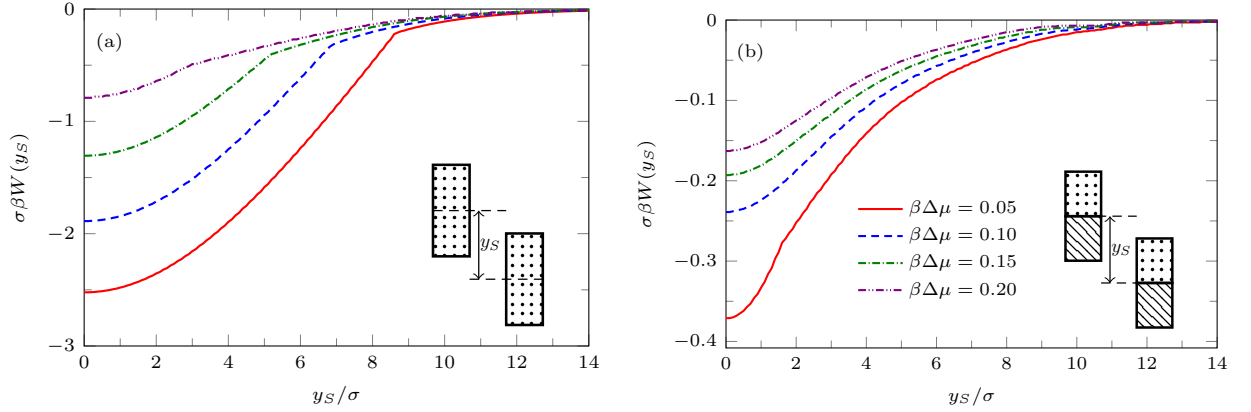


Figure 5.18: The solvent mediated potential (excess grand potential) between (a) an identical pair of solvophobic blocks and (b) a pair of patchy blocks divided into two segments: half solvophobic and half solvophilic, aligned evenly, as a function of  $y_S$ , the vertical distance between the horizontal lines through the block mid-points – see inset. For the solvophobic segment  $\beta\varepsilon_{wf} = 0.3$  and for the solvophilic segment  $\beta\varepsilon_{wf} = 1$ .  $T = 0.8T_c$  and  $x_G = 5\sigma$ . Note that in (a) and (b) there are two branches – see text.

#### 5.4.4 Blocks Shifted Vertically

The results presented in the previous subsections are for the case when the centres of the blocks are at  $y = 0$  and only the distance between the closest faces  $x_G$  is varied. Now we fix  $x_G = 5\sigma$  and move one of the blocks vertically along the  $y$ -axis [cf. inset of Fig. 5.18]. The vertical distance from the  $x$ -axis is defined as  $y_S$  (in the previous subsections  $y_S = 0$ ). The solvent mediated potential  $W(y_S)$  for a pair of solvophobic blocks and a pair of patchy blocks (divided into two segments: half solvophobic and half solvophilic, aligned evenly) is shown in Fig. 5.18. In both cases we see that  $W(y_S)$  is attractive, with a minimum at  $y_S = 0$ . This indicates that the preferred position (lower grand potential) is when the pair of blocks are aligned, with  $y_S = 0$ . We also see that for a given chemical potential the range and depth of the potential is greater for a pair of fully solvophobic blocks [Fig. 5.18(a)] than for a pair of two-segment blocks aligned evenly [Fig. 5.18(b)]. This is as one would expect, since the amount of solvophobic area on each block is greater in the former case (a). For a pair of solvophobic blocks, we showed in Fig. 5.14 that the solvent mediated potential  $W(x_G)$  varies approximately linearly with  $x_G$ , on the ‘gas branch’ arising for smaller values of  $x_G$ . However, we see from Fig. 5.18(a) that for fixed  $x_G$  the solvent mediated potential is not a linear function of  $y_S$ . For the pair of two-segment blocks aligned evenly (Fig. 5.18(b)) we do not see

any oscillations in the solvent mediated potential as  $y_S$  is varied – recall that there are oscillations as  $x_G$  is varied – see Fig. 5.16(b). Close inspection of Fig. 5.18 shows that within the present mean-field DFT approach there are actually two solution branches to the grand potential for both types of blocks. The branch for large  $y_S$  corresponds to a liquid-like density between the blocks while the other branch at smaller  $y_S$ , corresponds to the density between the blocks being gas-like. Consistent with our earlier discussion, the evaporation transition occurs at the value of  $y_S$  where the two branches meet and the solvent mediated force between the blocks jumps at this point. The value of  $y_S$  at which this transition occurs varies with  $\beta\Delta\mu$ .

Note that it is straightforward to derive a formula for  $W(y_S)$  analogous to that in Eq. (5.4.4), making the same assumptions. However, the assumption that the gas-liquid interface meets the blocks at the corners is no longer necessarily true and the resulting formula gives poor agreement with the DFT.

#### 5.4.5 Blocks at an Angle

So far we have considered pairs of blocks with their faces aligned parallel to each other. We now consider a pair of identical solvophobic blocks with the second block rotated by an angle  $\alpha$  with respect to the centre of the first, i.e.  $\alpha$  is the angle between the orientation vectors of the two blocks. In Fig. 5.19 we plot the density and compressibility profiles as the angle  $\alpha$  is varied whilst keeping the distance between the centres of the blocks fixed,  $x_C = 8\sigma$  (note that  $x_C \neq x_G$ ). The temperature  $T = 0.8T_c$  and chemical potential  $\beta\Delta\mu = 0.05$  are also fixed. We present results for a range of angles; by symmetry we only need to consider the range  $0^\circ \leq \alpha \leq 90^\circ$ .

Fig. 5.19 (top) shows that as  $\alpha$  is increased for fixed  $x_C = 8\sigma$ , the gas-like region between the blocks remains. The area of one of the interfaces between the gas-like region and the bulk liquid increases, while the other decreases. Additionally, we see that the volume of the gas-filled region between the blocks decreases as  $\alpha$  is increased from zero, since the blocks become closer to each other. Note also that for the larger values of  $\alpha$ , the gas-liquid interface does not connect to the corners of the blocks, which must be taken into account if generalising Eq. (5.4.4) to derive an approximation for  $W$  as a function of  $\alpha$ . From the corresponding compressibility profiles in Fig. 5.19 (bottom) we see that  $\chi(\mathbf{r})$  is largest in the gas-liquid interfaces, as previously. Also, the peak value of the compressibility increases as  $\alpha$  is increased from zero, attaining its maximum value

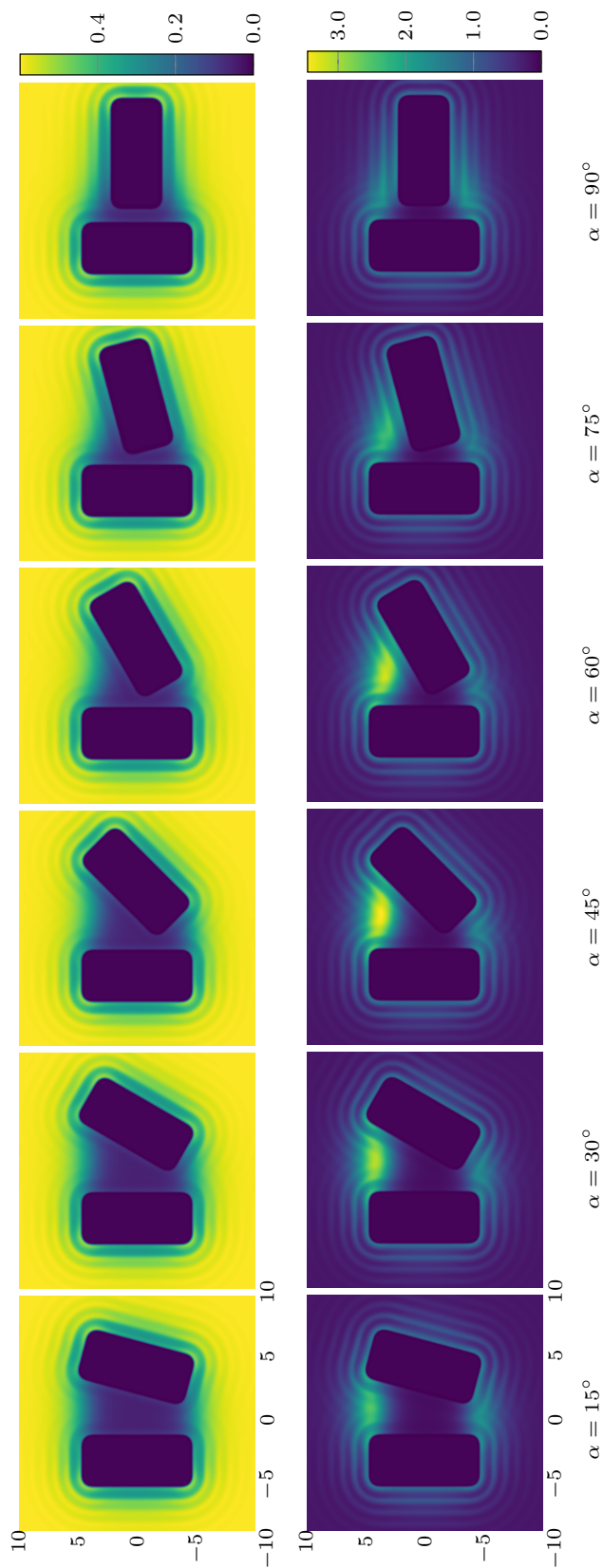


Figure 5.19: Liquid density profiles  $\sigma^3 \rho(x, y)$  (top) and the local compressibility  $k_B T \sigma^3 \chi(x, y)$  (bottom) around a pair of (identical) solvophobic blocks, for fixed temperature  $T = 0.8 T_c$  and chemical potential  $\beta \Delta \mu = 0.05$ . The distance between the centre of blocks is fixed:  $x_C = 8\sigma$  and the relative orientation angle  $\alpha$  is varied. The density and compressibility profiles for  $\alpha = 0$  are not shown since these form part of the sequence in Figs. 5.9 and 5.10.

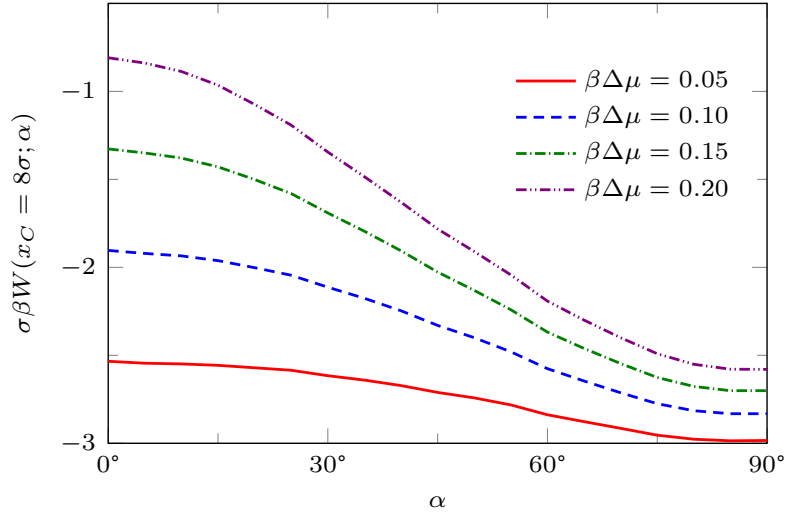


Figure 5.20: The solvent mediated potential (excess grand potential) between a pair of solvophobic blocks for various values of chemical potential as a function of the relative orientation angle,  $\alpha$ . As in Fig. 5.19 we fix the centres of the pair of blocks such that the distance between the centres  $x_C = 8\sigma$  and rotate one of the blocks by  $\alpha$ .  $T = 0.8T_c$  and  $\beta\varepsilon_{wf} = 0.3$ .

when  $\alpha \approx 45^\circ$ . Increasing  $\alpha$  further leads to a drop in the peak value of the compressibility.

In Fig. 5.20 we plot the solvent mediated potential for two solvophobic blocks as a function of  $\alpha$  for fixed distance between the centres of the blocks,  $x_C = 8\sigma$ , corresponding to the profiles in Fig. 5.19. We see that the minimum of the solvent mediated potential occurs when  $\alpha = 90^\circ$  for fixed  $x_C = 8\sigma$ . This is because as the angle is varied, the blocks become closer to each other as  $\alpha \rightarrow 90^\circ$  (see Fig. 5.19) and this leads to the excess grand free energy being lower. However, if we rotate the solvophobic blocks *and* also move the centres of the blocks such that closest distance between the two blocks  $x_G$  is always constant, we find the minimum of the grand potential is when  $\alpha = 0^\circ$  (not shown). In this case, it is because rotating to  $\alpha = 90^\circ$  results in a smaller area of the block surfaces being opposite one another than when  $\alpha = 0^\circ$ . Generically the attractive well in the solvent mediated potential between the blocks becomes deeper (i.e. stronger attraction) as  $\beta\Delta\mu \rightarrow 0$ .

In order to analyse further the solvent mediated potential between the solvophobic blocks, we fix the relative orientation between the blocks at  $\alpha = 45^\circ$  and vary the separation between the blocks  $x_G$ , which is the distance between the closest points on the pair of blocks.  $W(x_G)$  is shown in Fig. 5.21 for fixed temperature  $T = 0.8T_c$  and wall attraction  $\beta\varepsilon_{wf} = 0.3$ . In the inset we sketch

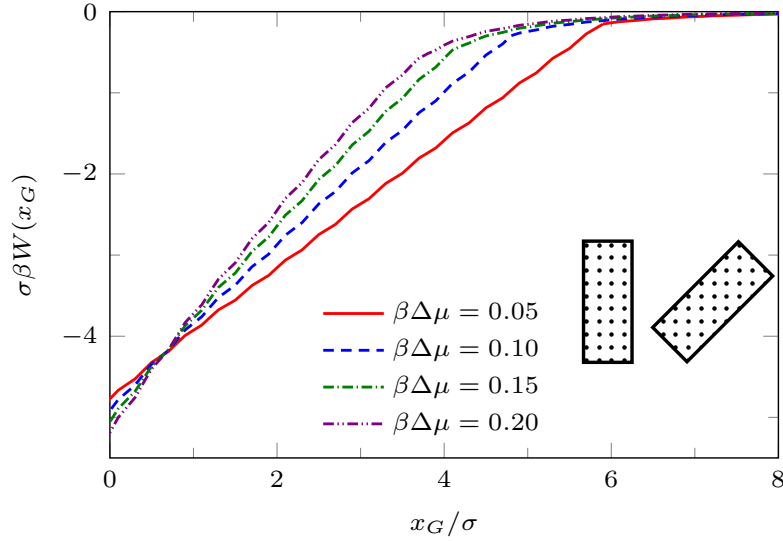


Figure 5.21: The solvent mediated potential (excess grand potential) between a pair of solvophobic blocks for various values of the chemical potential as a function of the distance between the closest points of the blocks,  $x_G$ , with one of the blocks rotated at fixed angle  $\alpha = 45^\circ$ .  $T = 0.8T_c$  and  $\beta\varepsilon_{wf} = 0.3$ . Note that for small values of  $\beta\Delta\mu$  there are two branches – see text.

the relative orientations of the two blocks. Thus,  $x_G$  is the distance from the left-most corner of the right hand block to the near face of the left hand block. From Fig. 5.21, we see that the solvent mediated potential between the pair of solvophobic blocks with fixed  $\alpha = 45^\circ$  is qualitatively similar to that for  $\alpha = 0^\circ$ , see Fig. 5.14. For small  $\beta\Delta\mu$ , i.e. for states nearer to coexistence, the solvent mediated potential  $W(x_G)$  is longer ranged (although not as long-ranged as when the faces are parallel,  $\alpha = 0^\circ$ , shown in Fig. 5.14) and also has two solution branches to the grand potential. The branch for large  $x_G$  corresponds to the liquid-like density between the blocks and the other, at smaller  $x_G$ , is when the density between the blocks is gas-like. Once again the evaporation transition occurs at the value of  $x_G$  where the two branches cross and the solvent mediated force jumps at this value of  $x_G$  for the given  $\beta\Delta\mu$ .

## 5.5 Concluding Remarks

Using classical DFT we have calculated the liquid density profile and the local compressibility around pairs of solvophobic, solvophilic and patchy blocks immersed in a simple LJ like solvent. We have also calculated an important thermodynamic quantity, namely the solvent mediated interaction

potential between the blocks  $W(x_G)$ . When both blocks are solvophobic, the potential  $W(x_G)$  is an almost linear function at small separations  $x_G$ , is strongly attractive and is very sensitive to the value of  $\beta\Delta\mu$ ; see Fig. 5.14. In this regime, treating the system using macroscopic thermodynamics, i.e. using Eq. (5.4.4), turns out to be a rather good approximation for  $W(x_G)$ . This success of macroscopic theory may seem surprising, given that the blocks we consider have the microscopic cross sectional area  $\approx 10\sigma \times 5\sigma$ . However, it is in keeping with recent simulation studies [49, 51] of water induced interactions between hydrophobes. In contrast, when both blocks are solvophilic, the potential  $W(x_G)$  is oscillatory but overall repulsive and exhibits only a weak dependence on  $\beta\Delta\mu$ ; see Fig. 5.15. When the blocks are patchy, the nature of the solvent mediated potential is complex. However, we find that if solvophobic patches are present, are sufficiently large and near to one another (facing each other on the opposing blocks), then their contribution to the effective potential dominates (see Fig. 5.16). Then the potential  $W(x_G)$  is still strongly attractive and is nearly linear in  $x_G$  for small  $\beta\Delta\mu$ , particularly if the solvophobic patches are on the ends of the blocks [see Fig. 5.16(e)]. From Fig. 5.18 we see that for fixed  $x_G$  there is a minimum in  $W$  as a function of the vertical distance  $y_S$ , when the solvophobic patches on the blocks are aligned.

For a pair of identical solvophobic blocks, the solvent mediated potential per unit length of the blocks is  $\approx -5k_B T$  when the blocks are close to contact (see Fig. 5.14). Thus, if we assume that the blocks are actually finite in length, with length  $a = 10\sigma$  (i.e. finite blocks of size  $10\sigma \times 10\sigma \times 5\sigma$ ), then when the blocks are close to contact we have  $W(x_G \lesssim \sigma) \approx -50k_B T$  or about  $-120 \text{ kJ mol}^{-1}$  at ambient temperature. This is the same order of magnitude as the solvent mediated potentials between a hydrophobic (polymeric) solute of a similar size and a hydrophobic SAM surface measured in computer simulations employing a realistic model of water – see Fig. 6(c) in Ref. [52] and also Ref. [80]. Moreover, it is important to note that when the SAM surface is strongly hydrophobic, the solvent mediated potentials in Ref. [52] display a portion that is almost linear. Hydrophobic interactions also play a role in determining the structure of proteins: simulations suggest capillary evaporation between hydrophobic patches can lead to strong forces between protein surfaces [81]. Given these observations, we expect that the results described here for a simple LJ like liquid incorporate the essential physics of a realistic model of a water solvent close to saturation.

In the vicinity of a single solvophobic surface the solvent density is lower, when  $\beta\Delta\mu$  is sufficiently small. However, the thickness of the depleted layer is only one or two particle diameters – see

Fig. 5.6 corresponding to  $\theta \approx 144^\circ$ . This is consistent with the x-ray studies of water at a water-OTS (octadecyl-trichlorosilane) surface reported in Ref. [82] and with simulation results for SPC/E water at non-polar substrates [83]. When two solvophobic surfaces become sufficiently close a gas-like region forms between the blocks. The extent of this can be large, see e.g. Fig. 5.9, and the density profile passing from the gas inside to the liquid outside of the blocks closely resembles the free gas-liquid interfacial profile – see Fig. 5.12. Moreover, the local compressibility is large in the neighbourhood of this interface, indicating that it is a region with large density fluctuations. Given that this interface is pinned to the corners of the blocks – see Fig 5.9 – we do not expect significant “capillary wave” broadening of the profile beyond the present mean-field DFT, as one would normally expect at a macroscopic free interface.

As the separation between solvophobic blocks is increased, there is a jump in the solvent mediated force when the blocks reach a particular distance,  $x_G = x_J$ , where the state minimising the grand potential changes from one with a gas-like density between the blocks to one where this is liquid-like. Within DFT the potential  $W(x_G)$  has two branches and there is a discontinuity in the the gradient at  $x_J$  – see e.g. Fig. 5.14. We do not display the metastable portions of the branches of  $W(x_G)$ ; these do not extend very far from the crossing point indicating that the height of the nucleation barrier is small. This is due to the small size of the blocks and the small values of  $x_G$ . For hydrophobic surfaces with greater surface area and at a greater distance apart, the free energy barrier should be larger; for a recent discussion of nucleation pathways to capillary evaporation in water see Ref. [60].

We have also studied the local compressibility  $\chi(\mathbf{r})$  in the liquid between and surrounding pairs of blocks of differing nature. The local compressibility exhibits pronounced peaks; these indicate where the local density fluctuations are large. These fluctuations are maximal close to the incipient gas-liquid interface – see for example the central plot in Fig. 5.10, which is for  $\beta\Delta\mu = 0.22$ , and also Fig. 5.17 (b) and (e) for  $\beta\Delta\mu = 0.01$ . Fig. 5.19 displays how for angled blocks  $\chi(\mathbf{r})$  depends on alignment and the confining geometry. When pronounced fluctuations, in conjunction with a depleted surface density, are observed in simulations of water at hydrophobic interfaces, this phenomenon is often ascribed to the disruption of the water hydrogen bonding network. Given that we observe similar behaviour for a simple LJ like liquid close to solvophobic substrates, we argue that this phenomenon is by no means specific to water. Rather it is due (i) to the weak bonding between the fluid and the (solvophobic) surface and (ii) the system being close to bulk

---

gas-liquid phase coexistence, i.e. a small value of  $\beta\Delta\mu$ . Thus, since the LJ like fluid considered here is representative of a broad class of simple liquids, we expect strong attraction between solvophobic surfaces, enhanced density fluctuations near such surfaces and other features of hydrophobicity to manifest themselves whenever the solvent, whatever its type, is near to bulk gas-liquid phase coexistence. There are obvious advantages, both in simulation and theory, in performing detailed investigations for simple model liquids, especially when tackling subtle questions of surface phase transitions such as critical drying [42].

## Chapter 6

# The standard mean-field treatment of inter-particle attraction in classical DFT is better than one might expect

*In classical density functional theory (DFT) the part of the Helmholtz free energy functional arising from attractive inter-particle interactions is often treated in a mean-field or van der Waals approximation. On the face of it, this is a somewhat crude treatment as the resulting functional generates the simple random phase approximation (RPA) for the bulk fluid pair direct correlation function. We explain why using standard mean-field DFT to describe inhomogeneous fluid structure and thermodynamics is more accurate than one might expect based on this observation. By considering the pair correlation function  $g(x)$  and structure factor  $S(k)$  of a one-dimensional model fluid, for which exact results are available, we show that the mean-field DFT, employed within the test-particle procedure, yields results much superior to those from the RPA closure of the bulk Ornstein-Zernike equation. We argue that one should not judge the quality of a DFT based solely on the approximation it generates for the bulk pair direct correlation function.*

### 6.1 Introduction

Classical density functional theory (DFT) [19, 18, 20, 21, 9] is based on the idea that the thermodynamic grand potential of an inhomogeneous fluid can be expressed as a functional of the average

one-body density profile  $\rho(\mathbf{r})$ . Minimising an (approximate) functional with respect to  $\rho(\mathbf{r})$  provides an estimate of the equilibrium density profile and the grand potential. DFT has proved to be a versatile tool for determining the thermodynamic quantities arising in the physics of adsorption and fluid interfaces. These include, for example, interfacial tensions [18] and the solvation force (excess pressure) for confined fluids [29, 84]. Since DFT provides directly the grand potential it is particularly well-suited to investigations of surface phase behaviour and perhaps it is here where DFT has had most success, revealing new phenomena and new physical insight [18, 9]. DFT also provides a direct measure of density fluctuations in the inhomogeneous fluid via the local compressibility  $(\partial\rho(\mathbf{r})/\partial\mu)$ , where  $\mu$  is the chemical potential and recent papers have investigated this quantity for liquids at solvophobic planar substrates [53] and confined between a variety of nanostructures [85]. In addition to the one-body density, higher order correlation functions can be obtained by taking further functional derivatives of the free energy functional. In particular, the two-body pair direct correlation function  $c^{(2)}(\mathbf{r}, \mathbf{r}')$  is proportional to the second functional derivative of the excess Helmholtz free energy with respect to the density [19, 18, 21, 9]. It is tempting to assess the quality of an approximate DFT for a given model fluid by comparing the resulting  $c^{(2)}(r)$  for a homogeneous fluid with that obtained from computer simulation of the radial distribution function  $g(r)$  or structure factor  $S(k)$  or from integral equation theories; see Refs. [18, 21, 9] and references therein. In this paper we explain why this might not be the best means of testing the accuracy of a free energy functional.

We focus on the much-used excess Helmholtz free energy functional [Eq. (6.3.4) below] that treats the attractive inter-particle interactions in a mean-field (MF) or van der Waals approximation. This standard MF DFT is considered the ‘work-horse’ for applications of DFT to interfaces, adsorption and many other inhomogeneous situations, see e.g. Refs. [18, 20, 21, 9, 29, 84, 53, 85]. Taking two derivatives of this functional and evaluating for a uniform density  $\rho_b$ , corresponding to the (bulk) fluid, leads to the pair direct correlation function  $c_{\text{RPA}}^{(2)}(r)$  that forms the basis for the well-known random phase approximation (RPA) [19, 9, 2, 86]. Recognising this connection between the MF DFT and the RPA, one might assume that the fluid structure, thermodynamics and phase behaviour predicted by the MF DFT is of similar quality to that resulting from the RPA closure to the bulk Ornstein-Zernike (OZ) equation. Here, we argue: (i) Results from the MF DFT are more accurate than one might expect from examining bulk pair correlation functions extracted from

the RPA closure to the OZ equation and (ii) one should not judge the quality of the MF DFT, or any other approximate DFT, solely upon what the approximate functional generates by taking two functional derivatives. We make these arguments explicit by considering the test-particle limit of Percus [87], i.e. we calculate the inhomogeneous fluid density profile  $\rho(r)$  around a fixed particle of the same type as the surrounding fluid. This enables us to calculate the fluid radial distribution function  $g(r) = \rho(r)/\rho_b$ . By rewriting the Euler-Lagrange equation obtained from minimising the MF DFT in this test particle limit and comparing with the OZ equation, we identify additional terms somewhat akin to a hybrid closure relation and certainly different from the RPA. The additional terms also suggest that the MF DFT, treated in the test particle limit, is much superior to standard OZ with the RPA closure. We argue that this observation should carry through more generally for arbitrary external potentials, not just in the test-particle limit.

Our paper proceeds as follows: In Sec. 6.2 we describe briefly the RPA in the context of the OZ equation. In Sec. 6.3 we describe the MF DFT that generates the RPA and indicate why one might expect this DFT to yield much better results for  $g(r)$ , within the test-particle procedure, than in the standard RPA treatment. In Sec. 6.4 we illustrate and confirm our arguments by presenting results for  $g(x)$  and  $S(k)$  for a model one-dimensional (1D) fluid where the pair correlation functions are known exactly and where the MF DFT can be implemented with the exact reference free energy functional, i.e. that pertaining to hard-rods. Finally, in Sec. 6.5 we discuss the general implications of our results. We also explain that for the same choice of reference system (hard rods) the MF DFT results are identical to those one would obtain from the local molecular field theory (LMF) of Weeks and co-workers [88, 89, 90] for this particular model fluid.

## 6.2 Integral equation approach: OZ equation and RPA

The two-body pair direct correlation function,  $c^{(2)}(r)$ , is usually defined via the OZ equation [9], which for a uniform and isotropic fluid is

$$h(r) = c^{(2)}(r) + \rho_b \int d\mathbf{r}' c^{(2)}(|\mathbf{r} - \mathbf{r}'|)h(r') \quad (6.2.1)$$

where  $h(r)$  is the total correlation function and  $\rho_b$  is the density of the (bulk) fluid. The OZ approach to calculating  $h(r)$  is to split the correlations present in  $h(r)$  into a direct part, which describes the ‘direct’ correlations acting over a range of order that of the interaction pair potential, and an ‘indirect’ part, i.e. the remainder described by the convolution integral. Note that the total correlation function  $h(r) = g(r) - 1$ , where  $g(r)$  is the radial distribution function. Fourier transforming Eq. (6.2.1) yields an algebraic relation:

$$\hat{h}(k) = \frac{\hat{c}(k)}{1 - \rho_b \hat{c}(k)}, \quad (6.2.2)$$

where  $\hat{h}(k)$  and  $\hat{c}(k)$  are the Fourier transforms of  $h(r)$  and  $c^{(2)}(r)$ , respectively.  $\hat{h}(k)$  is closely related to the static structure factor [9]

$$S(k) = 1 + \rho_b \hat{h}(k). \quad (6.2.3)$$

Consider a fluid composed of particles interacting via the pair potential  $v(r)$ . To calculate  $h(r)$  one must supplement the OZ Eq. (6.2.1) with a further, closure relation between  $c^{(2)}(r)$  and  $h(r)$ . The exact closure relation is usually expressed as [9]

$$c^{(2)}(r) = h(r) - \ln(h(r) + 1) - \beta v(r) + B(r) \quad (6.2.4)$$

where  $\beta = (k_B T)^{-1}$ ,  $k_B$  is Boltzmann’s constant,  $T$  is the temperature and  $B(r)$  is termed the bridge function.  $B(r)$  is not known exactly for any 3D fluid. In order to make progress approximations must be made. For example, the hypernetted-chain approximation (HNC) corresponds to  $B(r) = 0$  [9, 86]. Formally  $B(r)$  is the sum of the bridge or elemental diagrams missing in HNC. Suppose  $v(r)$  can be split as follows:

$$v(r) = v_0(r) + v_1(r), \quad (6.2.5)$$

where  $v_0(r)$  is a suitably chosen reference potential, usually the purely repulsive part of  $v(r)$ . Then the remainder  $v_1(r)$  usually incorporates the attractive part of the interaction between particles. The simple closure relation

$$c_{\text{RPA}}^{(2)}(r) \equiv c_0^{(2)}(r) - \beta v_1(r), \quad (6.2.6)$$

where  $c_0^{(2)}(r)$  is the pair direct correlation function for the (purely repulsive) reference system with the same density  $\rho_b$ , defines the RPA. Note that Eq. (6.2.6) enforces the correct asymptotic behaviour:  $c^{(2)}(r) \sim -\beta v(r)$ ,  $r \rightarrow \infty$  for a fluid away from its critical point. Inserting the Fourier transform of (6.2.6) into (6.2.2) yields the standard RPA result for the structure factor [9]:

$$S_{\text{RPA}}(k) = \frac{S_0(k)}{1 + \rho_b \beta \hat{v}_1(k) S_0(k)} \quad (6.2.7)$$

where  $S_0(k)$  is the structure factor of the reference system. The Fourier transform  $\hat{v}_1(k)$  is assumed to exist. Often the further approximation  $c_0^{(2)}(r) \approx c_{\text{HS}}^{(2)}(r)$  is made, where  $c_{\text{HS}}^{(2)}(r)$  is the pair direct correlation function for a hard-sphere (HS) fluid at the same density with suitably chosen effective particle diameter  $\sigma$  [9, 86]. Recall that accurate expressions for the reference  $c_{\text{HS}}^{(2)}(r)$  exist and for a fluid of 1D hard-rods  $c_{\text{HS}}^{(2)}(r)$  is known exactly (see below). The RPA closure relation in Eq. (6.2.6) has been used extensively in the theory of simple and complex liquids [9, 18, 19, 2, 20]. The reliability of the corresponding OZ result for the structure factor (6.2.7) depends on the particular model system and the choice of reference potential.

## 6.3 The mean-field DFT and the RPA

### 6.3.1 The non-uniform fluid

Consider now the fluid composed of particles interacting via the pair potential  $v(r)$ , split as in Eq. (6.2.5) and subject to an external potential  $V(\mathbf{r})$ . The corresponding one-body density is  $\rho(\mathbf{r})$ . Suppose too that we have an accurate DFT for the reference system, indicated by the subscript “0”, i.e. with particles interacting via the potential  $v_0(r)$ . The intrinsic Helmholtz free energy functional can be written as [18]:

$$F[\rho(\mathbf{r})] = F_0[\rho(\mathbf{r})] + \frac{1}{2} \int_0^1 d\lambda \int d\mathbf{r} \int d\mathbf{r}' \rho_\lambda^{(2)}(\mathbf{r}, \mathbf{r}') v_1(|\mathbf{r} - \mathbf{r}'|), \quad (6.3.1)$$

where  $F_0[\rho]$  is the corresponding functional for the reference system. This exact expression is obtained from a thermodynamic integration ‘turning on’ the potential  $v_1(r)$  between the particles via the integration parameter  $\lambda$ . The two-body density distribution function  $\rho_\lambda^{(2)}(\mathbf{r}, \mathbf{r}')$  is that for

the system with interaction potential

$$v_\lambda(r) = v_0(r) + \lambda v_1(r), \quad 0 \leq \lambda \leq 1. \quad (6.3.2)$$

In deriving Eq. (6.3.1) one must impose an external potential, varying with  $\lambda$ , that ensures the equilibrium one-body density remains  $\rho(\mathbf{r})$  at each value of  $\lambda$  [18]. The standard MF DFT approximation is obtained by assuming that (i)  $\rho_\lambda^{(2)}(\mathbf{r}, \mathbf{r}')$  does not change much as  $\lambda$  is varied from 0 to 1 and, more drastically, (ii)

$$\rho_\lambda^{(2)}(\mathbf{r}, \mathbf{r}') \approx \rho(\mathbf{r})\rho(\mathbf{r}'), \quad 0 \leq \lambda \leq 1. \quad (6.3.3)$$

Eq. (6.3.3) clearly constitutes a mean-field treatment of the ‘perturbation’  $\lambda v_1(r)$ . It follows that the MF DFT approximation for the excess (over ideal) free energy functional<sup>1</sup> is:

$$F^{\text{ex}}[\rho(\mathbf{r})] \approx F_0^{\text{ex}}[\rho(\mathbf{r})] + \frac{1}{2} \int d\mathbf{r} \int d\mathbf{r}' \rho(\mathbf{r})\rho(\mathbf{r}')v_1(|\mathbf{r} - \mathbf{r}'|). \quad (6.3.4)$$

Within DFT [19, 18, 9] two functional derivatives of  $-\beta F^{\text{ex}}[\rho]$  with respect to the density yields the pair direct correlation function. From Eq. (6.3.4), and evaluating for a uniform (bulk) fluid  $\rho(\mathbf{r}) = \rho_b$ , we obtain the RPA approximation in Eq. (6.2.6), since

$$c_0^{(2)}(|\mathbf{r} - \mathbf{r}'|) = - \left. \frac{\delta^2 \beta F_0^{\text{ex}}[\rho]}{\delta \rho(\mathbf{r}) \delta \rho(\mathbf{r}')} \right|_{\rho(\mathbf{r})=\rho_b}. \quad (6.3.5)$$

The approximations inherent in Eq. (6.3.3) imply correlations are omitted and so one must be sceptical about the accuracy of the MF functional (6.3.4). Recognising that taking two functional derivatives of (6.3.4) yields the RPA (6.2.6, 6.2.7) for bulk correlation functions provides some useful insight into the status of the MF DFT. It is tempting then to argue that employing the MF DFT (6.3.4) should lead to results with similar accuracy to those obtained from the RPA for bulk liquids. However, this argument is at best misleading. In practical applications of (6.3.4), or any other DFT approximation, one works at the one-body level which requires only a single functional derivative. We explain and illustrate this below within the context of the test particle procedure for calculating  $g(r)$ .

---

<sup>1</sup>The correlations neglected in (6.3.4) are incorporated into the functional  $F_{\text{corr}}[\rho]$  defined in Eq. (3.4.11) of Ref. [9].

### 6.3.2 The Percus test particle procedure

Percus proved [87] that one can determine the radial distribution function  $g(r)$  by calculating the density profile  $\rho(\mathbf{r}) = \rho(r)$  around a fixed particle that exerts an external potential  $V(\mathbf{r}) \equiv v(r)$  on the fluid. Then the radial distribution function  $g(r) = \rho(r)/\rho_b$ . Within DFT,  $\rho(r)$  is obtained by minimising the grand potential functional  $\Omega[\rho] = F[\rho] - \int d\mathbf{r}[\mu - V(\mathbf{r})]\rho(\mathbf{r})$ , where  $\mu$  is the chemical potential. Using (6.3.4), the resulting Euler-Lagrange equation is

$$\frac{\delta\Omega[\rho]}{\delta\rho} = k_B T \ln[\Lambda^3 \rho(r)] + \frac{\delta F_0^{\text{ex}}[\rho]}{\delta\rho} + \int d\mathbf{r}' \rho(r') v_1(|\mathbf{r} - \mathbf{r}'|) + v(r) - \mu = 0, \quad (6.3.6)$$

where  $\Lambda$  is the (irrelevant) thermal de-Broglie wavelength. For  $r \rightarrow \infty$ , away from the fixed test-particle, the density  $\rho(r) \rightarrow \rho_b$ , so within the approximation Eq. (6.3.4) we obtain the following relation between the chemical potential  $\mu$  and the bulk density  $\rho_b$ :

$$\mu = k_B T \ln[\Lambda^3 \rho_b] + \left. \frac{\delta F_0^{\text{ex}}[\rho]}{\delta\rho} \right|_{\rho_b} + \rho_b \int d\mathbf{r} v_1(r). \quad (6.3.7)$$

We make a functional Taylor expansion about the bulk density:

$$\frac{\delta F_0^{\text{ex}}[\rho]}{\delta\rho} = \left. \frac{\delta F_0^{\text{ex}}[\rho]}{\delta\rho} \right|_{\rho_b} + \int d\mathbf{r}' (\rho(\mathbf{r}') - \rho_b) \left. \frac{\delta^2 F_0^{\text{ex}}[\rho]}{\delta\rho(\mathbf{r})\delta\rho(\mathbf{r}')} \right|_{\rho_b} + H_0[\rho(\mathbf{r})], \quad (6.3.8)$$

where  $H_0[\rho(\mathbf{r})]$  denotes all higher order terms; these are  $\sim \mathcal{O}([\rho - \rho_b]^2)$  and higher. From Eqs. (6.3.5)–(6.3.8), we obtain:

$$0 = k_B T \ln\left(\frac{\rho(r)}{\rho_b}\right) + \int d\mathbf{r}' (\rho(r') - \rho_b) \left[ -k_B T c_0^{(2)}(|\mathbf{r} - \mathbf{r}'|) + v_1(|\mathbf{r} - \mathbf{r}'|) \right] + H_0[\rho(r)] + v(r), \quad (6.3.9)$$

which eliminates  $\mu$ . Multiplying through by  $-\beta$  and adding  $(\rho(r) - \rho_b)/\rho_b$  to both sides we obtain:

$$\begin{aligned} \frac{(\rho(r) - \rho_b)}{\rho_b} &= \frac{(\rho(r) - \rho_b)}{\rho_b} - \ln\left(\frac{\rho(r)}{\rho_b}\right) - \beta v(r) - \beta H_0[\rho(r)] \\ &\quad + \rho_b \int d\mathbf{r}' \frac{(\rho(r') - \rho_b)}{\rho_b} \left[ c_0^{(2)}(|\mathbf{r} - \mathbf{r}'|) - \beta v_1(|\mathbf{r} - \mathbf{r}'|) \right]. \end{aligned} \quad (6.3.10)$$

This is the equation for the density profile, equivalent to  $g(r)$ , in the test particle treatment of Percus, as determined by the MF DFT in Eq. (6.3.4). If we set  $v_1(r) = 0$ , then we obtain the

following equation for the total correlation function  $h_0(r) = g_0(r) - 1$  of the reference system:

$$h_0(r) = h_0(r) - \ln(h_0(r) + 1) - \beta v_0(r) - \beta H_0[\rho_b g_0(r)] + \rho_b \int d\mathbf{r}' h_0(r') c_0^{(2)}(|\mathbf{r} - \mathbf{r}'|). \quad (6.3.11)$$

Suppose we know the exact functional  $F_0[\rho]$ , and therefore  $c_0^{(2)}(r)$ , then comparison with Eq. (6.2.4) and use of the OZ equation (6.2.1) allows us to identify  $-\beta H_0[\rho_b g_0(r)]$  as the exact bridge-function  $B_0(r)$  of the reference system.

Returning to the full system, we see that Eq. (6.3.10) is an Ornstein-Zernike-like equation [see Eq. (6.2.1)] with the RPA closure (6.2.6) for the pair direct correlation function  $c^{(2)}(r)$  inside the convolution integral, but with a different closure approximation for  $c^{(2)}(r)$  [see Eq. (6.2.4)] appearing outside. Specifically, the sum of the first four terms on the right-hand side of (6.3.10) correspond formally to the exact expression for  $c^{(2)}(r)$  but with the bridge function  $B(r)$  replaced by  $B_0(r)$ .

The form of Eq. (6.3.10), which follows from the standard MF DFT functional (6.3.4), suggests that calculating the radial distribution function  $g(r)$  via the test-particle route might yield results better than those given by  $g_{\text{RPA}}(r)$ , obtained by solving the OZ equation together with the RPA closure (6.2.6), i.e. by Fourier inverting the RPA structure factor (6.2.7). This is evident for a fluid in which the pair potential  $v(r)$  has a hard-core of diameter  $\sigma$  since solving the Euler-Lagrange equation (6.3.6) guarantees the exact core condition  $\rho(r) = 0$ ,  $r < \sigma$  is satisfied which is, of course, not the case for  $g_{\text{RPA}}(r)$ , given by (6.2.7). In the latter  $g_{\text{RPA}}(r)$  is not identically zero inside the hard-core. We note that the application of any reasonable non-local DFT in the test particle procedure enforces the core condition. There are, of course, other theories that enforce the hard-core condition on  $g(r)$ . The well-known Mean-Spherical Approximation (MSA) [9, 91] enforces this and sets  $c^{(2)}(r) = -\beta v(r)$  outside the core. Perhaps more pertinent to our present discussion is the Optimised RPA (ORPA)[9, 92]. The ORPA invokes the RPA closure (6.2.6) but, in addition, seeks to vary the perturbation potential  $v_1(r)$  inside the hard core, where this is not uniquely defined, so that  $g(r) = 0$ . This constraint is equivalent to requiring the functional derivative of the RPA free energy with respect to  $v_1(r)$  to be zero inside the hard core. In our present approach, there is no attempt to minimise the free energy with respect to the perturbation potential, so for  $r > \sigma$ ,  $g(r)$  depends weakly on the choice of  $v_1(r)$  inside the core. There is no reason to expect the MF DFT to perform as well as the ORPA – at least for a Lennard-Jones type fluid at high densities where

the ORPA is known to be very accurate [9, 92].

For completeness, we also mention the Reference HNC (RHNC), see e.g. Ref. [9], which improves upon the HNC integral equation by approximating the bridge function by that of a reference system, usually hard-spheres. Although the integral equation (6.3.10) that emerges from our MF DFT shares a feature of the RHNC, in that  $B(r)$  is replaced by  $B_0(r)$ , this is implemented only in one part of the right hand side. There is no reason to expect the MF DFT to be as accurate as the RHNC.

This observation concerning the test-particle procedure has repercussions for more general external potentials  $V(\mathbf{r})$ . Solving the corresponding Euler-Lagrange equation, based on the seemingly crude MF functional (6.3.4), yields equilibrium density profiles  $\rho(\mathbf{r})$  that are often very accurate – see Refs. [18, 9] and references therein. Investigation of hard/impenetrable potentials is once again illuminating. For a planar hard wall, with  $V(z) = \infty$  for  $z < 0$ , the density profile satisfies  $\rho(z) = 0$ ,  $z < 0$ . Moreover, for a sensible choice of a (non-local) DFT for the reference system the profile will satisfy [18] the wall contact sum-rule:  $\beta\rho(0^+) = p(\rho_b)$ . The right hand side is the pressure of the bulk fluid, far from the hard wall, obtained from the bulk free energy  $F[\rho_b]$  with  $\rho_b = \rho(\infty)$ .

In the following Sec. 6.4 we compare the results for  $g_{\text{RPA}}(x)$  and  $S_{\text{RPA}}(k)$  (6.2.7) with those obtained from standard MF DFT (6.3.4), implemented within the Percus test particle prescription for a 1D fluid. The reference system is the hard-rod fluid for which the free energy functional is known exactly, and therefore its correlation functions and thermodynamics. Moreover, the pair correlation functions and the thermodynamics of the full system for uniform (bulk) densities are also known exactly. By considering this model fluid we can make a stringent examination of some of the basic approximations employed in classical DFT.

## 6.4 Illustrative results for a 1D fluid

In order to illustrate and support the observations made above, we consider a system of 1D hard-particles (rods on a line) with an additional attractive interaction between pairs of neighbouring rods. As mentioned above, this 1D system is chosen because we know the ingredients of the theory exactly and can therefore test carefully the accuracy of the various approximations. For a fluid of 1D rods with only nearest neighbour interactions  $v(x)$ , one finds the following exact expression for

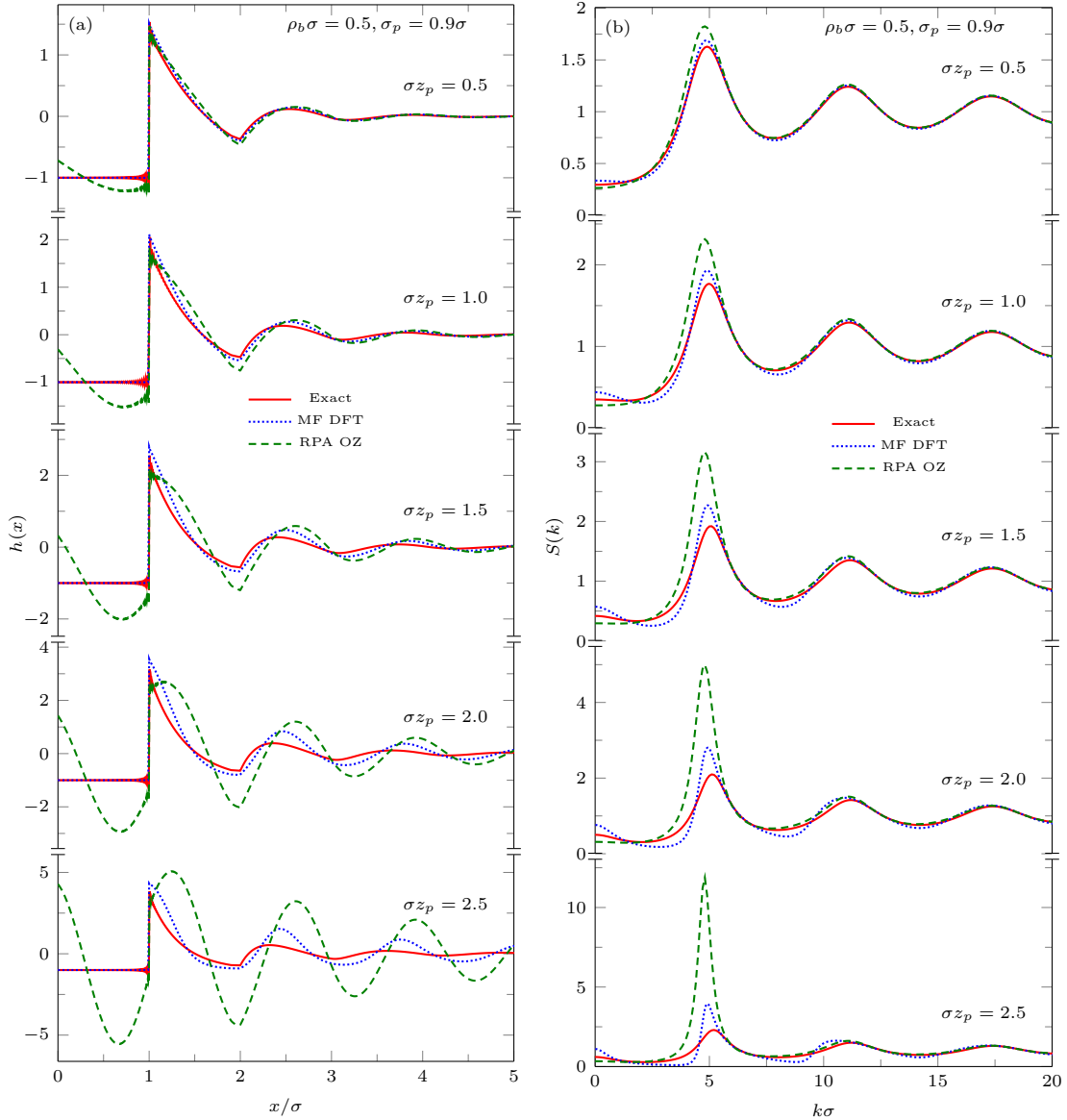


Figure 6.1: (a) The total correlation function  $h(x)$  and (b) the static structure factor  $S(k)$  for hard-rods with an attractive tail potential (6.4.3) for various values of the attraction strength  $z_p$  with fixed  $\sigma_p = 0.9\sigma$  and  $\rho_b\sigma = 0.5$ . We compare the exact results (solid line) with  $g_{\text{RPA}}(x) - 1$  and  $S_{\text{RPA}}(k)$  from the RPA closure (6.2.7) to the OZ equation (dashed) and with those from the MF DFT (6.3.4) using the test particle route (dotted). Note the different scales on each y-axis.

the structure factor [93]

$$S(k) = \frac{1 - e^{-\beta[\mu(p+ik/\beta) - 2\mu(p) + \mu(p-ik/\beta)]}}{(1 - e^{-\beta[\mu(p+ik/\beta) - \mu(p)]})(1 - e^{-\beta[\mu(p-ik/\beta) - \mu(p)]})} \quad (6.4.1)$$

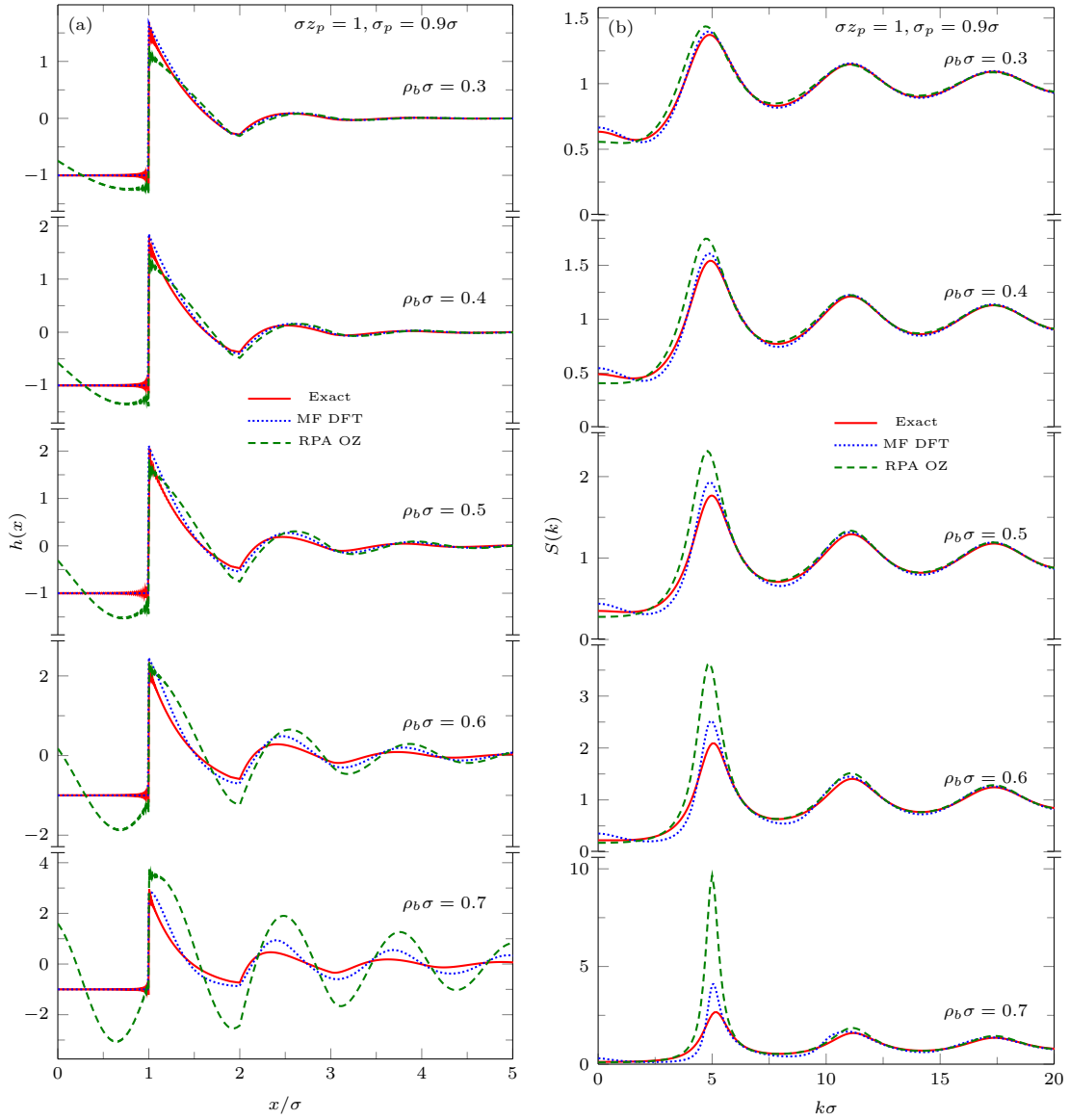


Figure 6.2: (a) The total correlation function  $h(x)$  and (b) the static structure factor  $S(k)$  for hard-rods with an attractive tail potential (6.4.3) for various values of bulk density  $\rho_b$  with fixed  $\sigma z_p = 1$  and  $\sigma_p = 0.9\sigma$ . The key is the same as in Fig. 6.1.

where  $p$  is the pressure and  $\mu(p)$  is the chemical potential which are known exactly [94, 95]. The above equation along with Eqs. (6.2.1) – (6.2.3) can be used to obtain the distribution functions of the uniform 1D system.

We consider 1D rods on a line interacting via the pair potential  $v(x) = v_0(x) + v_1(x)$ , where  $x$  is the distance between the centres of a pair of particles – c.f. Eq. (6.2.5).  $v_0(x)$  is the hard-rod

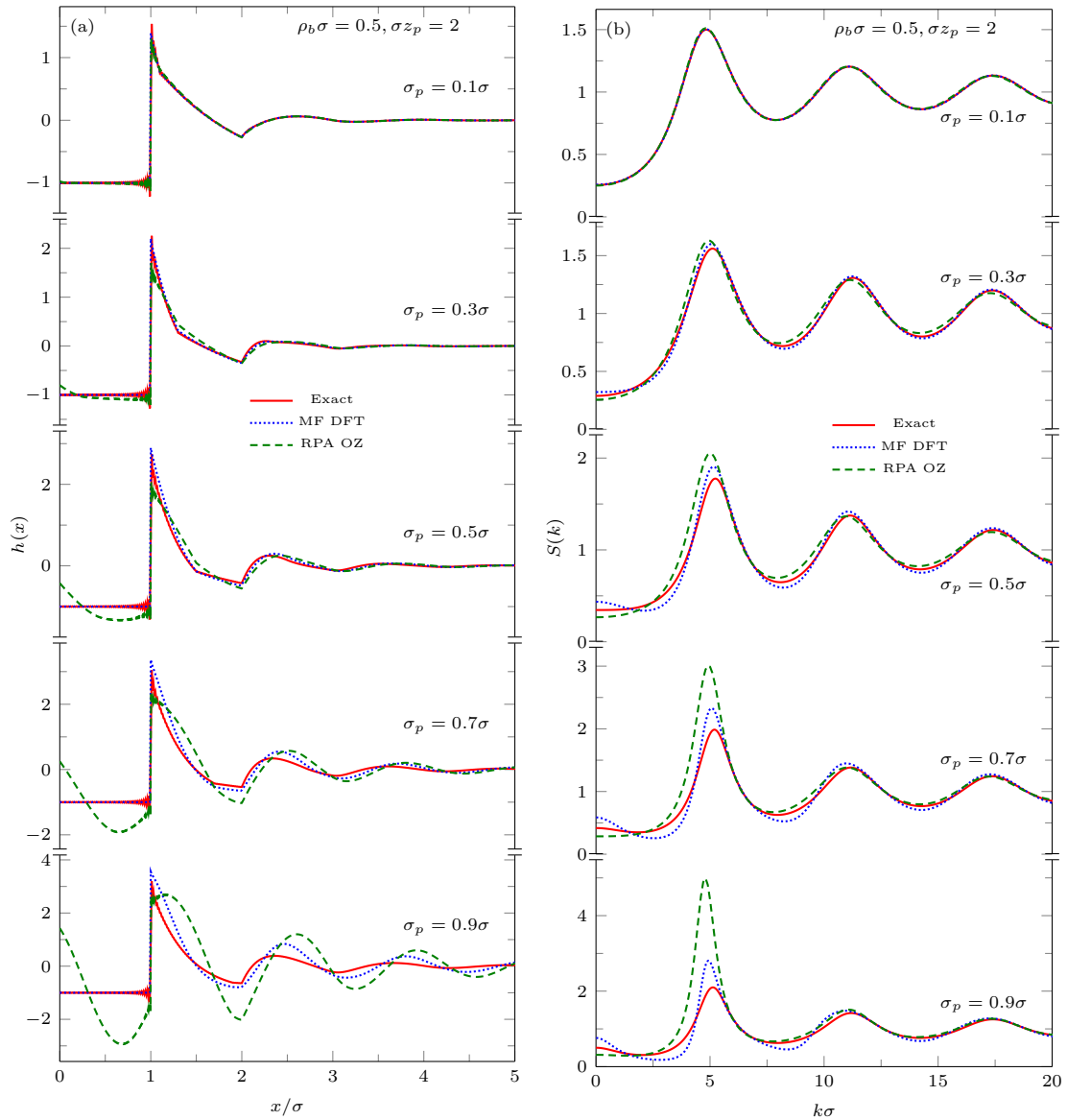


Figure 6.3: (a) The total correlation function  $h(x)$  and (b) the static structure factor  $S(k)$  for hard-rods with an attractive tail potential (6.4.3) for various values of the attraction range  $\sigma_p$  with fixed  $\sigma z_p = 2$  and  $\rho_b \sigma = 0.5$ . The key is the same as in Fig. 6.1.

potential

$$v_0(x) = \begin{cases} \infty & |x| \leq \sigma \\ 0 & |x| > \sigma \end{cases} \quad (6.4.2)$$

and the attractive tail potential (also considered in Ref. [96]) is:

$$\beta v_1(x) = \begin{cases} 0 & |x| \leq \sigma \\ -z_p(\sigma + \sigma_p - |x|) & \sigma < |x| \leq \sigma + \sigma_p \\ 0 & |x| > \sigma + \sigma_p. \end{cases} \quad (6.4.3)$$

The above potential is the 1D analogue of the Asakura-Oosawa potential for the effective colloid-colloid potential of hard-sphere colloids of diameter (length)  $\sigma$  mixed with ideal polymers:  $\sigma_p$  is the ‘length’ of polymer coils and  $z_p$  is the fugacity of ideal polymers [97, 96, 95].

For the hard-rods reference system “0” Percus [98, 93] derived an exact expression for the excess Helmholtz free energy functional

$$F_0^{\text{ex}}[\rho] \equiv F_{\text{HR}}^{\text{ex}}[\rho] = - \int \rho(x) \ln [1 - t(x)] dx, \quad (6.4.4)$$

where the weighted density is

$$t(x) = \int_{x-\sigma}^x \rho(x') dx'. \quad (6.4.5)$$

Taking the functional derivative of (6.4.4) and adding the contribution from the ideal-gas free energy  $F^{\text{id}}[\rho]$ , we obtain

$$\frac{\delta F_0[\rho]}{\delta \rho} = \ln \frac{\Lambda \rho(x)}{1 - t(x)} + \int_x^{x+\sigma} \frac{\rho(x')}{1 - t(x')} dx'. \quad (6.4.6)$$

By differentiating again and using (6.3.5) the exact direct correlation function of a uniform fluid of hard-rods of length  $\sigma$  and density  $\rho_b$  is derived:

$$c_{\text{HR}}^{(2)}(|x - x'|) = -\Theta(\sigma - |x - x'|) \frac{1 - \rho_b |x - x'|}{(1 - \rho_b \sigma)^2}, \quad (6.4.7)$$

where  $\Theta$  is the Heaviside step function. This can be used to construct the RPA approximation (6.2.6) for the 1D system.

Comparison of the exact solution (solid line) with DFT results [calculated using the test particle equation (6.3.6) with (6.4.6) and  $v(x)$  (dotted)] and results for  $g_{\text{RPA}}(x)$  and  $S_{\text{RPA}}(k)$  from the RPA approximation to the OZ equation (6.2.7) with  $v_1(x)$  (dashed), is shown in Figs. 6.1, 6.2 and 6.3.<sup>2</sup>

<sup>2</sup>Note that for  $\lambda = 1$ ,  $S_{\text{MFA}}(k)$ , introduced in Eq. (41) of Ref. [96], is identical to  $S_{\text{RPA}}(k)$  defined here.

In Fig. 6.1 we fix the bulk density  $\rho_b\sigma = 0.5$  and the attraction range  $\sigma_p = 0.9\sigma$  while varying the attraction strength parameter  $z_p$ . In Fig. 6.2 we fix the attraction strength  $\sigma z_p = 1$  and range  $\sigma_p = 0.9\sigma$ , while varying the bulk density  $\rho_b\sigma$ . Finally, in Fig. 6.3 we fix the attraction strength  $\sigma z_p = 2$  and the bulk density  $\rho_b\sigma = 0.5$  while varying the attraction range  $\sigma_p$ .

As expected,  $g_{\text{RPA}}(x)$  fails to satisfy the core condition  $g(x) = 0$  when  $x < \sigma$ , whereas the DFT enforces this. Outside the core of the hard-rod, both the DFT and RPA differ from the exact solution. However, the DFT results for  $g(x)$  are much closer to the exact solution. As we increase the attraction strength or the density, both the DFT and RPA results deviate increasingly from the exact solution.  $g_{\text{RPA}}(x)$  displays only weakly damped oscillations. The same type of pattern is also observed in the sequence of structure factors displayed in Figs. 6.1(b) and 6.2(b). The RPA greatly overestimates the height of the first peak in  $S(k)$  as  $z_p\sigma$  (attractive well-depth) or  $\rho_b\sigma$  are increased. It is important to note that when these parameters are increased beyond the values considered here,  $S_{\text{RPA}}(k)$  diverges at the first peak [96]. Note that for a given choice of pair potential the number density at which the divergence occurs is identical within both the RPA and MF DFT since the linearised form of both theories is identical; only the terms that are non-linear in  $h(x)$  are different. However, the height of the first peak in the structure factor obtained from the MF DFT is always lower and closer to the exact value. It is also noteworthy that both the RPA and MF DFT capture well the behaviour in  $S(k)$  at larger  $k\sigma$ .

The results in Fig. 6.3 show that for fixed attraction strength  $z_p$  both the MF DFT and the RPA become less accurate as the range of the potential  $\sigma_p$  increases. In particular the height of the first peak in  $S(k)$  is overestimated. It appears that the integrated strength of the attraction, measured by the product  $z_p\sigma_p$ , is important in determining under what conditions both approximations are accurate.

## 6.5 Discussion

In order to assess the physical content, and hence the usefulness, of an approximation for the excess free energy functional, it is not sufficient to take two functional derivatives, compute the bulk fluid pair direct correlation function  $c^{(2)}(r)$ , and then enquire how well this quantity performs when used to calculate the pair correlation function  $h(r)$  via the OZ route, Eqs. (6.2.1)-(6.2.3). In most

practical applications of DFT one is concerned with solving the Euler-Lagrange equation for the one-body density profiles and calculating the associated thermodynamic quantities (free energies) that result from minimising a given (approximate) grand potential functional. This requires taking only a single functional derivative—not two. We have illustrated this point of view by focusing on the standard MF DFT, defined by (6.3.4), which treats the attractive part of the inter-particle potential via a simple MF approximation. Working in 1D and computing the density profile induced by a test particle exerting the potential (6.4.2, 6.4.3), we determined  $g(x)$  and  $S(k)$  from the MF DFT. These were compared with the exact results and with those obtained using (6.2.6) with the OZ equation. The latter corresponds to the usual RPA, given by (6.2.7). These results show that the test particle route yields more accurate structure, within a DFT treatment. This not surprising. What is significant is that the MF DFT applied in the test particle situation performs much better for strong inter-particle attraction and for higher densities than the standard RPA. This is evident in Figs. 6.1–6.3.

That it is generally more appropriate to assess the performance of an approximate functional at the one-body rather than at the two-body level is known to the DFT community. The former requires only a single functional derivative with respect to density whereas the latter requires two. Naturally errors build up as further derivatives are taken. Here we are concentrating upon the efficacy of the particular functional (6.3.4). Why might the results, from what appears to be a crude approximation, be much better at the one-body density and free energy level than one might expect? We give three separate arguments: (i) as indicated in Sec. 6.3, the Euler-Lagrange equation (6.3.10) for  $\rho(r)$ , when viewed as an integral equation for  $g(r)$ , implies a more sophisticated closure approximation than the RPA (6.2.6) implemented directly in the OZ equation (6.2.2), which leads to the RPA expression (6.2.7). (ii) Oettel [40] discusses (6.3.4) in the context of a powerful and rather general reference functional approach for constructing approximate free energy functionals. By invoking the assumption that the bridge functional for the full system is well-approximated by that of the reference system and by considering expansions about the bulk density he argues that the reference functional approach predicts roughly MF behaviour for the density deviations (from bulk). He concludes that for adsorption problems, such as wetting and drying, a description based on the MF DFT (6.3.4), with an accurate reference functional  $F_0[\rho]$ , should capture all the essential physical features. Oettel [40] also emphasises that (6.3.4) has the advantage, over the

more sophisticated reference functional approach, of satisfying identically the Gibbs adsorption equation and the wall-contact sum rule. (iii) Weeks and co-workers [88, 89, 90] introduced a local molecular field theory (LMF) that has proved to be highly successful in describing the structure and thermodynamics of a variety of non-uniform liquids. The derivation [89, 99] of the LMF equation for the effective reference field  $\phi_R(\mathbf{r})$  starts with the Yvon-Born-Green equation and uses insightful arguments about the form of the conditional singlet densities  $\rho(\mathbf{r}|\mathbf{r}')$  in the full and reference (mimic) systems. It does not employ concepts from DFT. Although LMF operates at the one-body level, like MF DFT, at first sight there does not appear to be a direct connection between the two approaches. This is not the case. Archer and Evans [96] showed that the LMF equation follows directly from the standard mean-field treatment of attractive interactions as embodied in MF DFT (6.3.4) and if one has access to the exact functional  $F_0[\rho]$  for the same reference system the two theories are equivalent. We note that the derivation of the LMF equation and the relation to DFT is also discussed in the Supporting Information in a recent paper on solvation free energies [100]. In the 1D system described in Sec. 6.4 the free energy functional of the reference (hard-rod) fluid is known exactly; it is given by the Percus result (6.4.4). It follows that our present results for  $g(x)$  obtained using MF DFT and the test particle route are identical to those that would emerge from LMF using hard-rods as the reference system. More generally, in three dimensions, LMF with a hard-sphere reference system would lead to the same  $g(r)$  as MF DFT using the test particle route and a very accurate hard-sphere functional for  $F_0[\rho]$ . Given the success of LMF for a wide variety of fluids, one might argue, albeit circuitously, that the physical arguments and plausible approximations that lead to LMF [89, 99, 100] provide an alternative justification as to why MF DFT might perform better than one might expect. Of course, there is a caveat. The justification for LMF relies upon the judicious choice of reference fluid, described by  $v_0(r)$ , so that the LMF equation used to treat  $v_1(r)$ , the longer ranged part of the pair potential, captures the essential physics for a given model fluid [99, 100]. Although the MF DFT treatment of  $v_1(r)$  is formally equivalent to that of the LMF, the limitation and drawback of the former is finding an accurate free energy functional for the reference fluid [96].

As a final note of caution on assessing the quality of a DFT on the basis of what two derivatives of the free energy functional yields for the (bulk) pair direct correlation function, one should also

recall the following functional:

$$\begin{aligned}
 F^{\text{ex}}[\rho(\mathbf{r})] &\approx F^{\text{ex}}[\rho_b] + \mu_{\text{ex}} \int d\mathbf{r}(\rho(\mathbf{r}) - \rho_b) \\
 &\quad - \frac{1}{2\beta} \int d\mathbf{r} \int d\mathbf{r}' (\rho(\mathbf{r}) - \rho_b)(\rho(\mathbf{r}') - \rho_b)c(|\mathbf{r} - \mathbf{r}'|). \tag{6.5.1}
 \end{aligned}$$

This is the well-known Ramakrishnan-Yousouf functional [101], constructed to yield the ‘exact’ pair direct correlation function,  $c(r) = c_{\text{exact}}^{(2)}(r)$ , with  $c_{\text{exact}}^{(2)}(r)$  calculated at the relevant bulk density  $\rho_b$ . Note that minimising the grand potential corresponding to (6.5.1) within the test particle procedure leads to the HNC closure for the uniform fluid, provided the direct correlation function is determined self-consistently using the OZ equation [18, 9]. However, the functional (6.5.1) has significant weaknesses. For example, it is unable to describe wetting or drying phenomena [18, 102] at substrates nor critical adsorption [103] owing to the fact that it is only quadratic in the density deviation.

## Chapter 7

# Two-Dimensional Colloidal Fluids Exhibiting Pattern Formation

*Fluids with competing short range attraction and long range repulsive interactions between the particles can exhibit a variety of microphase separated structures. We develop a lattice-gas (generalised Ising) model and analyse the phase diagram using Monte Carlo computer simulations and also with density functional theory (DFT). The DFT predictions for the structures formed are in good agreement with the results from the simulations, which occur in the portion of the phase diagram where the theory predicts the uniform fluid to be linearly unstable. However, the mean-field DFT does not correctly describe the transitions between the different morphologies, which the simulations show to be analogous to micelle formation. We determine how the heat capacity varies as the model parameters are changed. There are peaks in the heat capacity at state points where the morphology changes occur. We also map the lattice model onto a continuum DFT that facilitates a simplification of the stability analysis of the uniform fluid.*

### 7.1 Introduction

When the forces between colloidal particles suspended in a liquid are sufficiently strongly attractive, they can exhibit phase separation into a high density colloidal fluid, referred as a colloidal “liquid” and low density suspension, a colloidal “gas” [9]. However, in some circumstances, the interactions can be attractive at short ranges when the particle cores are close to one another, but at longer

ranges be repulsive. These short-range attractive, long-range repulsive (SALR) potentials can arise in certain suspensions of charged colloids and polymers [104] and also in protein solutions [105]. The short range attraction arises from depletion and/or van der Waals attraction and the long range repulsion arises from screened Coulomb interaction. Self-consistent Ornstein-Zernike approximation (SCOZA) integral equation theory for a model of such systems [106, 107], showed that when the long range repulsion is not too strong there is a large region of the phase diagram where the correlations in the fluid show significant fluctuation effects and where the compressibility increases significantly. The SCOZA theory (which is sophisticated and rather accurate) was also compared with results from DFT [108], which showed good agreement between the theories for the liquid structure. When the long range repulsion is further increased, the SALR interaction between the particles gives rise to pattern formation in the fluid state, such as gathering to form clusters, stripes (lamellas) and holes (bubbles), referred to as microphase separation. In Ref. [109] Monte Carlo (MC) computer simulations and integral equation theory was used to understand the details of the relation between the liquid-vapour transition line and the occurrence of any microphase separated phases. As the repulsion strength is increased, starting from the critical point, the gas-liquid phase separation is replaced by microphase separation. In Ref. [110], a study of the cluster formation showed that it is very similar to micelle formation in aqueous surfactant solutions. However, for the system considered in Ref. [111], discontinuities in thermodynamic quantities were observed at the onset of cluster formation, suggesting it is indeed a phase transition.

Further understanding of the phase ordering in SALR systems was recently gained by Pękalski and co-workers [112] by studying a simple one-dimensional lattice model, in which the SALR interaction was modelled using an attractive interaction between neighbouring particles, repulsion between the third neighbours and no interaction between second neighbours or any other neighbours. An exact solution was presented using the transfer matrix method. The same SALR system was then extended to two-dimensions (2D) on a triangular lattice [113, 114], where microphase separated phases and also a reentrant uniform liquid is observed in the phase diagram. This approach, based on using lattice models to elucidate the nature of the structure formation in systems with competing interactions, has a long track record, going back to seminal works, such as Refs. [115, 116]. There are several advantages of using lattice models stemming from the fact that they are much more straightforward to analyse than the equivalent continuum models and also the computations are

much simpler, allowing larger systems to be simulated over longer times. Due to the fact that the clusters and other structures formed can be more than an order of magnitude larger than the size of the individual particles, to properly observe the microphase formation, the system size generally needs to be much larger than that one would use for studying simple gas-liquid systems. There have also been other (field) theoretical and simulation studies considering aspects of the phase behaviour of a variety of fluids interacting via SALR potentials [117, 118, 119, 120].

The more recent interest in SALR systems in 2D stems from the experimental observation of microphase-ordering of nanoparticles at a water-air interface [121, 122], which led to theoretical and simulation work to understand the nature of the structures that are formed. Imperio and Reatto [123, 124, 125] made a detailed study of the phase diagram using parallel-tempering MC simulations to determine the location in the phase diagram of the microphase separated states for a 2D fluid of particles interacting via the double-exponential pair potential

$$u(r) = \begin{cases} \infty, & \text{if } r < \sigma \\ -\frac{\varepsilon_a \sigma^2}{R_a^2} e^{-r/R_a} + \frac{\varepsilon_r \sigma^2}{R_r^2} e^{-r/R_r}, & \text{otherwise} \end{cases} \quad (7.1.1)$$

where  $r$  is the distance between the centres of the particles, which have a hard-core of diameter  $\sigma$ . The short range attraction has strength determined by  $\varepsilon_a$  and range  $R_a$ . Similarly, the repulsion strength is determined by  $\varepsilon_r$  and has range  $R_r$ . When  $R_a = \sigma$ ,  $R_r = 2\sigma$  and  $\varepsilon_a = \varepsilon_r = \varepsilon$ , microphase ordering is observed for temperatures  $k_B T / \varepsilon \lesssim 0.6$ , where  $k_B$  is Boltzmann's constant. At lower densities this takes the form of clusters or "droplets", whilst at higher densities striped structures were observed. At even higher densities a hole phase is observed, although here the simulations can be difficult to perform. Imperio and Reatto [123, 124, 125] showed that at the onset of microphase ordering, one observes a peak in the heat capacity and this was used to identify the location in the phase diagram of the microphase ordered states. Following this, a DFT model for this system was developed [126], which is in good qualitative agreement with simulation results with regard to the topology of the phase diagram and the structure of the fluid and inhomogeneous phases. The DFT also predicts that the transitions from the uniform to the modulated fluid phases are all either first or second order phase transitions [126]. However, the DFT is a mean-field theory and so one should be cautious about accepting this prediction of the theory.

The aim of the work described here is to study the formation of patterns using both MC computer simulations and also DFT for a 2D lattice model in order to determine the nature of the transitions to and between the different microphase ordered structures and also to compare between the methods in order to elucidate what aspects of the microphase ordering the mean-field DFT is able to describe. We fix the strength of the repulsion between the particles to a particular value and we also fix the temperature and then calculate the properties of the fluid as the density and the strength of the attractive interactions between the particles are varied. In particular, we calculate the heat capacity and determine the phase diagram. We also map the lattice model onto a continuum DFT that allows a simple calculation of roughly where in the phase diagram one can expect to find the microphase ordering. This takes the form of a linear stability analysis.

This chapter is laid out as follows: In Sec. 7.2 we define the model fluid and in Sec. 7.3 we present MC computer simulation results, including for the heat capacity, for the ratio of particles in the system within the clusters as the total density in the system is increased and for the static structure factor. In Sec. 7.4 we present the lattice DFT results, comparing with the MC results and calculating the fluid phase diagram. In Sec. 7.5 we map onto a continuum DFT and discuss the linear stability of the fluid. Finally, in Sec. 7.6 we draw our conclusions.

## 7.2 The Model Fluid

We assume that the colloids interact via the pair potential

$$u(r) = \begin{cases} V(r) & r \geq \sigma \\ \infty & r < \sigma, \end{cases} \quad (7.2.1)$$

where  $r$  is the distance between the centres of the two particles and the tail of the potential is given by the double-Yukawa potential [109]

$$V(r) = \begin{cases} -\frac{\varepsilon e^{-z_1(r-\sigma)/\sigma}}{r/\sigma} + \frac{A e^{-z_2(r-\sigma)/\sigma}}{r/\sigma} & r \geq \sigma \\ 0 & r < \sigma \end{cases} \quad (7.2.2)$$

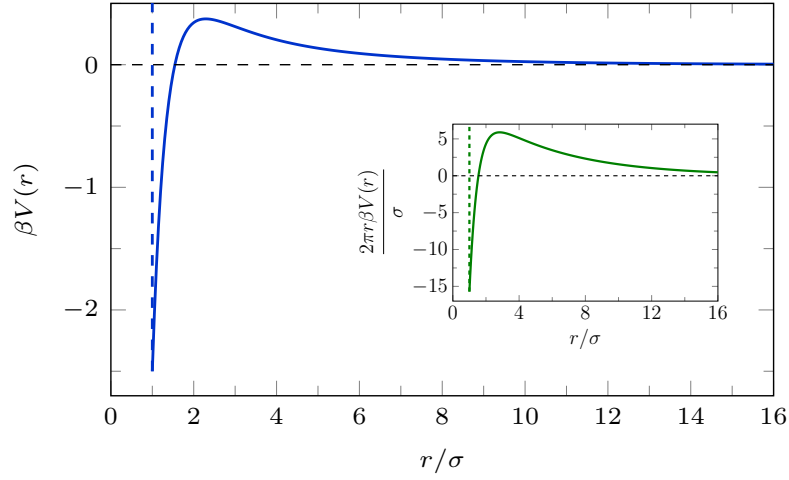


Figure 7.1: The double-Yukawa pair interaction potential between the particles, in the case when the parameters are  $\beta A = 1.5$ ,  $z_1 = 2$ ,  $z_2 = 0.2$  and  $\beta\varepsilon = 4$ . The inset shows the potential multiplied by  $2\pi r$ . This is the integrand in calculating the total contribution. The potential was truncated beyond  $r = r_c = 16\sigma$  because the scaled potential is less than 10% of the maximum value after this point.

where  $\varepsilon$  is the attraction strength coefficient and  $A$  is the repulsion strength coefficient. The parameters  $z_1$  and  $z_2$  determine the range of the attraction and repulsion, respectively.  $\sigma$  is the diameter of the particles, which we set to be our unit of length. We fix the coefficients  $z_1 = 2$  and  $z_2 = 0.2$  so that the potential is of the form illustrated in Fig. 7.1.

In order to simplify the analysis and to reduce the computational costs, we assume that the positions of the particles are discrete variables, and represent the fluid via a 2D lattice model, containing  $M$  lattice sites and with periodic boundary conditions. We use a square lattice of size  $L \times L$ , with lattice spacing equal to the diameter of the particles  $\sigma$  and we assume that each lattice site can be occupied by at most one colloid. We denote a particular configuration of particles by a set of occupation numbers  $\{n_i\}$ , such that, if the site  $i$  is empty, then  $n_i = 0$  and  $n_i = 1$ , if it is occupied. Note that  $i$  here is used as a short form for the position on the 2D lattice, at point  $(j, k)$ . We treat the system in the grand canonical ensemble and so the Hamiltonian of our lattice model can be written as [28]

$$E(\{n_i\}) = \sum_{i=1}^M n_i(\Phi_i - \mu) + \frac{1}{2} \sum_{i,j} V_{i,j} n_i n_j, \quad (7.2.3)$$

where  $\Phi_i$  is the external potential at the lattice site  $i$  and  $\mu$  is the chemical potential which determines

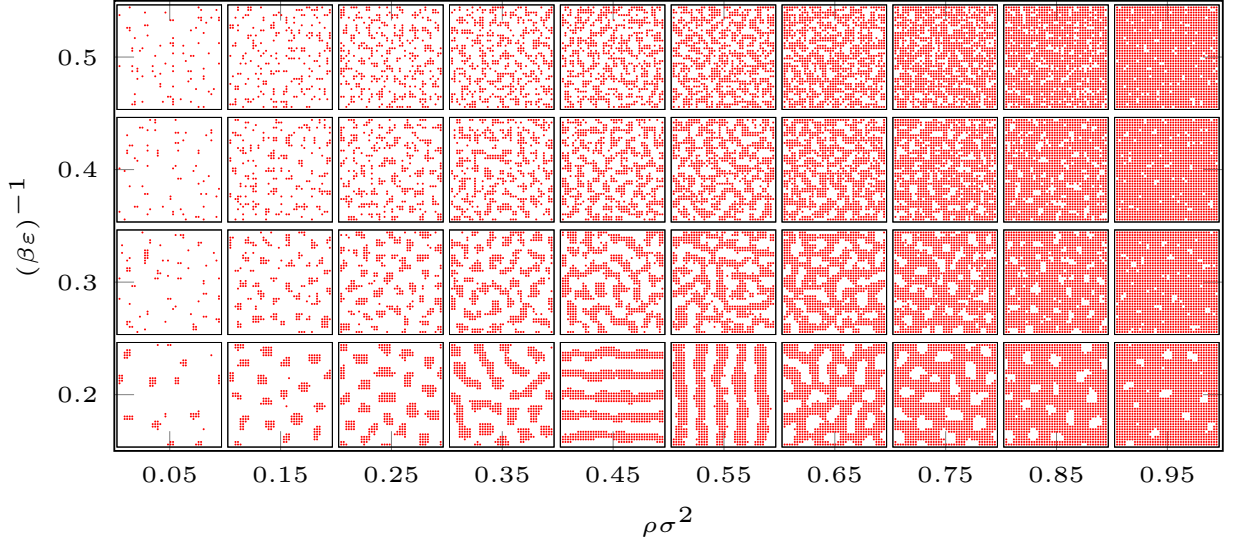


Figure 7.2: Snapshots of typical configurations for a  $40\sigma \times 40\sigma$  size system with  $\beta A = 1.5$ ,  $z_1 = 2$  and  $z_2 = 0.2$ , obtained from grand-canonical MC simulations for various values of the average density and varying values of  $(\beta\varepsilon)^{-1}$ .

the number of particles in the system  $N$ . The final term is the energy contribution due to the interactions between particles, where  $V_{i,j}$  is the pair interaction potential between two particles at sites  $i$  and  $j$ , which is the discrete lattice version of the potential in Eq. (7.2.2), i.e. evaluated by taking  $r$  in Eq. (7.2.2) to be the distance between sites  $i$  and  $j$ . We also assume that there are no three-body or higher-body interactions between the particles. Since here we only consider the ordering in the bulk fluid, we henceforth assume that  $\Phi_i = 0$ ,  $\forall i$ . Also, in all our MC and DFT results below, we truncate the tail of the pair potential beyond  $r = r_c = 16\sigma$ . It is also worth noting that the lattice model Hamiltonian (7.2.3) has a symmetry between particles and holes (i.e. replacing  $n_i \rightarrow 1 - n_i$ ) that, as we show below, results in the phase diagram of the system being symmetric around the density  $\rho = \langle n_i \rangle = 1/2$ .

### 7.3 Monte Carlo

We study the system using standard Metropolis MC simulations [127]. The lattice is initiated in a state where all the sites are randomly occupied by a particle with probability 0.5. At each step during the simulation, a random lattice site  $i$  is selected and we then calculate the change in energy  $\Delta E$  using Eq. (7.2.3) when the occupation number for that lattice site is replaced  $n_i \rightarrow (1 - n_i)$ .

Thus, if the site is already occupied, the trial change is to remove the particle and if the site is unoccupied, the trial move it to insert a particle at that site. If  $\Delta E$  is negative, then we keep the change. Otherwise, we only keep the change with probability,  $e^{-\beta\Delta E}$ .

In Fig. 7.2, we display typical snapshots from our MC simulations for a range of state points, for various average densities  $\rho = \langle N \rangle / M$  (determined by the value of the chemical potential  $\mu$ ) and several values of the inverse attraction strength parameter,  $(\beta\varepsilon)^{-1}$ . At low values of  $(\beta\varepsilon)^{-1}$ , as the average density is increased, the system exhibits a sequence of microphase separated structures. At very low densities, the system forms a gas phase. Increasing  $\rho$ , when the value of  $(\beta\varepsilon)^{-1}$  is low enough, we see the particles are arranged into clusters of a characteristic size. Further increasing  $\rho$ , we observe stripe like patterns for  $\rho\sigma^2 \sim 0.5$ . At even higher densities, we observe a fluid containing ‘bubbles’, again with a characteristic size. Finally, for large  $\rho$ , the system is almost entirely full of particles, forming a dense liquid. Increasing  $(\beta\varepsilon)^{-1}$  leads to the particles becoming less correlated, making it difficult to identify what microphase separation occurs, if any.

### 7.3.1 Heat Capacity

We calculate the heat capacity as the chemical potential  $\mu$  is varied, in order to identify the regions of the phase diagram where the microphase separation occurs. At a phase transition, in the thermodynamic limit, there is normally either a discontinuity or a divergence in the heat capacity. For finite size systems, these show up as peaks in the heat capacity. Recall also that a “bump” in the heat capacity was observed at the onset of microphase ordering in the simulations of Imperio and Reatto [124]. The heat capacity at constant volume can be obtained from the following derivative with respect to temperature [128],

$$C_V = \left( \frac{\partial U}{\partial T} \right)_V, \quad (7.3.1)$$

where the internal energy  $U = \langle E \rangle$ . Alternatively, it can be calculated by measuring the energy fluctuations within the system [16],

$$C_V = \frac{\langle E^2 \rangle - \langle E \rangle^2}{k_B T^2}. \quad (7.3.2)$$

A plot of the heat capacity of a system of size  $40\sigma \times 40\sigma$  as a function of  $\mu$  and for various values

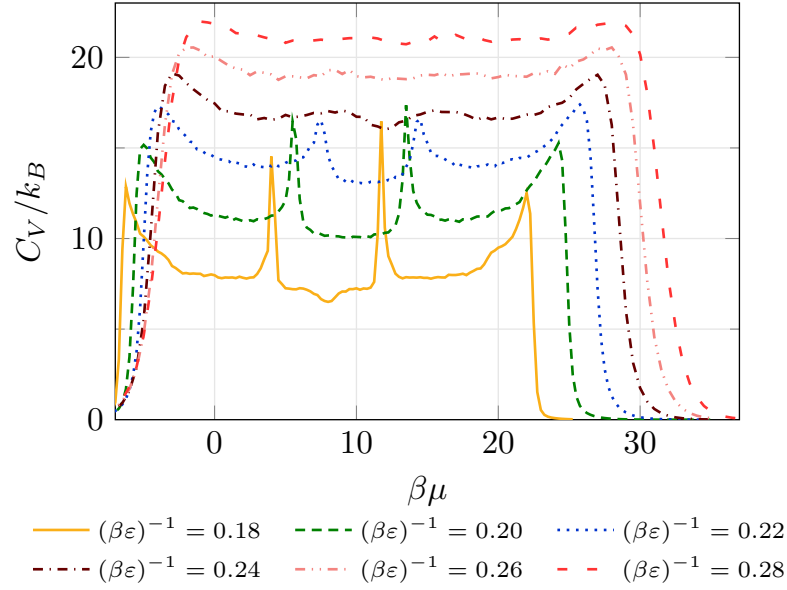


Figure 7.3: Heat capacity versus chemical potential,  $\mu$ , for different values of  $(\beta\varepsilon)^{-1}$ , obtained from Monte Carlo simulations for a  $40\sigma \times 40\sigma$  size system with  $\beta A = 1.5$ ,  $z_1 = 2$  and  $z_2 = 0.2$ .

of  $(\beta\varepsilon)^{-1}$  calculated via Eq. (7.3.2) is shown in Fig. 7.3. The heat capacity tends to zero when the system is completely empty or fully filled. This is as expected, since the system contains hardly any particles to give rise to energy fluctuations at lower values of the chemical potential,  $\mu \rightarrow -\infty$ , and in the opposite limit  $\mu \rightarrow \infty$ , the system is almost completely full of particles, so that the energy of the system,  $E$ , also does not fluctuate much in value.

For higher values of  $(\beta\varepsilon)^{-1}$ , we see in Fig. 7.3 that the heat capacity varies smoothly as  $\mu$  is increased. However, for lower values of  $(\beta\varepsilon)^{-1}$ , we see four clear peaks in the heat capacity. These peaks correspond to changes in the structure of the fluid (see Fig. 7.2). Increasing  $\mu$ , the first peak corresponds to a change from a low density gas to a clustered structure. The second peak corresponds to the change from the cluster to the stripe morphology. The third peak to the change from stripe to bubble and then the final fourth peak to the change from a liquid containing bubbles to a dense liquid without bubbles. As  $(\beta\varepsilon)^{-1}$  is increased, these peaks become smaller in height, eventually being so small that they cannot be identified.

The overall energy fluctuations in the system also get larger as one increases  $(\beta\varepsilon)^{-1}$ . The large (peak) values of the heat capacity  $C_V$  corresponds to state points where there are large fluctuations in the energy of the system. Hence, the peak in  $C_V$  identifies state points where there are multiple

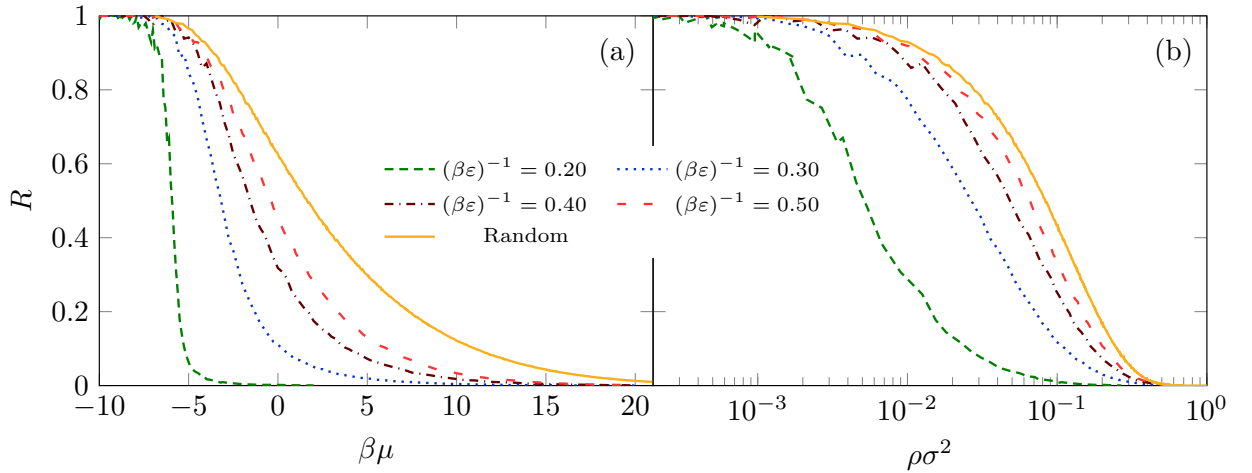


Figure 7.4: Ratio of lone particles in the system,  $R$ , for different values of  $(\beta\varepsilon)^{-1}$ , as a function of: (a) the chemical potential and (b) the average density. The solid line labelled “Random” corresponds to the value of  $R$  for the entirely random uncorrelated configurations that the system with  $\varepsilon = 0$  and  $A = 0$  exhibits. All other results are for the system with  $\beta A = 1.5$ ,  $z_1 = 2$  and  $z_2 = 0.2$ .

types of typical configurations, each with different energy  $E$ .

The presence of these peaks in the heat capacity at state points where the fluid changes morphology naturally leads to the question: are these phase transitions, or just changes in the nature of the fluid correlations? For the low density and high density peak, this question is addressed in the following section.

### 7.3.2 Cluster Formation

To answer the question just posed above: no, the cluster formation is not a phase transition, it is a continuous change analogous to micellisation in surfactants.

Recall that  $N$  is the total number of particles in the system, which changes over time in a grand canonical system. We denote the average total number of particles to be  $\langle N \rangle$ , and  $\langle N_1 \rangle$  be the average number of particles that have no nearest or next nearest neighbours, which we refer to as “lone particles”. We also calculate the ratio of lone particles to the total number of particles,  $R = \langle N_1 \rangle / \langle N \rangle$ , and how this quantity depends on the average density and chemical potential of the system.

In Fig. 7.4, we see that at lower values of chemical potential (i.e. low density), almost all the particles are lone particles and so  $R \approx 1$ . This is because when we have a small overall number

of particles in the system, we are likely to find them all to be alone. As the attraction strength is increased (i.e. as  $(\beta\varepsilon)^{-1}$  is decreased), we see that the drop in value from  $R \approx 1$  for low  $\mu$ , to a value  $R \ll 1$ , becomes much steeper. For example, we see in Fig. 7.4(a) that when  $(\beta\varepsilon)^{-1} = 0.2$ , there is a very sudden drop in the value of  $R$  at  $\beta\mu \approx -5$ . This corresponds to the change in morphology of the system from being mostly full of lone particles to the cluster phase. However, as can be seen in Fig. 7.4(b), where we display the variation of  $R$  with the average density  $\rho$  on a logarithmic scale, we see that actually the change in  $R$  is continuous. The results in Fig. 7.4 were calculated for a  $40\sigma \times 40\sigma$  size system, but these results do not change as the system size is increased (see also section 7.3.3 below).

As we increase  $(\beta\varepsilon)^{-1}$ , we see the ratio of lone particles,  $R$  tends towards the value that one would obtain for a system with  $\varepsilon = 0$  and  $A = 0$ , i.e. where the particles are randomly distributed in the system. This is due to the decrease in particle correlations at higher values of  $(\beta\varepsilon)^{-1}$ , where the structure is essentially that of a highly supercritical fluid. Since the change in the ratio of lone particles is smooth and continuous as we increase the chemical potential (density) of the system, it is clear that the transition that we observe is not a phase transition, instead it is a structural change in the fluid much like micellisation at the critical micelle concentration (CMC) [129].

Micellisation is the spontaneous self assembly of amphiphilic molecules in fluids. The forces that hold the amphiphiles together are generally weak, so that the structure within the micelles is fluid-like. Varying the solvent in which the micelles are suspended changes the interactions and so determines the structure and size of the micelles [129]. The clusters we see are equivalent to spherical micelles, the bubbles are analogous to inverted micelles and the stripes to lamellar bilayer micelles. The similarities between the self-assembly of colloids and amphiphilic molecules have been observed in many experimental, simulation and theoretical studies [109, 120, 124, 104, 130]. Indeed, Ciach and co-workers were able to describe both the SALR colloidal system and amphiphilic systems using the same functional [131], highlighting the many parallels between these systems.

Further support for the above conclusion about the nature of the structural changes in the system can be garnered from noting that the static structure factor  $S(\mathbf{k})$  varies smoothly as  $\mu$  is changed, taking the system from the low density gas state to the cluster morphology.  $S(\mathbf{k})$  is a non-local quantity and so is sensitive to any onset of long range order, in contrast to  $R$ , which characterises

only local (nearest neighbour) ordering. The static structure factor we compute is [9, 123]

$$\begin{aligned} S(\mathbf{k}) &= N^{-1} \langle \rho_{\mathbf{k}} \rho_{-\mathbf{k}} \rangle \\ &= N^{-1} \left\langle \left( \sum_{j=1}^N \cos(\mathbf{k} \cdot \mathbf{r}_j) \right)^2 + \left( \sum_{j=1}^N \sin(\mathbf{k} \cdot \mathbf{r}_j) \right)^2 \right\rangle, \end{aligned} \quad (7.3.3)$$

where  $\rho_{\mathbf{k}} = \sum_{j=1}^N \exp(i\mathbf{k} \cdot \mathbf{r}_j)$ ,  $N$  is the number of particles in the system, and  $\mathbf{r}_j$  is the position on the lattice of each of the particle. In our calculations presented here, we fix the wavevector  $\mathbf{k} = (k, 0)$ .

In Fig. 7.5(a) we display results for  $S(k)$  for a range of state points where the cluster phase is observed, for fixed  $(\beta\varepsilon)^{-1} = 0.18$ . At lower densities (i.e. lower values of the chemical potential  $\mu$ ), the peak in  $S(k)$  is fairly broad with a maximum at  $k\sigma = 0.15\pi \approx 0.47$ , but for higher densities, the peak is sharper, with a maximum at  $k\sigma = 0.2\pi \approx 0.63$ . This is because at the higher densities the cluster phase is formed. When  $(\beta\varepsilon)^{-1} = 0.18$ , the peak in the heat capacity for the gas to cluster transition occurs at  $\beta\mu \approx -6$  [see Fig. 7.3]. Fig. 7.5(b) shows that as  $\mu$  is varied around this value,  $S(k)$  varies smoothly, indicating there is no phase transition. This can also be seen from the plot in Fig. 7.6, where we plot  $S(k)$  for fixed values of  $k$  as the chemical potential  $\mu$  is varied, going from the low density gas state to deep in the region of the phase diagram where the cluster morphology occurs. One further interesting feature of the results in Fig. 7.6 is that in the cluster phase, the value of  $S(k\sigma = \pi/4)$  is almost constant.

We also calculate the histogram of the probability of finding a given instantaneous density  $\rho = N/M$  (not displayed). This has a single peak for all values of the chemical potential  $\beta\mu \approx -6$ , where the heat capacity peak occurs. This is in contrast to the three dimensional system considered in Ref. [109], where a double peaked histogram is observed at the onset of cluster formation.

### 7.3.3 Changing Box Size

Our MC simulations are performed in a finite size box with periodic boundary conditions to approximate an infinite system. However, for some of the transitions, it turns out that the box size is significant in determining the properties of the system. In Fig. 7.7 we plot the heat capacity for  $(\beta\varepsilon)^{-1} = 0.18$ , calculated for simulations in a box of size  $40\sigma \times 40\sigma$  and compare with results for a

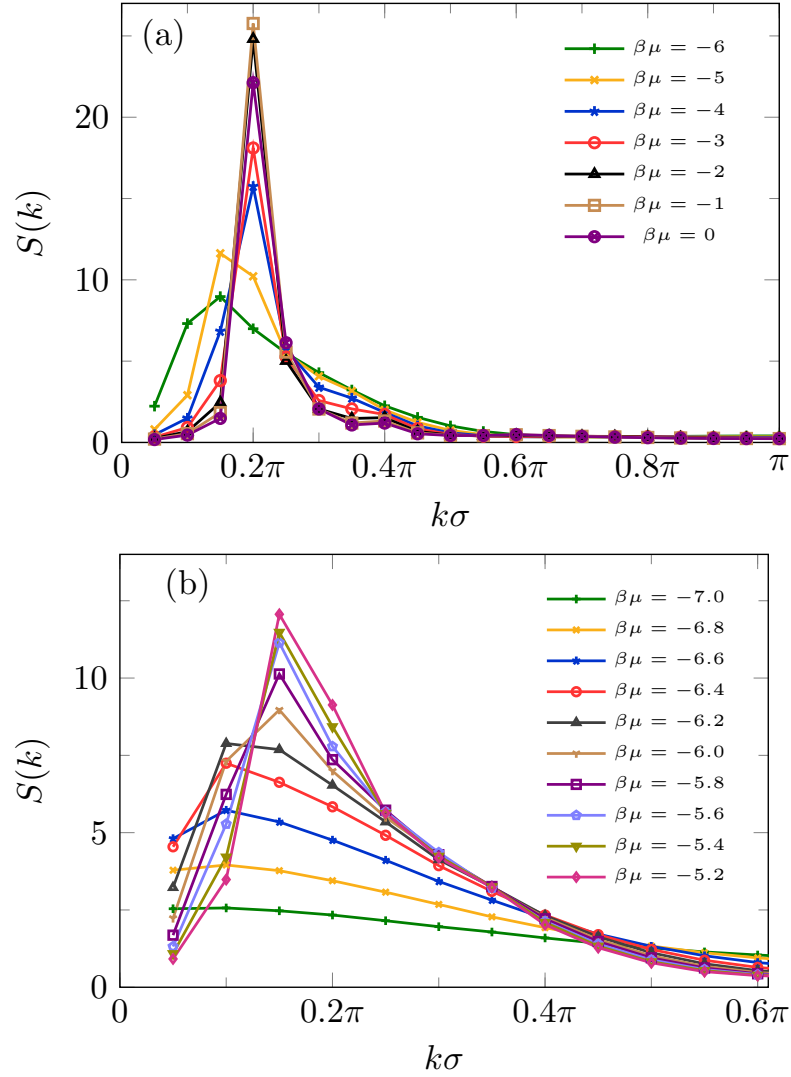


Figure 7.5: In (a) we display the static structure factor  $S(k)$  for fixed  $(\beta\varepsilon)^{-1} = 0.18$  and for a range of different values of the chemical potential  $\mu$  where the cluster morphology is observed. The gas to cluster morphology change occurs at  $\beta\mu \approx -6$ , where there is a peak in the heat capacity (cf. Fig. 7.3). In (b) we display  $S(k)$  over a smaller range of values of  $\mu$ , going from the gas to the cluster morphology. We see that  $S(k)$  varies smoothly as  $\mu$  is varied – see also Fig. 7.6.

larger box of size  $60\sigma \times 60\sigma$ .

In Fig. 7.7, we do not observe any effect of the finite box size on the value of the heat capacity at the peaks corresponding to the gas to cluster transition and also the bubbles to liquid transition. This confirms the conclusion in the previous section that this transition is akin to micellisation, and that there are no discernible effects in the above results due to a finite system size. However, for the heat capacity peaks corresponding to the cluster to stripe and the stripe to bubble transitions,

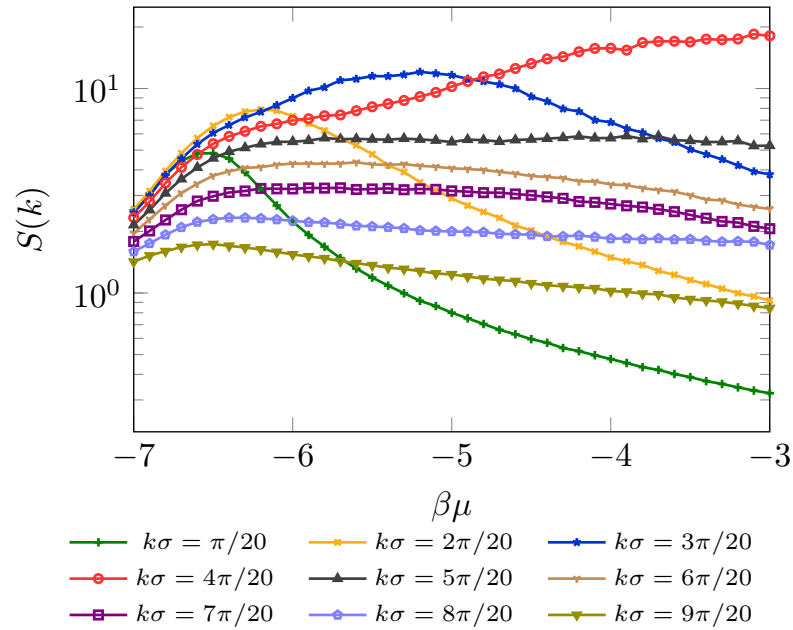


Figure 7.6: The static structure factor  $S(k)$  for a range of different wavevectors  $k$ , as the chemical potential  $\mu$  is varied, for fixed attraction strength  $(\beta\varepsilon)^{-1} = 0.18$ .

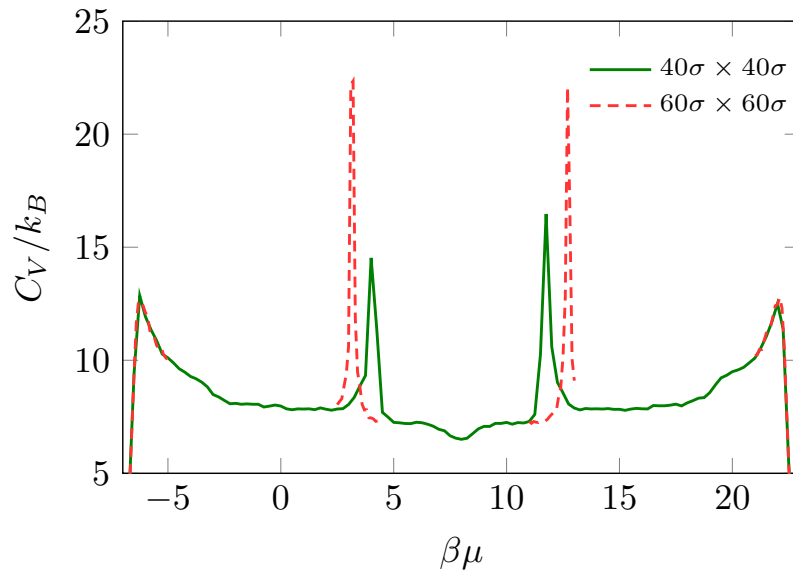


Figure 7.7: The heat capacity versus chemical potential  $\mu$ , for two different box sizes for  $(\beta\varepsilon)^{-1} = 0.18$  [cf. Fig. 7.3].

in Fig. 7.7 we do see significant finite size effects. These peaks shift and become sharper and higher as the system size is increased. This might be seen as indicative that these are second order phase transitions, with a heat capacity divergence in the thermodynamic limit. However, recall that at a

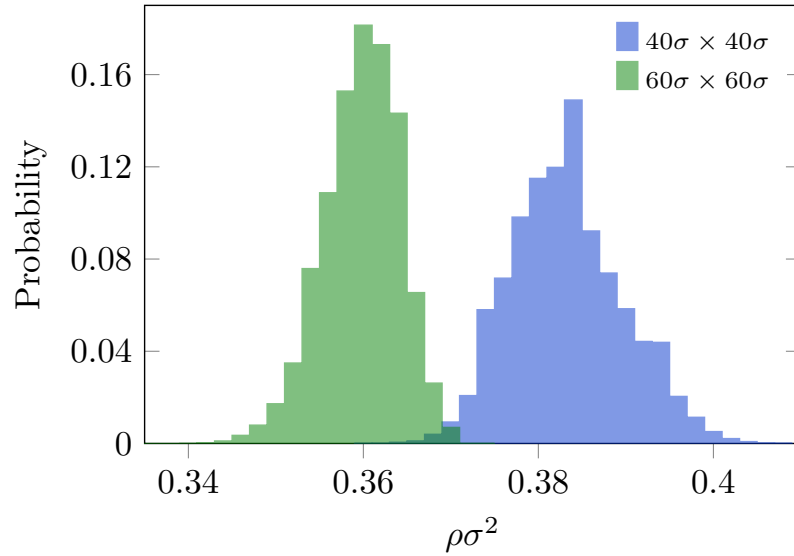


Figure 7.8: Probability of finding a certain instantaneous density  $\rho = N/M$  calculated at the cluster to stripe transition (i.e. at the second peak in the heat capacity) for two different box size for  $(\beta\varepsilon)^{-1} = 0.18$ .

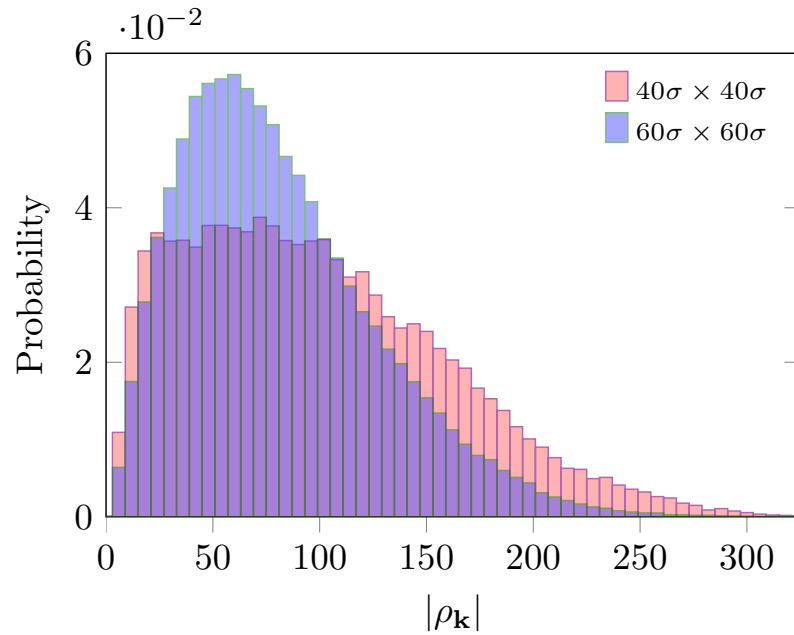


Figure 7.9: Probability distribution for the density Fourier mode amplitude  $|\rho_{\mathbf{k}}|$ , with  $k\sigma = 0.2\pi$ , calculated at the cluster to stripe transition (i.e. at the second peak in the heat capacity) for two different box sizes  $L$  and for  $(\beta\varepsilon)^{-1} = 0.18$ .

phase transition, in a small finite size simulation box the system fluctuates between the two phases.

This leads to a double peak in the density histogram at that state point (or indeed the histogram of

any other quantity that is a suitable order parameter for the transition). However, as can be seen in Fig. 7.8, where we display the density histogram calculated at the value of  $\mu$  corresponding to the peak in the heat capacity, there is a single peak (the corresponding chemical potential values are  $\beta\mu \approx 4.0$  and  $\beta\mu \approx 3.1$  for  $L = 40\sigma$  and  $L = 60\sigma$ , respectively). We obtain very similar distributions for state points either side of where the heat capacity peak occurs. An alternative order parameter that is more sensitive to periodic ordering is the density Fourier mode amplitude,

$$|\rho_{\mathbf{k}}| = \sqrt{\left(\sum_{j=1}^N \cos(\mathbf{k} \cdot \mathbf{r}_j)\right)^2 + \left(\sum_{j=1}^N \sin(\mathbf{k} \cdot \mathbf{r}_j)\right)^2}. \quad (7.3.4)$$

In Fig. 7.9 we display the histogram of  $|\rho_{\mathbf{k}}|$  for the wavevector  $\mathbf{k} = (k_p, 0)$ , where  $k_p\sigma = 0.2\pi$ , which is the value where there is a peak in  $S(k)$ . This order parameter histogram also has a single peak for values of  $\mu$  where the heat capacity exhibits a peak.

From the fact that there is only a single peak in Figs. 7.8 and 7.9, we infer that the transition from the cluster to striped state is simply a change in morphology, much like the micellisation process. We infer the same for the transition from the stripe to the bubble morphology. For low values of  $(\beta\varepsilon)^{-1}$ , we believe that the large heat capacity peak at the transition to the stripe phase and the strong finite-size effects are due to the fact that the stripes that are formed span the simulation box (see Fig. 7.2). The finite size box stabilises the stripes, damping some of the long wavelength fluctuations.

## 7.4 Lattice DFT

We now present results for the structure and thermodynamics of the fluid, which are calculated using density functional theory, and compare with the MC simulation results. The mean-field DFT that we use is a generalisation of the theory presented in Ref. [28] (see also references therein for other applications of the theory). The thermodynamic grand potential is approximated by

$$\Omega = k_B T \sum_{i=1}^M [\rho_i \ln(\rho_i) + (1 - \rho_i) \ln(1 - \rho_i)] + \frac{1}{2} \sum_{i,j} V_{i,j} \rho_i \rho_j + \sum_{i=1}^M (\Phi_i - \mu) \rho_i. \quad (7.4.1)$$

The equilibrium density profile is that which minimises  $\Omega$ , i.e. is the solution of

$$\frac{\partial \Omega}{\partial \rho_i} = 0, \text{ for all } i. \quad (7.4.2)$$

Thus, from Eqs. (7.4.1) and (7.4.2) we obtain

$$\rho_i = (1 - \rho_i) \exp \left[ \beta \left( - \sum_j V_{i,j} \rho_j - \Phi_i + \mu \right) \right]. \quad (7.4.3)$$

This set of coupled equations are solved by Picard iteration [28]. In order to make sure  $\rho_i$  does not fall outside the interval  $(0, 1)$  during the iteration process, we introduce a mixing parameter,  $\alpha$ . The idea is that after each iteration, we mix the new density value with the previous one,

$$\rho_i = \alpha \rho_i^{\text{new}} + (1 - \alpha) \rho_i^{\text{old}}. \quad (7.4.4)$$

The mixing parameter  $\alpha$  typically takes a value in the range  $(0.01, 0.2)$ . Too large a value of  $\alpha$  leads to instabilities in the iteration, whilst if  $\alpha$  is too small, it leads to slow convergence.

### DFT results and comparison with MC

In Fig. 7.10, we display examples of density profiles calculated using the lattice DFT for various values of the attraction strength parameter  $(\beta\varepsilon)^{-1}$ . These are obtained by initiating the Picard iteration with a flat density profile, to which is added a small amplitude random value at each lattice site. The density profiles show the same sequence of structures as observed in Fig. 7.2 from the MC simulation, namely uniform, cluster, stripe (which are not always parallel due to the random initialisation), bubble and uniform as the chemical potential (density) is increased. The agreement between Fig. 7.10 and Fig. 7.2 is rather good. Within the DFT each of these different structures correspond to different solution branches of the grand potential. The global minimum structure for a given state point contains no defects. Thus, in Fig. 7.10 the vast majority of the structures displayed are not global minima of  $\Omega$ . To calculate the phase diagram, we calculate the free energy for defect-free structures, which are obtained by initiating the Picard iteration from profiles with the required structure, rather than from random initial conditions. As  $\mu$  is increased, there are points where these branches cross. At these points the solutions on the different branches have the same

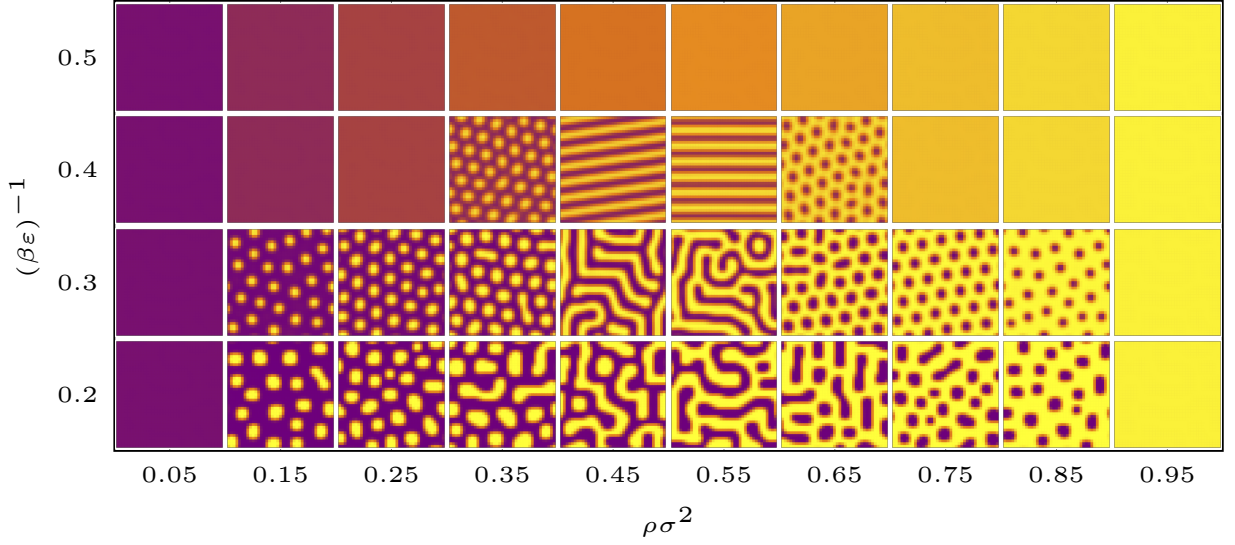


Figure 7.10: A series of density profiles for varying values of  $(\beta\varepsilon)^{-1}$  calculated using the lattice DFT for a  $40\sigma \times 40\sigma$  size system with random initial conditions, for  $\beta A = 1.5$ ,  $z_1 = 2$  and  $z_2 = 0.2$  [cf. Fig. 7.2]. The colours associated with each density value can be deduced from the top row of profiles, which are for  $(\beta\varepsilon)^{-1} = 0.5$ .

$\mu$ ,  $T$  and pressure  $p = -\Omega/V$ , where  $V = M\sigma^2$  is the area of the 2D system. Thus, the (incorrect) prediction from the mean-field DFT is that there are first order phase transitions between all the different structures.

We calculate the lines of thermodynamic coexistence in the phase diagram predicted by the DFT by selecting an initial lattice with a certain microphase separation and then change the chemical potential  $\mu$  and follow that particular branch of solutions. For example, to find the coexistence curve for the gas to cluster transition, we start the DFT iteration with a uniform gas profile and increase  $\mu$  with the new guess being the minimised density profile from the previous value of  $\mu$ . While doing this we record the grand potential  $\Omega$ . Also, we start with an initial density profile corresponding to the cluster structure at a higher value of  $\mu$  and then decrease  $\mu$  following this branch of solutions. Coexistence is found when the pressure, temperature and chemical potential of the two structures are equal. The lines of coexistence define the boundaries in the phase diagram of where the different microphase separated structures occur.

As shown in Fig. 7.11, we see that at the highest values of  $(\beta\varepsilon)^{-1}$  (weak attraction) there is no microphase separation and the system exhibits a single uniform fluid phase. The DFT predicts microphase separation for values of  $(\beta\varepsilon)^{-1} < 0.45$ . For the higher values in this range, e.g.  $(\beta\varepsilon)^{-1} =$

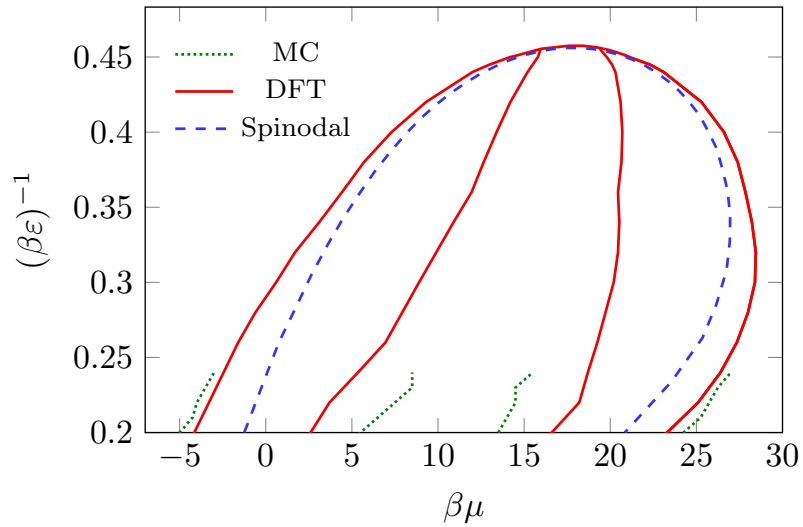


Figure 7.11: Phase diagram showing the instability threshold (spinodal, displayed as the blue dashed line) and the coexistence lines (red solid lines) obtained from DFT for varying values of the chemical potential  $\mu$  and attraction strength  $(\beta\varepsilon)^{-1}$ . The location of the peaks in the heat capacity determined from the MC simulations for a  $40\sigma \times 40\sigma$  system are also shown, as the green dotted line. Note that these lines terminate where the peaks disappear (cf. Fig. 7.2).

0.4, the heat capacity from MC simulations in Fig. 7.3 has no discernible peaks. Nonetheless, comparing Fig. 7.10 and Fig. 7.2, we see that the DFT is correctly predicting the structures formed, it is solely failing to describe the nature of the transition to the modulated structures.

We also see a general shift of the occurrence of microphase ordering to higher values of  $\mu$  as we increase  $(\beta\varepsilon)^{-1}$ . In Fig. 7.11 we also display as green dotted lines the locations of the peaks in the heat capacity, from the MC simulations for a system of size  $40\sigma \times 40\sigma$ . We see that these peaks lie close to the DFT coexistence lines for the gas to cluster transition and also the bubble to liquid transition. However, for the transitions to the stripe state, they are further away. We should emphasise, however, that these are subject to significant finite size effects. For a larger system, these are much closer to the DFT coexistence line.

The linear instability threshold line in Fig. 7.11 is calculated numerically by starting from an initial density profile with the given average value of the density, but with small amplitude random fluctuations. We then determine whether the fluctuations grow over time as we iterate. The boundary of the region where they do grow is referred to as the spinodal in Fig. 7.11. We can also see that the instability line is completely inside the coexistence line. An alternative (but entirely equivalent) way to calculate the spinodal is to determine when the uniform density solution to

Eq. (7.4.1) ceases to be a minimum. Consider a small amplitude harmonic density perturbation of the form

$$\rho_i = \rho + ae^{i\mathbf{k}\cdot\mathbf{r}_i}, \quad (7.4.5)$$

where the amplitude  $a$  is a small parameter,  $\mathbf{r}_i$  is the location of lattice site  $i$  and  $\mathbf{k}$  is any wavevector that is commensurate with the lattice. Substituting Eq. (7.4.5) into Eq. (7.4.1) and then requiring that there is no solution except when  $a = 0$ , is equivalent to the requirement that [see Appendix B]

$$\frac{1}{1-\rho} + \rho\beta V_d(\mathbf{k}) > 0, \quad (7.4.6)$$

where  $V_d(\mathbf{k}) = \sum_j V_{i,j} e^{-i\mathbf{k}\cdot\mathbf{r}_{i,j}}$  is the discrete Fourier sum of the potential, where  $\mathbf{r}_{i,j} = \mathbf{r}_i - \mathbf{r}_j$ . The quantity on the left hand side of Eq. (7.4.6) is equal to  $1/S_{DFT}(\mathbf{k})$ , where  $S_{DFT}(\mathbf{k})$  is the static structure factor predicted by the DFT. Within the spinodal displayed in Fig. 7.11, Eq. (7.4.6) is no longer true for all  $\mathbf{k}$  and thus the uniform density profile is no longer a minimum of the free energy [126].

In Fig. 7.12 we compare how the average density varies with chemical potential in the MC simulations with the results from DFT. We see that the MC simulation results show a smooth increase in the density. However, for sufficiently low values of  $(\beta\varepsilon)^{-1}$ , the DFT gives jumps in the density as we increase  $\mu$ . The jumps are plotted as dots in Fig. 7.12, which corresponds to the values of  $\mu$  where microphase separation occurs. The magnitude of the jumps decreases as we increase  $(\beta\varepsilon)^{-1}$ . The jumps in the DFT occur because of various local minima in the free energy. Hence, the DFT has a tendency to stick to the initial density profile (local minimum) that we start from. Thus, the initial density profile is important for determining if the grand potential minimum that the iteration goes to is actually the global minimum. Different initial density profiles give us different local minima, which also depends on the box size, as expected. The DFT results are closer to the MC simulation results at higher values of  $(\beta\varepsilon)^{-1}$  where there are more fluctuations in the system and the structural changes that occur in the system are smoother.

For example, when  $(\beta\varepsilon)^{-1} = 0.18$  (typical of low values of  $(\beta\varepsilon)^{-1}$ ), the DFT exhibits many discontinuities as we increase the chemical potential. This can be easily noticed in the middle portion of the curve in Fig. 7.12 which corresponds to the stripe region. This is due to discontinuous changes

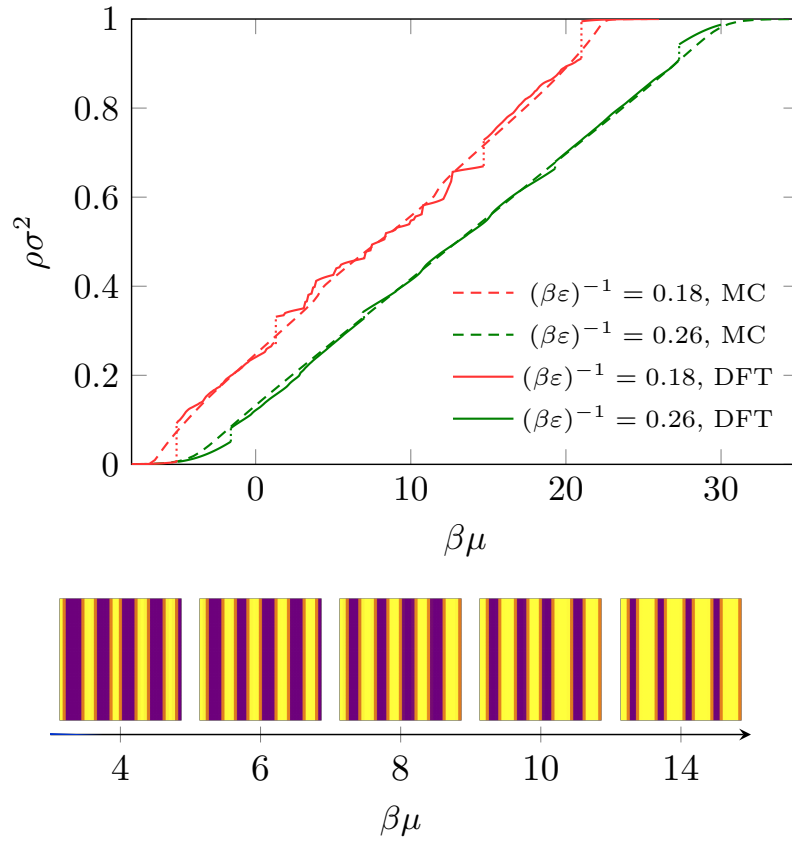


Figure 7.12: Top: a comparison of the average density as a function of  $\mu$  for two different values of  $(\beta\varepsilon)^{-1}$  from the MC simulations (dashed lines) and DFT (solid lines). The dotted line in the DFT curves show the jumps at which the transitions between the different morphologies occurs. Bottom: DFT density profiles showing the discontinuous changes in the stripes as we vary  $\mu$  for fixed  $(\beta\varepsilon)^{-1} = 0.18$ , resulting in the non-smooth curves in the density plot above.

in the width of the stripes that arise as we change the chemical potential. This is illustrated in the lower plots in Fig. 7.12, where we see that the width of individual stripes varies with changing chemical potential - i.e. not all stripes in Fig. 7.12 have the same width. This confirms that the pattern formed is not necessarily the global equilibrium, since we expect the width of all the individual stripes to be identical at a global minimum.

In Fig. 7.11, the phase diagram was plotted as a function of chemical potential  $\mu$ . If we instead plot the value of  $(\beta\varepsilon)^{-1}$  at which the transitions occur as a function of density, we see that in this representation the phase diagram is symmetric around  $\rho\sigma^2 = 0.5$  (see Fig. 7.13). The instability line is fully within the region of the phase diagram where the uniform liquid is metastable. The shaded regions are the regions of coexistence between the two phases. We also see that the density

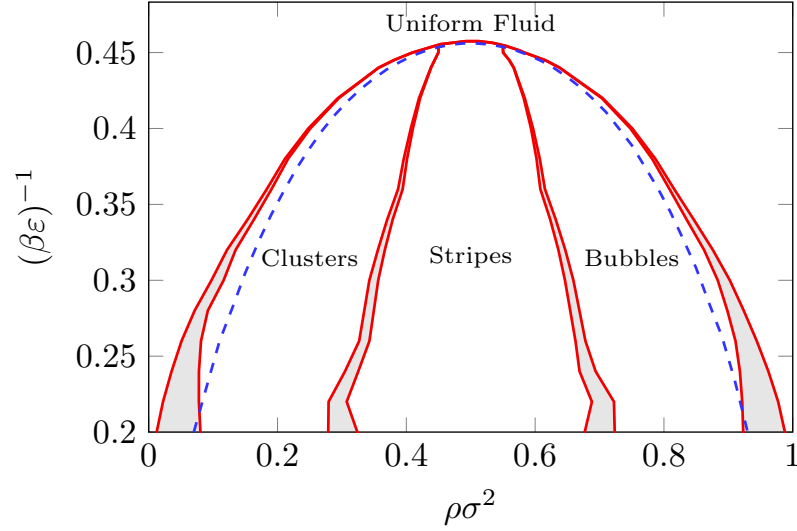


Figure 7.13: Phase diagram showing the instability line (blue) and the coexistence lines (red) from DFT for varying values of the density  $\rho$  and attraction strength  $\varepsilon$ , for fixed  $\beta A = 1.5$ ,  $z_1 = 2$  and  $z_2 = 0.2$ .

range over which there is coexistence decreases as we increase  $(\beta\varepsilon)^{-1}$ .

## 7.5 Continuum DFT approximation

We now approximate the discrete lattice model by treating it with a continuum DFT, that enables a more straightforward calculation of quantities such as the linear instability threshold (spinodal) and other related quantities. This mapping from the lattice to a continuum assumes that the density profile  $\rho_i$  varies slowly enough that we can treat it as a discretised representation of a continuous profile  $\rho(\mathbf{r})$ . This also enables us to convert the sums over lattice sites into integrals. Hence, the Helmholtz free energy  $F = \Omega + \mu\langle N \rangle$  [cf. Eq. (7.4.1)], can be written as the following functional:

$$F = \int f(\rho(\mathbf{r})) \, d\mathbf{r} + \frac{1}{2} \iint \rho(\mathbf{r})\rho(\mathbf{r}')V(|\mathbf{r} - \mathbf{r}'|) \, d\mathbf{r} \, d\mathbf{r}' + \int \rho(\mathbf{r})\Phi(\mathbf{r}) \, d\mathbf{r} \quad (7.5.1)$$

where  $V(r)$  is the pair potential in Eq. (7.2.2),  $\Phi(\mathbf{r})$  is the external potential and  $f$  is a local free energy per unit area given by

$$f(\rho) = k_B T [\rho \ln(\rho) + (1 - \rho) \ln(1 - \rho)] - \frac{\chi}{2} \rho^2. \quad (7.5.2)$$

The first term is the free energy for a non-interacting ( $\varepsilon = A = 0$ ) lattice gas. The second term involving the parameter  $\chi$  is a term to correct for the effect of the mapping from the lattice to the continuum, so that the continuum model gives the same free energy for the uniform fluid as the lattice model. The parameter  $\chi$  is the following integrated difference between the continuum pair potential and the lattice potential:

$$\chi = 2\pi \int_{\sigma}^{r_c} rV(r) dr - \sum_{\langle i,j \rangle} V_{i,j}. \quad (7.5.3)$$

The reason for mapping to a continuum model is that the following linear stability analysis is made somewhat more simple. The aim of the linear stability analysis is to determine where in the phase diagram the uniform fluid state becomes unstable, i.e. we locate the region of the phase diagram in which the microphase ordering occurs.

Consider a uniform fluid with density  $\rho_0$ . We wish to know whether any small amplitude density modulation will grow over time (fluid is unstable) or whether the amplitude will decrease (fluid is stable). Specifically we consider a density fluctuation of the form [cf. Eq. 7.4.5]

$$\begin{aligned} \rho &= \rho_0 + \delta\rho(\mathbf{r}, t) \\ &= \rho_0 + \xi e^{i\mathbf{k}\cdot\mathbf{r} + \omega t}, \end{aligned} \quad (7.5.4)$$

where  $\xi$  is the initial amplitude of the sinusoidal perturbation that has wavenumber  $\mathbf{k}$ . The growth/decay rate of this mode is given by the dispersion relation  $\omega = \omega(k)$ , where  $k = |\mathbf{k}|$  [132].

To determine the time evolution of this non-equilibrium density profile, we require a theory for the dynamics of the colloids. This is supplied by dynamical density functional theory (DDFT), which shows that for Brownian colloidal particles the time evolution of  $\rho(\mathbf{r}, t)$  is governed by [133, 132, 9]

$$\frac{\partial \rho}{\partial t} = D \nabla \cdot \left[ \rho \nabla \frac{\delta \beta F}{\delta \rho} \right], \quad (7.5.5)$$

where  $D$  is the diffusion coefficient of the colloids. Note that for an equilibrium fluid, the chemical potential [19, 18, 9]

$$\mu = \frac{\delta F}{\delta \rho} \quad (7.5.6)$$

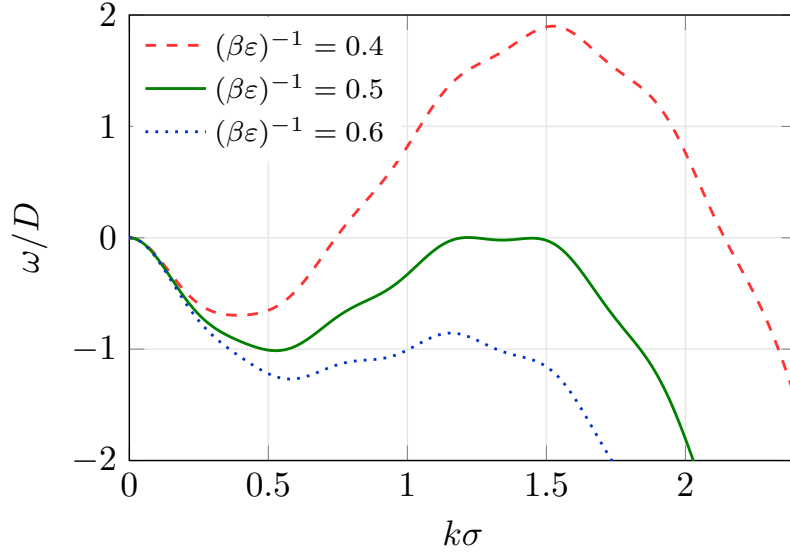


Figure 7.14: The dispersion relation (7.5.7) for varying attraction strength  $\varepsilon$ , for the uniform fluid with density  $\rho\sigma^2 = 0.5$ , for fixed  $\beta A = 1.5$ ,  $z_1 = 2$  and  $z_2 = 0.2$ .

is a constant. Thus, in Eq. (7.5.5), it is gradients in the chemical potential of the non-equilibrium fluid that drives the dynamics. Substituting Eq. (7.5.4) into Eq. (7.5.5) together with Eq. (7.5.1) with the external potential  $\Phi = 0$ , and then linearising in  $\delta\rho$ , we obtain the following expression for the dispersion relation [132] [cf. Eq. (7.4.6)]

$$\omega = -Dk^2 \left( \frac{1}{1 - \rho_0} - \beta\chi\rho_0 + \beta\rho_0\hat{V}(k) \right), \quad (7.5.7)$$

where  $\hat{V}(k)$  is the 2D Fourier Transform of the pair potential

$$\hat{V}(k) = 2\pi \int_0^\infty rV(r)J_0(kr) dr, \quad (7.5.8)$$

where  $J_0(x)$  is the Bessel function of order 0. In Fig. 7.14 we display the dispersion relation for the uniform fluid with density  $\rho\sigma^2 = 0.5$ , for various values of  $\varepsilon$ .

From the dispersion relation, we can find the linear instability threshold line. Since we know that the system becomes unstable when  $\omega > 0$ , the instability line (threshold between stable and unstable region) can be calculated for values of  $\varepsilon$  and  $\rho_0$  when the maximum of  $\omega(k)$  is zero; i.e.

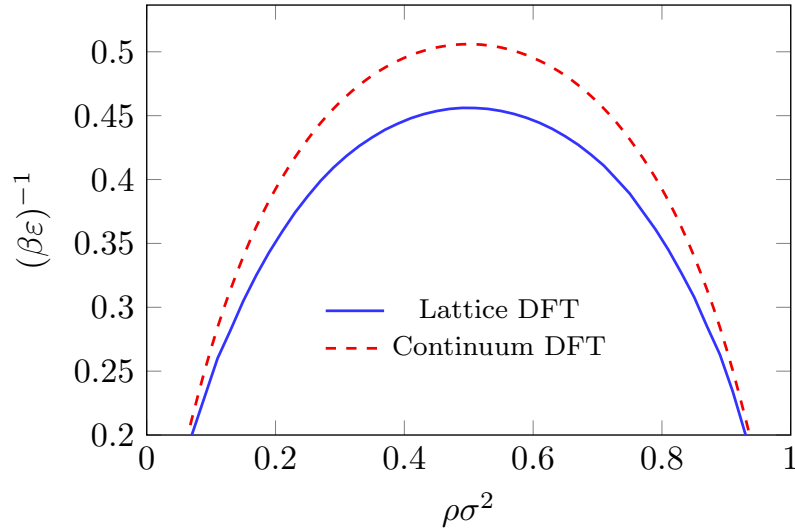


Figure 7.15: Phase diagram showing the linear instability threshold line for the lattice DFT (blue solid line) and also the instability line for the continuum DFT (red dashed line), calculated from dispersion relation in Eq. (7.5.7).

the locus of

$$\left. \frac{d\omega(k)}{dk} \right|_{k=k_c} = 0 \quad \text{and} \quad \omega(k_c) = 0, \quad (7.5.9)$$

where  $k_c$  is the value at which  $\omega(k)$  is maximum. The linear instability line is thus easily obtained from the dispersion relation and is displayed in Fig. 7.15. In this figure, we also display the linear instability line for the original lattice DFT model, obtained as described in Appendix B.

Comparing the two instability lines in Fig. 7.15 shows that the maximum value of  $(\beta\epsilon)^{-1}$  where the system is linearly unstable is predicted to be a little higher in the continuum theory, compared to the lattice model. Comparing with Fig. 7.2 and Fig. 7.10, we see that this simple calculation does indeed identify the region of the phase diagram where microphase separation is observed. Of course, it does not specify which structures (cluster, stripe or bubble) are formed, but it does allow one to narrow down to the relevant region of the phase diagram.

We find the above analysis rather instructive: mapping from a lattice to continuum theory or vice-versa is a “trick” that is often performed to aid the analysis of a system. This procedure is clearly an approximation, but the fact that the two curves in Fig. 7.15 are reasonably close to one another gives confidence that in the present situation the mapping is justified.

## 7.6 Conclusion

In this chapter we have studied a lattice model for 2D colloidal fluids where the colloids have attractive interactions at short separations, but repel at longer range. We model this by using a double-Yukawa pair potential between the particles. This SALR system self assembles to form different microphase separated structures. Using MC computer simulations and by calculating the heat capacity of the system as the chemical potential  $\mu$  and the attraction strength coefficient  $\varepsilon$  are varied, we determine where in the phase diagram the different morphology changes occur. At lower values of  $(\beta\varepsilon)^{-1}$ , the heat capacity exhibits peaks at the transitions between the different structures. The height of the peaks decrease as we increased  $(\beta\varepsilon)^{-1}$ , eventually disappearing. The peak at the transition from the gas to the cluster state and also for the bubble to liquid shows no system size dependence for systems greater than or equal to  $40\sigma \times 40\sigma$  in size. However, the peaks for the transitions to the stripe phase do change with system size, for the system sizes we were able to consider. By calculating how the number of lone particles and the static structure factor varies through the transition between the gas and the cluster phase, we conclude that this transition is a structural transition entirely akin to micellisation. The transition from the cluster to the stripe phase is very similar, except here occurring on a larger scale, by the gathering together of clusters to form stripes. This behaviour is also observed in living polymerisation, where a peak in the heat capacity is also observed [134, 135, 136].

Due to the fact that the pair potential (7.2.1) between the particles is fairly long ranged, the MC simulations can be computationally expensive. Recall that we cut-off our slowly decaying potential at a range of  $r_c = 16\sigma$ , which is much longer ranged than the potentials considered e.g. in Refs. [112, 113, 114, 115, 116]. We only implemented the simple Metropolis MC algorithm, so correctly sampling for system sizes greater than  $60\sigma \times 60\sigma$  and for many state points was not feasible. To simulate efficiently for larger systems, a more sophisticated MC incorporating e.g. cluster moves is required. This simple MC also limited what temperatures (i.e. values of  $(\beta\varepsilon)^{-1}$ ) we could go down to. For  $(\beta\varepsilon)^{-1} = 0.18$  we are confident that our MC simulations are correctly sampling the system. However, for lower temperatures, the algorithm struggles to sample a representative set of states in the time available. The low temperature properties of the model are interesting as it may be the case that at very low temperatures the structural transitions we observe become genuine phase

transitions. It is certainly the case that other lattice models with competing interactions [113, 114, 115, 116] do exhibit phase transitions at low temperatures. We leave investigating this aspect to future work.

We also used a simple lattice DFT to calculate density profiles for the system. Comparing Figs. 7.2 and 7.10, the agreement between simulation and the mean-field DFT is rather good. The pair potential (7.2.1), with the parameter values that we use, is fairly long ranged and slowly varying – see Fig. 7.1. In the case of purely attractive systems, when the pair potentials are long ranged and slowly varying (the classic mean-field situation) then one would not be surprised to find that mean-field DFT is accurate. However, given that the present system exhibits microphase ordering and is strongly fluctuating, it was not a-priori clear that the agreement between the DFT and the MC is as good as it is.

We also used the DFT to calculate the phase diagram and found that the heat capacity peaks in the MC simulations are close to the transition lines predicted by the DFT for the gas to cluster transition and the bubble to liquid transition. For the cluster to stripe and stripe to bubble transitions, they are somewhat further away. One aspect of the DFT is that at lower values of  $(\beta\varepsilon)^{-1}$ , the model exhibits many local free energy minima. This means that to use the DFT to calculate the phase diagram one needs to ensure one has a good choice of initial density profile. Starting from a density profile that is not good approximation, the iteration can go to a local minimum with a free energy value above that of the global minimum. Such behaviour is often observed in pattern forming systems. Thus, great care is required to determine the system sizes in which the system arranges in a state that is close in free energy value to the global minimum value.

Mapping the lattice model onto a continuum DFT yields a theory from which determining the linear instability threshold line using the dispersion relation is straightforward, enabling us to easily and rapidly determine the range of parameter values where the microphase ordering occurs. This provides a useful starting point if future analysis of the behaviour of systems with different pair potential parameter values is required.

## Chapter 8

# Final Remarks

We conclude by summarising the relevant results from the main chapters in this thesis. We also discuss the scope for further study and the limitations of the approaches used in our investigations.

In chapter 5, we studied the effect of solvophobic, solvophilic and patchy blocks immersed in a simple LJ like solvent. All the calculations were done using continuum DFT. We looked at the density profiles and local compressibility in the vicinity of various blocks and found that when the blocks are solvophobic (or have solvophobic patches) next to each other, the solvent is expelled akin to capillary evaporation when the solvent is near to coexistence. When the blocks have solvophilic patches, we see strong density oscillations due to the packing of the solvent particles. We noticed that the local compressibility had a maxima in the region of liquid-gas interface, with the maxima for the solvophilic blocks being considerably smaller than in the solvophobic case. Also, we calculated the solvent mediated interaction potential between the blocks and found that when the blocks are both solvophobic and parallel to each other, the solvent mediated potential has a roughly linear part. For blocks that are solvophilic the solvent mediated potential has oscillations in it. This structure was evident with the patchy blocks as well. Moreover, we were able to approximate the solvent mediated potential using macroscopic thermodynamics and the resulting formula matches quite well with the microscopic DFT. However, to derive such an approximation for the blocks at an angle, we need to take into account the shape of the interface.

While the model considered in chapter 5 is rather simple, it provides hints concerning the magnitude of the solvation force that will arise upon immersing complex molecules in a solvent. This is especially important in the context of solvent mediated protein-protein interactions, where

the areas of proteins (patches) with different affinity towards the water solvent molecules give rise to an important contribution to the free energy of the protein dimer formation and our results gives an estimate of how large these effects are. We considered a simple model fluid and learned a great deal. However, it would be good to repeat the exercise with a realistic model for water (cf. Ref. [42]) and also more realistic substrates and model proteins.

The pattern formation in a two-dimensional lattice model with competing attractive and repulsive interactions (double-Yukawa pair potential between the particles) was studied in chapter 7. A lattice model was studied both via Monte Carlo simulations and by DFT. Using MC we calculated the heat capacity of the system as the chemical potential and the attraction between the particles were varied. We found that the peaks in the heat capacity correspond to the changes in the morphology of the system. With further investigation, such as finding the structure factor, we were able to conclude that the microphase formation is likely a crossover phenomenon, akin to micellisation in surfactant systems (this behaviour is also observed in living polymerisation). Using DFT for the same parameters, we found that the agreement between simulation and the mean-field DFT was rather good. However, the mean field approximation meant that DFT incorrectly predicts the morphological changes as first order phase transitions.

There were many limitations in both the MC and the DFT used. The system size for the MC was limited because the interactions between particles is fairly long ranged, so the MC simulations can be computationally expensive. To simulate efficiently for large systems, a more sophisticated MC incorporating e.g. cluster moves is required – recall we used just the simple Metropolis MC algorithm in our simulations. With the DFT, the initial density profile approximation has a big impact on what the final density profile is like. The main reason is due to the iteration becoming stuck in the local minima. A further study of the underlying (free) energy landscape would be illuminating, e.g. statistics of the depth and how free energy minima are connected and how the minima vary as the system size is increased. Further, one should explore other related pair potentials and lattices in order to study the structures described in Ref. [137]. Recently, Almarza and co-workers [138] studied the effects of confinement on pattern formation in two dimensional systems with competing interactions on a triangular lattice. One could extend this by considering the effect of fluid next to blocks (instead of two planar walls) like we did in chapter 5.

Throughout the thesis we used a simple mean-field approximate DFT in most of our calculations

---

and in chapter 6 we used the so-called test-particle limit to calculate the fluid density profile around a fixed particle. The comparison of the results with the exact bulk fluid correlation functions and those from the OZ equation with the RPA closure showed that one should not necessarily judge the quality of an approximate DFT based on what it generates from taking two functional derivatives, since the DFT results are much better than those from RPA OZ. This work gives reassurance about the reliability and usefulness of the mean-field DFT used extensively here and in many other studies.

## Appendix A

# Solvent Mediated Potential for Two Identical (Asymptotic) Planar Walls

For planar walls separated by distance  $L$ , the asymptotic decay,  $L \rightarrow \infty$ , of the excess grand potential per unit area  $W(L)$  is known [78, 79] for various choices of the fluid-fluid and wall-fluid potentials and is given by

$$\beta W(L) \sim \beta u_{00}(L) + \frac{2\rho B L^{1-p}}{p-1} - \frac{2\pi\rho^2 A L^{4-n}}{(n-2)(n-3)(n-4)}, \quad L \rightarrow \infty, \quad (\text{A.0.1})$$

where  $u_{00}$  is the direct wall-wall interaction potential per unit area and  $\rho$  is the fluid density. The potentials are defined by

$$\beta v(r) \sim -A r^{-n}, \quad r \rightarrow \infty; \quad n > 3 \quad (\text{fluid-fluid}) \quad (\text{A.0.2})$$

$$\beta \phi(z) \sim -B z^{-p}, \quad z \rightarrow \infty \quad (\text{wall-fluid}). \quad (\text{A.0.3})$$

For our choice [Eqs. (5.2.2) and (5.3.7)], we have

$$n = 6 \quad \text{and} \quad A = \beta 4 \varepsilon \sigma^6 \quad (\text{A.0.4})$$

$$p = 3 \quad \text{and} \quad B = \beta \frac{2\pi}{3} \varepsilon_{wf} (\rho_w \sigma^3) \sigma^3. \quad (\text{A.0.5})$$

Thus Eq. (A.0.1) becomes

$$\beta W(L) \sim \beta u_{00}(L) + L^{-2} \left[ \frac{2\pi}{3} \beta \varepsilon_{wf}(\rho_w \sigma^3)(\rho \sigma^3) - \frac{\pi}{3} \beta \varepsilon (\rho \sigma^3)^2 \right]. \quad (\text{A.0.6})$$

At  $T/T_c = 0.8$ , we have  $\beta \varepsilon \approx 0.828$  and when  $\beta \Delta \mu = 0.01$ , we have  $\rho \sigma^3 \approx 0.589$ . Also, for the solvophilic wall, we set  $\beta \varepsilon_{wf} = 1$ . Substituting all this into the above equation yields

$$\beta W(L) \sim \beta u_{00}(L) + 0.933 L^{-2}, \quad L \rightarrow \infty, \quad (\text{A.0.7})$$

i.e. the solvent mediated force per unit area  $-(\partial W/\partial L)_{T,\mu}$  is positive (repulsive) and decays  $\sim L^{-3}$ .

## Appendix B

# Linear Stability (Spinodal) Calculation for Lattice DFT

The thermodynamic grand potential in lattice model is approximated by

$$\Omega = k_B T \sum_{i=1}^M [\rho_i \ln(\rho_i) + (1 - \rho_i) \ln(1 - \rho_i)] + \frac{1}{2} \sum_{i,j} V_{i,j} \rho_i \rho_j + \sum_{i=1}^M (\Phi_i - \mu) \rho_i. \quad (\text{B.0.1})$$

The equilibrium density profile is that which minimises  $\Omega$ , i.e. is the solution of

$$\frac{\partial \Omega}{\partial \rho_i} = 0, \text{ for all } i. \quad (\text{B.0.2})$$

Thus, by differentiating Eq. (B.0.1) and imposing the minimum condition (B.0.2) we obtain

$$\ln \rho_i - \ln(1 - \rho_i) + \sum_j \beta V_{i,j} \rho_j + \beta \Phi_i - \beta \mu = 0. \quad (\text{B.0.3})$$

In our calculation the external potential  $\Phi_i = 0$  and the chemical potential is related to the bulk density as follows

$$\beta \mu = \ln \left( \frac{\rho_b}{1 - \rho_b} \right) + \rho_b \sum_j \beta V_{i,j}. \quad (\text{B.0.4})$$

Consider a small amplitude harmonic density perturbation of the form

$$\rho_i = \rho_b + \delta \rho_i = \rho_b + a e^{i\mathbf{k} \cdot \mathbf{r}_i} \quad (\text{B.0.5})$$

where the amplitude  $a$  is a small parameter,  $\rho_i$  is the density at lattice site  $i$  and  $\mathbf{k}$  is any wavevector that is commensurate with the lattice. Using Taylor expansion for  $\ln \rho_i - \ln(1 - \rho_i)$  around  $\rho_b$  we have

$$\ln \rho_i - \ln(1 - \rho_i) = \ln \left( \frac{\rho_b}{1 - \rho_b} \right) + \left( \frac{1}{\rho_i} + \frac{1}{1 - \rho_i} \right) \delta \rho_i + \mathcal{O}(\delta \rho_i^2). \quad (\text{B.0.6})$$

Therefore, substituting Eq. (B.0.5) into Eq. (B.0.3) and using the above equation we have

$$\ln \left( \frac{\rho_b}{1 - \rho_b} \right) + \left( \frac{1}{\rho_b(1 - \rho_b)} \right) \delta \rho_i + \rho_b \sum_j \beta V_{i,j} + \sum_j \beta V_{i,j} \delta \rho_j + \mathcal{O}(\delta \rho_i^2) = \beta \mu, \quad (\text{B.0.7})$$

which reduces to

$$\begin{aligned} & \left( \frac{1}{\rho_b(1 - \rho_b)} \right) \delta \rho_i + \sum_j \beta V_{i,j} \delta \rho_j + \mathcal{O}(\delta \rho_i^2) \\ &= a \left( \frac{1}{\rho_b(1 - \rho_b)} \right) e^{i\mathbf{k} \cdot \mathbf{r}_i} + a \sum_j \beta V_{i,j} e^{i\mathbf{k} \cdot \mathbf{r}_j} + \mathcal{O}(\delta \rho_i^2) \\ &= a \left( \frac{1}{\rho_b(1 - \rho_b)} \right) e^{i\mathbf{k} \cdot \mathbf{r}_i} + a \sum_j \beta V_{i,j} e^{i\mathbf{k} \cdot (\mathbf{r}_j - \mathbf{r}_i)} e^{i\mathbf{k} \cdot \mathbf{r}_i} + \mathcal{O}(\delta \rho_i^2) \\ &= a \left( \frac{1}{\rho_b(1 - \rho_b)} \right) e^{i\mathbf{k} \cdot \mathbf{r}_i} + a \sum_j \beta V_{i,j} e^{i\mathbf{k} \cdot (\mathbf{r}_j - \mathbf{r}_i)} e^{i\mathbf{k} \cdot \mathbf{r}_i} + \mathcal{O}(\delta \rho_i^2) \\ &= \left( \frac{1}{\rho_b(1 - \rho_b)} + \sum_j \beta V_{i,j} e^{i\mathbf{k} \cdot (\mathbf{r}_j - \mathbf{r}_i)} \right) a e^{i\mathbf{k} \cdot \mathbf{r}_i} + \mathcal{O}(\delta \rho_i^2) \\ &= \frac{1}{\rho_b} \left( \frac{1}{1 - \rho_b} + \rho_b \sum_j \beta V_{i,j} e^{-i\mathbf{k} \cdot \mathbf{r}_{i,j}} \right) a e^{i\mathbf{k} \cdot \mathbf{r}_i} + \mathcal{O}(\delta \rho_i^2) = 0. \end{aligned} \quad (\text{B.0.8})$$

In the above calculation,  $\mathbf{r}_{i,j} = \mathbf{r}_i - \mathbf{r}_j$ . The formula inside the brackets is equal to reciprocal of static structure factor predicted by the DFT,  $S_{DFT}$ . Hence,

$$1/S_{DFT}(\mathbf{k}) = \frac{1}{1 - \rho_b} + \rho_b \sum_j \beta V_{i,j} e^{-i\mathbf{k} \cdot \mathbf{r}_{i,j}} = \frac{1}{1 - \rho_b} + \rho_b \beta V_d(\mathbf{k}) \quad (\text{B.0.9})$$

where,  $V_d(\mathbf{k})$  is the discrete Fourier sum of the potential. Therefore, we have the requirement that

$$1/S_{DFT}(\mathbf{k}) > 0, \quad (\text{B.0.10})$$

for there to be no solution except when  $a = 0$  for Eq. (B.0.8). Thus, when Eq. (B.0.10) is true, the uniform system is linearly stable. The locus in parameter space when Eq. (B.0.10) is no longer true corresponds to the linear instability threshold plotted in Fig. 7.15.

# Bibliography

- [1] T. Mammoto and D. E. Ingber, “Mechanical control of tissue and organ development,” *Development*, vol. 137, no. 9, pp. 1407–1420, 2010.
- [2] C. N. Likos, “Effective interactions in soft condensed matter physics,” *Physics Reports*, vol. 348, no. 4, pp. 267–439, 2001.
- [3] M. Dine and M. C. Gutzwiller, “Has particle physics fulfilled its promise?,” *Physics Today*, vol. 48, no. 2, pp. 13–15, 1995.
- [4] L. Boltzmann, “The second law of thermodynamics,” in *Theoretical physics and philosophical problems*, pp. 13–32, Springer, 1974.
- [5] J. D. Van Der Waals and J. S. Rowlinson, *On the continuity of the gaseous and liquid states*. Courier Corporation, 2004.
- [6] P. Egelstaff, *An introduction to the liquid state*. Elsevier, 2012.
- [7] C. A. Croxton, *Introduction to liquid state physics*. Wiley, 1975.
- [8] J. S. Rowlinson and F. L. Swinton, *Liquids and liquid mixtures: Butterworths monographs in chemistry*. Butterworth-Heinemann, 2013.
- [9] J.-P. Hansen and I. R. McDonald, *Theory of Simple Liquids: With Applications to Soft Matter*. Academic Press, 2013.
- [10] H. Gould and J. Tobochnik, *Statistical and thermal physics: with computer applications*. Princeton University Press, 2010.
- [11] P. Curty and H. Beck, “Thermodynamics and phase diagram of high temperature superconductors,” *Physical review letters*, vol. 91, no. 25, p. 257002, 2003.
- [12] N. A. Peppas, Y. Huang, M. Torres-Lugo, J. H. Ward, and J. Zhang, “Physicochemical foundations and structural design of hydrogels in medicine and biology,” *Annual review of biomedical engineering*, vol. 2, no. 1, pp. 9–29, 2000.
- [13] J. E. Moyal, “Quantum mechanics as a statistical theory,” in *Mathematical Proceedings of the Cambridge Philosophical Society*, vol. 45, pp. 99–124, Cambridge Univ Press, 1949.

- [14] M. Plischke and B. Bergersen, *Equilibrium Statistical Physics*. World Scientific Publishing Co Inc, 2006.
- [15] V. I. Kalikmanov, *Statistical physics of fluids: basic concepts and applications*. Springer, Berlin, 2001.
- [16] D. Chandler, *Introduction to modern statistical mechanics*. Oxford University Press, 1987.
- [17] S. R. A. Salinas, *Introduction to statistical physics*. Springer, 2001.
- [18] R. Evans, “Density functionals in the theory of nonuniform fluids,” in *Fundamentals of Inhomogeneous Fluids* (D. Henderson, ed.), ch. 3, pp. 85–176, New York: Marcel Dekker, 1992.
- [19] R. Evans, “The nature of the liquid-vapour interface and other topics in the statistical mechanics of non-uniform, classical fluids,” *Adv. Phys.*, vol. 28, no. 2, pp. 143–200, 1979.
- [20] H. Löwen, “Density functional theory of inhomogeneous classical fluids: recent developments and new perspectives,” *J. Phys.: Condens. Matter*, vol. 14, no. 46, p. 11897, 2002.
- [21] J. F. Lutsko, “Recent developments in classical density functional theory,” *Adv. Chem. Phys.*, vol. 144, p. 1, 2010.
- [22] N. D. Mermin, “Thermal properties of the inhomogeneous electron gas,” *Phys. Rev.*, vol. 137, no. 5A, p. A1441, 1965.
- [23] R. Roth, “Fundamental measure theory for hard-sphere mixtures: a review,” *J. Phys.: Condens. Matter*, vol. 22, no. 6, p. 063102, 2010.
- [24] W. A. Curtin and N. W. Ashcroft, “Weighted-density-functional theory of inhomogeneous liquids and the freezing transition,” *Phys. Rev. A*, vol. 32, no. 5, p. 2909, 1985.
- [25] Y. Rosenfeld, “Free-energy model for the inhomogeneous hard-sphere fluid mixture and density-functional theory of freezing,” *Phys. Rev. Lett.*, vol. 63, no. 9, p. 980, 1989.
- [26] F. H. Stillinger, “Structure in aqueous solutions of nonpolar solutes from the standpoint of scaled-particle theory,” in *The Physical Chemistry of Aqueous System*, pp. 43–60, Springer, 1973.
- [27] R. Roth, R. Evans, A. Lang, and G. Kahl, “Fundamental measure theory for hard-sphere mixtures revisited: the white bear version,” *J. Phys.: Condens. Matter*, vol. 14, no. 46, p. 12063, 2002.
- [28] A. P. Hughes, U. Thiele, and A. J. Archer, “An introduction to inhomogeneous liquids, density functional theory, and the wetting transition,” *Am. J. Phys.*, vol. 82, no. 12, pp. 1119–1129, 2014.

- [29] R. Evans and U. M. B. Marconi, "Phase equilibria and solvation forces for fluids confined between parallel walls," *J. Chem. Phys.*, vol. 86, no. 12, pp. 7138–7148, 1987.
- [30] P. Tarazona and R. Evans, "Long ranged correlations at a solid-fluid interface a signature of the approach to complete wetting," *Mol. Phys.*, vol. 47, no. 5, pp. 1033–1063, 1982.
- [31] R. Evans and A. O. Parry, "Wetting transitions in fluids with short-ranged forces: correlation functions and criticality," *J. Phys.: Condens. Matter*, vol. 1, no. 39, p. 7207, 1989.
- [32] M. C. Stewart and R. Evans, "Critical drying at a spherical substrate," *J. Phys.: Condens. Matter*, vol. 17, no. 45, p. S3499, 2005.
- [33] T. Young, "An essay on the cohesion of fluids," *Philosophical Transactions of the Royal Society of London*, vol. 95, pp. 65–87, 1805.
- [34] K. Binder, "Theory of first-order phase transitions," *Rep. Prog. Phys.*, vol. 50, no. 7, p. 783, 1987.
- [35] E. V. Albano and K. Binder, "Finite-size scaling approach for critical wetting: Rationalization in terms of a bulk transition with an order parameter exponent equal to zero," *Phys. Rev. Lett.*, vol. 109, no. 3, p. 036101, 2012.
- [36] P. Bryk and K. Binder, "Non-mean-field behavior of critical wetting transition for short-range forces," *Phys. Rev. E*, vol. 88, no. 3, p. 030401, 2013.
- [37] D. Bonn, J. Eggers, J. Indekeu, J. Meunier, and E. Rolley, "Wetting and spreading," *Rev. Mod. Phys.*, vol. 81, no. 2, p. 739, 2009.
- [38] J. T. Simpson, S. R. Hunter, and T. Aytug, "Superhydrophobic materials and coatings: a review," *Rep. Prog. Phys.*, vol. 78, no. 8, p. 086501, 2015.
- [39] J. R. Henderson and F. van Swol, "On the approach to complete wetting by gas at a liquid-wall interface: Exact sum rules, fluctuation theory and the verification by computer simulation of the presence of long-range pair correlations at the wall," *Mol. Phys.*, vol. 56, no. 6, pp. 1313–1356, 1985.
- [40] M. Oettel, "Integral equations for simple fluids in a general reference functional approach," *J. Phys.: Condens. Matter*, vol. 17, no. 3, p. 429, 2005.
- [41] R. Evans and N. B. Wilding, "Quantifying density fluctuations in water at a hydrophobic surface: evidence for critical drying," *Phys. Rev. Lett.*, vol. 115, no. 1, p. 016103, 2015.
- [42] R. Evans, M. C. Stewart, and N. B. Wilding, "Critical drying of liquids," *Phys. Rev. Lett.*, vol. 117, no. 17, p. 176102, 2016.

- [43] R. Evans, M. C. Stewart, and N. B. Wilding, “Drying and wetting transitions of a lennard-jones fluid: Simulations and density functional theory,” *J. Chem. Phys.*, vol. 147, no. 4, p. 044701, 2017.
- [44] D. Chandler, “Interfaces and the driving force of hydrophobic assembly,” *Nature*, vol. 437, no. 7059, pp. 640–647, 2005.
- [45] B. J. Berne, J. D. Weeks, and R. Zhou, “Dewetting and hydrophobic interaction in physical and biological systems,” *Annu. Rev. Phys. Chem.*, vol. 60, p. 85, 2009.
- [46] E. Ueda and P. A. Levkin, “Emerging applications of superhydrophilic-superhydrophobic micropatterns,” *Adv. Mater.*, vol. 25, no. 9, pp. 1234–1247, 2013.
- [47] T. Aytug, A. R. Lupini, G. E. Jellison, P. C. Joshi, I. H. Ivanov, T. Liu, P. Wang, R. Menon, R. M. Trejo, E. Lara-Curzio, *et al.*, “Monolithic graded-refractive-index glass-based antireflective coatings: broadband/omnidirectional light harvesting and self-cleaning characteristics,” *J. Mater. Chem. C*, vol. 3, no. 21, pp. 5440–5449, 2015.
- [48] P. Ball, “Water as an active constituent in cell biology,” *Chem. Rev.*, vol. 108, no. 1, pp. 74–108, 2008.
- [49] M. Kanduč, A. Schlaich, E. Schneck, and R. R. Netz, “Water-mediated interactions between hydrophilic and hydrophobic surfaces,” *Langmuir*, vol. 32, no. 35, pp. 8767–8782, 2016.
- [50] X. Huang, C. J. Margulis, and B. J. Berne, “Dewetting-induced collapse of hydrophobic particles,” *PNAS*, vol. 100, no. 21, pp. 11953–11958, 2003.
- [51] B. S. Jabes, D. Bratko, and A. Luzar, “Universal repulsive contribution to the solvent-induced interaction between sizable, curved hydrophobes,” *J. Phys. Chem. Lett.*, vol. 7, no. 16, pp. 3158–3163, 2016.
- [52] S. N. Jamadagni, R. Godawat, and S. Garde, “Hydrophobicity of proteins and interfaces: Insights from density fluctuations,” *Annu. Rev. Chem. Biomol. Eng.*, vol. 2, pp. 147–171, 2011.
- [53] R. Evans and M. C. Stewart, “The local compressibility of liquids near non-adsorbing substrates: a useful measure of solvophobicity and hydrophobicity?,” *J. Phys.: Condens. Matter*, vol. 27, no. 19, p. 194111, 2015.
- [54] M. C. Stewart and R. Evans, “Phase behavior and structure of a fluid confined between competing (solvophobic and solvophilic) walls,” *Phys. Rev. E*, vol. 86, no. 3, p. 031601, 2012.
- [55] H. Acharya, S. Vembanur, S. N. Jamadagni, and S. Garde, “Mapping hydrophobicity at the nanoscale: Applications to heterogeneous surfaces and proteins,” *Faraday Disc.*, vol. 146, pp. 353–365, 2010.

- [56] A. P. Willard and D. Chandler, “The molecular structure of the interface between water and a hydrophobic substrate is liquid-vapor like,” *J. Chem. Phys.*, vol. 141, no. 18, p. 18C519, 2014.
- [57] P. Tarazona, U. M. B. Marconi, and R. Evans, “Phase equilibria of fluid interfaces and confined fluids: non-local versus local density functionals,” *Mol. Phys.*, vol. 60, no. 3, pp. 573–595, 1987.
- [58] R. Evans, “Fluids adsorbed in narrow pores: phase equilibria and structure,” *J. Phys.: Condens. Matter*, vol. 2, no. 46, p. 8989, 1990.
- [59] L. D. Gelb, K. E. Gubbins, R. Radhakrishnan, and M. Sliwinska-Bartkowiak, “Phase separation in confined systems,” *Rep. Prog. Phys.*, vol. 62, no. 12, p. 1573, 1999.
- [60] R. C. Remsing, E. Xi, S. Vembanur, S. Sharma, P. G. Debenedetti, S. Garde, and A. J. Patel, “Pathways to dewetting in hydrophobic confinement,” *Proc. Natl. Acad. Sci. USA*, vol. 112, no. 27, pp. 8181–8186, 2015.
- [61] G. Reiter, “Dewetting of thin polymer films,” *Phys. Rev. Lett.*, vol. 68, no. 1, p. 75, 1992.
- [62] R. Seemann, S. Herminghaus, and K. Jacobs, “Dewetting patterns and molecular forces: A reconciliation,” *Phys. Rev. Lett.*, vol. 86, no. 24, p. 5534, 2001.
- [63] U. Thiele, “Open questions and promising new fields in dewetting,” *Euro. Phys. J. E*, vol. 12, no. 3, pp. 409–416, 2003.
- [64] U. Thiele, “Thin film evolution equations from (evaporating) dewetting liquid layers to epitaxial growth,” *J. Phys.: Condens. Matter*, vol. 22, no. 8, p. 084019, 2010.
- [65] A. J. Archer, M. J. Robbins, and U. Thiele, “Dynamical density functional theory for the dewetting of evaporating thin films of nanoparticle suspensions exhibiting pattern formation,” *Phys. Rev. E*, vol. 81, no. 2, p. 021602, 2010.
- [66] A. Luzar, “Wetting dynamics of hydrophobic and structured surfaces: General discussion,” *Faraday Discuss.*, vol. 146, p. 290, 2010.
- [67] R. Evans, “Wetting dynamics of hydrophobic and structured surfaces: General discussion,” *Faraday Discuss.*, vol. 146, p. 297, 2010.
- [68] P. Bryk, R. Roth, M. Schoen, and S. Dietrich, “Depletion potentials near geometrically structured substrates,” *Europhys. Lett.*, vol. 63, no. 2, p. 233, 2003.
- [69] P. Hopkins, A. J. Archer, and R. Evans, “Solvent mediated interactions between model colloids and interfaces: A microscopic approach,” *J. Chem. Phys.*, vol. 131, no. 12, p. 124704, 2009.
- [70] A. J. Archer and R. Evans, “Solvent-mediated interactions and solvation close to fluid–fluid phase separation: A density functional treatment,” *J. Chem. Phys.*, vol. 118, no. 21, pp. 9726–9746, 2003.

- [71] A. J. Archer, R. Evans, R. Roth, and M. Oettel, “Solvent mediated interactions close to fluid-fluid phase separation: Microscopic treatment of bridging in a soft-core fluid,” *J. Chem. Phys.*, vol. 122, no. 8, p. 084513, 2005.
- [72] A. Malijevský and A. O. Parry, “Bridging transitions for spheres and cylinders,” *Phys. Rev. E*, vol. 92, no. 2, p. 022407, 2015.
- [73] K. Lum, D. Chandler, and J. D. Weeks, “Hydrophobicity at small and large length scales,” *J. Phys. Chem. B*, vol. 103, no. 22, pp. 4570–4577, 1999.
- [74] R. Evans, J. R. Henderson, and R. Roth, “Nonanalytic curvature contributions to solvation free energies: Influence of drying,” *J. Chem. Phys.*, vol. 121, no. 23, pp. 12074–12084, 2004.
- [75] C. A. Cerdeiriña, P. G. Debenedetti, P. J. Rossky, and N. Giovambattista, “Evaporation length scales of confined water and some common organic liquids,” *J. Phys. Chem. Lett.*, vol. 2, no. 9, pp. 1000–1003, 2011.
- [76] J. R. Henderson, “Statistical mechanical sum rules,” in *Fundamentals of Inhomogeneous Fluids* (D. Henderson, ed.), ch. 2, pp. 23–84, New York: Marcel Dekker, 1992.
- [77] K. Lum and A. Luzar, “Pathway to surface-induced phase transition of a confined fluid,” *Phys. Rev. E*, vol. 56, no. 6, p. R6283, 1997.
- [78] P. Attard, D. R. Bérard, C. P. Ursenbach, and G. N. Patey, “Interaction free energy between planar walls in dense fluids: An ornstein-zernike approach with results for hard-sphere, lennard-jones, and dipolar systems,” *Phys. Rev. A*, vol. 44, no. 12, p. 8224, 1991.
- [79] A. Maciołek, A. Drzewiński, and P. Bryk, “Solvation force for long-ranged wall–fluid potentials,” *J. Chem. Phys.*, vol. 120, no. 4, pp. 1921–1934, 2004.
- [80] S. N. Jamadagni, R. Godawat, and S. Garde, “How surface wettability affects the binding, folding, and dynamics of hydrophobic polymers at interfaces,” *Langmuir*, vol. 25, no. 22, pp. 13092–13099, 2009.
- [81] P. Liu, X. Huang, R. Zhou, and B. J. Berne, “Observation of a dewetting transition in the collapse of the melittin tetramer,” *Nature*, vol. 437, no. 7055, pp. 159–162, 2005.
- [82] M. Mezger, H. Reichert, S. Schöder, J. Okasinski, H. Schröder, H. Dosch, D. Palms, J. Ralston, and V. Honkimäki, “High-resolution in situ x-ray study of the hydrophobic gap at the water–octadecyl-trichlorosilane interface,” *Proc. Natl. Acad. Sci. U.S.A.*, vol. 103, no. 49, pp. 18401–18404, 2006. see also M. Mezger, H. Reichert, B. M. Ocko, H. Daillant and H. Dosch, *Phys. Rev. Lett.*, **107**, 249801 (2011) and S. Chattopadhyay, A. Uysal, B. Stripe, Y.-G. Ha, J. Tobin, E. A. Karapetrova and P. Dutta, *Phys. Rev. Lett.* **107**, 249802 (2011).
- [83] J. Janecek and R. R. Netz, “Interfacial water at hydrophobic and hydrophilic surfaces: Depletion versus adsorption,” *Langmuir*, vol. 23, no. 16, pp. 8417–8429, 2007.

- [84] M. C. Stewart and R. Evans, "Layering transitions and solvation forces in an asymmetrically confined fluid," *J. Chem. Phys.*, vol. 140, no. 13, p. 134704, 2014.
- [85] B. Chacko, R. Evans, and A. J. Archer, "Solvent fluctuations around solvophobic, solvophilic, and patchy nanostructures and the accompanying solvent mediated interactions," *J. Chem. Phys.*, vol. 146, no. 12, p. 124703, 2017.
- [86] J. A. Barker and D. Henderson, "What is "liquid"? understanding the states of matter," *Rev. Mod. Phys.*, vol. 48, no. 4, p. 587, 1976.
- [87] J. K. Percus, "Approximation methods in classical statistical mechanics," *Phys. Rev. Lett.*, vol. 8, no. 11, p. 462, 1962.
- [88] J. D. Weeks, K. Vollmayr, and K. Katsov, "Intermolecular forces and the structure of uniform and nonuniform fluids," *Physica A*, vol. 244, no. 1-4, pp. 461–475, 1997.
- [89] J. D. Weeks, K. Katsov, and K. Vollmayr, "Roles of repulsive and attractive forces in determining the structure of nonuniform liquids: Generalized mean field theory," *Phys. Rev. Lett.*, vol. 81, no. 20, p. 4400, 1998.
- [90] J. D. Weeks, "Connecting local structure to interface formation: A molecular scale van der waals theory of nonuniform liquids," *Ann. Rev. Phys. Chem.*, vol. 53, no. 1, pp. 533–562, 2002.
- [91] J. L. Lebowitz and J. K. Percus, "Mean spherical model for lattice gases with extended hard cores and continuum fluids," *Phys. Rev.*, vol. 144, no. 1, p. 251, 1966.
- [92] H. C. Andersen, D. Chandler, and J. D. Weeks, "Roles of repulsive and attractive forces in liquids: The optimized random phase approximation," *J. Chem. Phys.*, vol. 56, no. 8, pp. 3812–3823, 1972.
- [93] J. K. Percus, "One-dimensional classical fluid with nearest-neighbor interaction in arbitrary external field," *J. Stat. Phys.*, vol. 28, no. 1, pp. 67–81, 1982.
- [94] H. Takahashi, "A simple method for treating the statistical mechanics of one-dimensional substances," in *Proc. Phys.-Math. Soc. Jpn*, vol. 24, pp. 60–62, 1942.
- [95] J. M. Brader and R. Evans, "An exactly solvable model for a colloid–polymer mixture in one-dimension," *Physica A*, vol. 306, pp. 287–300, 2002.
- [96] A. J. Archer and R. Evans, "Relationship between local molecular field theory and density functional theory for non-uniform liquids," *J. Chem. Phys.*, vol. 138, no. 1, p. 014502, 2013.
- [97] M. Dijkstra, J. M. Brader, and R. Evans, "Phase behaviour and structure of model colloid-polymer mixtures," *J. Phys.: Condens. Matter*, vol. 11, no. 50, p. 10079, 1999.
- [98] J. K. Percus, "Equilibrium state of a classical fluid of hard rods in an external field," *J. Stat. Phys.*, vol. 15, no. 6, pp. 505–511, 1976.

- [99] J. M. Rodgers and J. D. Weeks, “Local molecular field theory for the treatment of electrostatics,” *J. Phys.: Condens. Matter*, vol. 20, no. 49, p. 494206, 2008.
- [100] R. C. Remsing, S. Liu, and J. D. Weeks, “Long-ranged contributions to solvation free energies from theory and short-ranged models,” *Proc. Natl Acad. Sci. USA*, vol. 113, p. 2819, 2016.
- [101] T. V. Ramakrishnan and M. Yussouff, “First-principles order-parameter theory of freezing,” *Phys. Rev. B*, vol. 19, no. 5, p. 2775, 1979.
- [102] R. Evans, P. Tarazona, and U. M. B. Marconi, “On the failure of certain integral equation theories to account for complete wetting at solid-fluid interfaces,” *Mol. Phys.*, vol. 50, no. 5, pp. 993–1011, 1983.
- [103] R. Evans and U. M. B. Marconi, “Comment on “simple theory for the critical adsorption of a fluid”,” *Phys. Rev. A*, vol. 34, no. 4, p. 3504, 1986.
- [104] A. I. Campbell, V. J. Anderson, J. S. van Duijneveldt, and P. Bartlett, “Dynamical arrest in attractive colloids: the effect of long-range repulsion,” *Phys. Rev. Lett.*, vol. 94, no. 20, p. 208301, 2005.
- [105] A. Stradner, H. Sedgwick, F. Cardinaux, W. C. Poon, S. U. Egelhaaf, and P. Schurtenberger, “Equilibrium cluster formation in concentrated protein solutions and colloids,” *Nature*, vol. 432, no. 7016, pp. 492–495, 2004.
- [106] D. Pini, G. Jialin, A. Parola, and L. Reatto, “Enhanced density fluctuations in fluid systems with competing interactions,” *Chem. Phys. Lett.*, vol. 327, no. 3, pp. 209–215, 2000.
- [107] D. Pini, A. Parola, and L. Reatto, “Freezing and correlations in fluids with competing interactions,” *J. Phys.: Condens. Matter*, vol. 18, no. 36, p. S2305, 2006.
- [108] A. J. Archer, D. Pini, R. Evans, and L. Reatto, “Model colloidal fluid with competing interactions: Bulk and interfacial properties,” *J. Chem. Phys.*, vol. 126, no. 1, p. 014104, 2007.
- [109] A. J. Archer and N. B. Wilding, “Phase behavior of a fluid with competing attractive and repulsive interactions,” *Phys. Rev. E*, vol. 76, no. 3, p. 031501, 2007.
- [110] M. B. Sweatman, R. Fartaria, and L. Lue, “Cluster formation in fluids with competing short-range and long-range interactions,” *J. Chem. Phys.*, vol. 140, no. 12, p. 124508, 2014.
- [111] J.-M. Bomont, J.-L. Bretonnet, D. Costa, and J.-P. Hansen, “Communication: Thermodynamic signatures of cluster formation in fluids with competing interactions,” *J. Chem. Phys.*, vol. 137, no. 1, p. 011101, 2012.
- [112] J. Pełkalski, A. Ciach, and N. G. Almarza, “Periodic ordering of clusters in a one-dimensional lattice model,” *J. Chem. Phys.*, vol. 138, no. 14, p. 144903, 2013.

- [113] J. Pełkalski, A. Ciach, and N. G. Almarza, “Periodic ordering of clusters and stripes in a two-dimensional lattice model. i. ground state, mean-field phase diagram and structure of the disordered phases,” *J. Chem. Phys.*, vol. 140, no. 11, p. 114701, 2014.
- [114] N. G. Almarza, J. Pełkalski, and A. Ciach, “Periodic ordering of clusters and stripes in a two-dimensional lattice model. ii. results of monte carlo simulation,” *J. Chem. Phys.*, vol. 140, no. 16, p. 164708, 2014.
- [115] W. Selke and M. E. Fisher, “Two-dimensional ising models with competing interactions: a monte carlo study,” *Zeitschrift für Physik B Condensed Matter*, vol. 40, no. 1, pp. 71–77, 1980.
- [116] D. P. Landau and K. Binder, “Phase diagrams and critical behavior of ising square lattices with nearest-, next-nearest-, and third-nearest-neighbor couplings,” *Phy. Rev. B*, vol. 31, no. 9, p. 5946, 1985.
- [117] D. Andelman, F. Broçhard, and J.-F. Joanny, “Phase transitions in langmuir monolayers of polar molecules,” *J. Chem. Phys.*, vol. 86, no. 6, pp. 3673–3681, 1987.
- [118] Z. Nussinov, J. Rudnick, S. A. Kivelson, and L. N. Chayes, “Avoided critical behavior in o (n) systems,” *Phys. Rev. Lett.*, vol. 83, no. 3, p. 472, 1999.
- [119] C. B. Muratov, “Theory of domain patterns in systems with long-range interactions of coulomb type,” *Phys. Rev. E*, vol. 66, no. 6, p. 066108, 2002.
- [120] M. Tarzia and A. Coniglio, “Lamellar order, microphase structures, and glassy phase in a field theoretic model for charged colloids,” *Phys. Rev. E*, vol. 75, no. 1, p. 011410, 2007.
- [121] R. P. Sear and W. M. Gelbart, “Microphase separation versus the vapor-liquid transition in systems of spherical particles,” *J. Chem. Phys.*, vol. 110, no. 9, pp. 4582–4588, 1999.
- [122] R. P. Sear, S.-W. Chung, G. Markovich, W. M. Gelbart, and J. R. Heath, “Spontaneous patterning of quantum dots at the air-water interface,” *Phys. Rev. E*, vol. 59, no. 6, p. R6255, 1999.
- [123] A. Imperio and L. Reatto, “A bidimensional fluid system with competing interactions: spontaneous and induced pattern formation,” *J. Phys.: Condens. Matter*, vol. 16, no. 38, p. S3769, 2004.
- [124] A. Imperio and L. Reatto, “Microphase separation in two-dimensional systems with competing interactions,” *J. Chem. Phys.*, vol. 124, no. 16, p. 164712, 2006.
- [125] A. Imperio and L. Reatto, “Microphase morphology in two-dimensional fluids under lateral confinement,” *Phys. Rev. E*, vol. 76, no. 4, p. 040402, 2007.

- [126] A. J. Archer, “Two-dimensional fluid with competing interactions exhibiting microphase separation: Theory for bulk and interfacial properties,” *Phys. Rev. E*, vol. 78, no. 3, p. 031402, 2008.
- [127] D. P. Landau and K. Binder, *A guide to Monte Carlo simulations in statistical physics*. Cambridge university press, 2014.
- [128] R. Bowley and M. Sanchez, *Introductory statistical mechanics*. Clarendon Press Oxford, 1999.
- [129] J. N. Israelachvili, *Intermolecular and surface forces: revised third edition*. Academic press, 2011.
- [130] D. El Masri, T. Vissers, S. Badaire, J. C. P. Stiefelhagen, H. R. Vutukuri, P. Helfferich, T. H. Zhang, W. K. Kegel, A. Imhof, and A. van Blaaderen, “A qualitative confocal microscopy study on a range of colloidal processes by simulating microgravity conditions through slow rotations,” *Soft Matter*, vol. 8, no. 26, pp. 6979–6990, 2012.
- [131] A. Ciach, J. Pękalski, and W. T. Gózdź, “Origin of similarity of phase diagrams in amphiphilic and colloidal systems with competing interactions,” *Soft Matter*, vol. 9, no. 27, pp. 6301–6308, 2013.
- [132] A. J. Archer and R. Evans, “Dynamical density functional theory and its application to spinodal decomposition,” *J. Chem. Phys.*, vol. 121, no. 9, pp. 4246–4254, 2004.
- [133] U. M. B. Marconi and P. Tarazona, “Dynamic density functional theory of fluids,” *J. Chem. Phys.*, vol. 110, no. 16, pp. 8032–8044, 1999.
- [134] S. C. Greer, “Physical chemistry of equilibrium polymerization,” *J. Phys. Chem. B*, vol. 102, no. 28, pp. 5413–5422, 1998.
- [135] J. Dudowicz, K. F. Freed, J. F. Douglas, *et al.*, “Lattice model of living polymerization. i. basic thermodynamic properties,” *J. Chem. Phys.*, vol. 111, no. 15, p. 7116, 1999.
- [136] K. Van Workum and J. F. Douglas, “Equilibrium polymerization in the stockmayer fluid as a model of supermolecular self-organization,” *Phys. Rev. E*, vol. 71, no. 3, p. 031502, 2005.
- [137] A. Jain, J. R. Errington, and T. M. Truskett, “Dimensionality and design of isotropic interactions that stabilize honeycomb, square, simple cubic, and diamond lattices,” *Phys. Rev. X*, vol. 4, no. 3, p. 031049, 2014.
- [138] N. G. Almarza, J. Pękalski, and A. Ciach, “Effects of confinement on pattern formation in two dimensional systems with competing interactions,” *Soft Matter*, vol. 12, no. 36, pp. 7551–7563, 2016.